

The Development of a Hollow Concrete Masonry System
for use with Near-Surface Mounted Reinforcement

by

Adrien Joseph James Sparling

A Thesis submitted to the Faculty of Graduate Studies of

The University of Manitoba

in partial fulfilment of the requirements of the degree of

MASTER OF SCIENCE

Department of Civil Engineering

University of Manitoba

Winnipeg

Copyright © 2015 by Adrien Joseph James Sparling

Abstract

The 21st century has brought with it myriad innovative construction techniques and structural systems; however reinforced masonry systems have gone virtually unchanged over the last decades. The innovative Surface-Reinforced Concrete Masonry Unit (SRCMU) system makes use of Near-Surface Mounted reinforcement to form a structurally efficient system. Preliminary analysis of this system shows the potential for improved moment resistance when compared to conventional masonry construction. There is also evidence for a potential decrease in embodied and operating energy for finished structures using the SRCMU system. Experimental work indicates similar axial compressive behaviour of the SRCMU when compared to conventional concrete masonry systems. Pull-out and flexural tests performed on reinforced SRCMU specimens indicate it is possible to achieve a good bond between the SRCMU system and the reinforcing bars; up to 60kN of pull out force was developed in 590mm of bonded length, and flexural specimens developed up to 20kNm/m of moment-resistance.

Acknowledgements

I would like to thank my advisors Dr. Hashemian and Dr. Britton for their support and guidance throughout my Master of Science program. Without you, none of this would have been possible. I would also like to thank the University of Manitoba and the W.R. McQuade Structures Laboratory staff; Chad, Brendan, and Grant were instrumental in the experimental work discussed in this report. I would like to acknowledge SIKA's donation of the dowelling epoxy which was used to strengthen the SRCMU specimens, and the Manitoba Masonry Institute, which provided the skilled labour necessary to construct the masonry specimens. Thank you to Dr. Cha and Dr. Kordi for agreeing to be part of my examining committee.

A Special thanks to my colleagues in the faculty of Civil Engineering for all your help throughout this process, and thank you to Dr. El-Salakawy for allowing me to use your software. Thank you to my parents, Richard and Carol, my siblings, Claire and Lucas, and all my friends for your support. Thank you, Grace, for your patience.

Dedication

To our great-grandchildren

Table of contents

1	Chapter 1 – Introduction.....	1
1.1	Conventional reinforced concrete masonry.....	2
1.2	The surface-reinforced concrete masonry system.....	5
1.2.1	SRCMU structural applications	9
1.2.2	Expected performance	9
1.3	Construction materials reduction and sustainability	17
1.3.1	Embodied energy (EE) vs. operating energy (OE).....	17
1.3.2	Use of recycled and waste materials.....	19
1.3.3	Decreased use of materials.....	20
1.3.4	Decrease energy input during construction.....	21
1.3.5	Operating energy.....	22
1.3.6	Near-surface mounted reinforcing bars	24
1.3.7	NSM application case studies	24
1.3.8	Experimental laboratory studies	26
1.3.9	Numerical analysis of NSM reinforced systems.....	27
1.4	Commercial block production.....	29
1.4.1	Mix design	30

1.4.2	Block casting.....	31
1.4.3	Curing	31
2	Chapter 2 – Experimental Phase 1: Block Fabrication.....	33
2.1	Manufacture of concrete block moulds.....	33
2.2	Development of a concrete mix design for casting CMUs in laboratory.....	35
2.2.1	Production of dry-mix concrete cylinders.....	35
2.2.2	Outcomes from dry-mix concrete casting.....	37
2.2.3	Workable concrete mix for concrete block production.....	38
2.3	Block production.....	38
2.3.1	Preparation of moulds.....	39
2.3.2	Determination of moisture content for sand and aggregate (based on ASTM C566)	
	40	
2.3.3	Concrete batching and mixing	41
2.3.4	Concrete casting.....	45
2.3.5	Unmolding and curing	46
3	Chapter 3 – Experimental Phase 2: Material Testing and Block Validation.....	48
3.1	Preparation of axial compression specimens	49
3.1.1	Casting of masonry prisms.....	49
3.1.2	Curing of masonry prisms.....	50
3.1.3	Instrumentation of masonry prisms	50

3.1.4	Preparation of concrete test cylinders	52
3.2	Axial testing of concrete and masonry specimens	53
3.2.1	Prism test set-up.....	53
3.2.2	CMU test set-up	55
3.2.3	Concrete cylinder testing	55
3.3	Experimental results of axial compression tests	56
3.3.1	Masonry prisms.....	56
3.3.2	Masonry Units.....	60
3.3.3	Concrete test cylinders	62
3.4	Preparation of tensile specimens	63
3.4.1	Steel reinforcing bar specimens	63
3.4.2	GFRP reinforcing bar specimens	66
3.5	Tension test procedure	67
3.6	Experimental results of reinforcing bar testing	69
3.7	Discussion	71
3.7.1	Masonry prisms.....	72
3.7.2	Concrete blocks and test cylinders.....	72
3.7.3	Reinforcing bars.....	73
4	Experimental Phase 3: Testing of Reinforced SRCMU Assemblies.....	74
4.1	Pull-out testing	74

4.1.1	Specimen fabrication	75
4.1.2	Test procedure.....	77
4.1.3	Results.....	80
4.1.4	Discussion.....	89
4.2	Flexural testing.....	92
4.2.1	Specimen fabrication	92
4.2.2	Test set-up.....	97
4.2.3	Results.....	101
4.2.4	Discussion.....	105
4.2.5	Shear behaviour	113
5	ATENA FEA Analysis	114
5.1	Model geometry	114
5.2	Material properties	117
5.3	Support and loading conditions.....	120
5.4	Pull-out analysis	122
5.4.1	Steel reinforcement	123
5.4.2	GFRP reinforcement	126
5.5	Flexural analysis.....	129
5.5.1	Perfect bond – Steel reinforcement.....	130
5.5.2	Perfect bond – GFRP reinforcement.....	132

6	Conclusion and Future Work.....	136
6.1	Benefits of the SRMCU system	136
6.2	Axial behaviour	137
6.3	Flexural behaviour.....	138
6.4	Proposed future work	139
6.4.1	Test confirmation	139
6.4.2	Tall flexural walls	139
6.4.3	SRCMU walls in Shear.....	140
6.4.4	Fire resistance	140
6.4.5	Earthquake resistance.....	140
6.4.6	Monitoring of a complete structure.....	140
	References.....	141

List of Tables

Table 1: Theoretical test wall properties..... 9

Table 2: Theoretical test wall configurations..... 10

Table 3: Constants for S304.1 analysis..... 11

Table 4: Embodied energy of conventional grouting vs. SRCMU epoxy grouting 21

Table 5: Insulation characteristics of concrete and polyurethane foam..... 22

Table 6: Concrete mix proportions 38

Table 7: Concrete batching variables..... 42

Table 8: 2014-06-26 concrete mix variables 43

Table 9: 2014-06-26 concrete mix component mass 43

Table 10: Prism age at testing..... 50

Table 11: CMU type acronym 57

Table 12: Compressive masonry prisms, elastic modulus E 58

Table 13: Compressive masonry prisms, ultimate strength 59

Table 14: Axial compression prisms modes of failure 60

Table 15: Axial testing of LCCMU concrete blocks 61

Table 16: Axial testing of concrete cylinder samples..... 62

Table 17: Steel rebar material properties 70

Table 18: GFRP reinforcing bar material properties 71

Table 19: Pull-out specimen age at time of testing..... 77

Table 20: Pull-out specimens maximum load and mode of failure 81

Table 21: Flexural specimen age at time of testing 96

Table 22: Flexural specimens maximum load 102

Table 23: Notation used for moment of inertia calculations.....	106
Table 24: Material properties for stiffness calculations.....	107
Table 25: Reinforced masonry moment of inertia	110
Table 26: ATENA FEA material properties	117
Table 27: Reinforcement bond models	120

List of Figures

Figure 1: Grade beam segment with protruding reinforcing bars..... 3

Figure 2: Conventional masonry construction in running bond 3

Figure 3: Location of joint reinforcement, conventional masonry system 4

Figure 4: Lintel blocks and lintel construction 5

Figure 5: Conventional CMU dimensions 6

Figure 6: SRCMU dimensions..... 7

Figure 7: Fully reinforced SRCMU assembly 8

Figure 8: Conventional (left) and SRCMU (right) masonry assemblies; fully reinforced systems shown 8

Figure 9: Interaction diagram; ungrouted walls..... 14

Figure 10: Interaction diagram; fully grouted walls 15

Figure 11: Interaction diagram; partially grouted walls 15

Figure 12: Generic bilinear shear-slip bond model..... 29

Figure 13: SRCMU mould; exploded view 34

Figure 14: Curing water bath temperature 37

Figure 15: Low cohesion of poorly consolidated commercial concrete mix 37

Figure 16: SRCMU mould; threaded rod alignment 40

Figure 17: Vertical axis electric concrete mixer 44

Figure 18: Filled concrete block moulds covered by a polymer sheet 45

Figure 19: SRCMU sample date stamp 46

Figure 20: Laboratory-cast vs. commercial CMU surface texture 49

Figure 21: Location of pi-gauges; conventional shaped blocks, front and back	51
Figure 22: Conventional CMU prism fitted with pi-gauges	51
Figure 23: Location of pi-gauges and gauge points; SRCMUs, front (left) and back (right).....	52
Figure 24: Cylinder capping jig	53
Figure 25: Masonry prism centered in loading frame.....	54
Figure 26: Concrete cylinder testing machine	56
Figure 27: Compressive masonry prisms, elastic modulus E	57
Figure 28: Compressive masonry prisms, ultimate strength.....	58
Figure 29: CMU mode of failure	62
Figure 30: Steel rebar - prepared surface for strain gauge installation	64
Figure 31: Prepared electronic strain gauge.....	64
Figure 32: Strain gauge - installation complete	66
Figure 33: Instron universal testing machine.....	68
Figure 34: Stress-strain plot, steel reinforcing bar specimens	70
Figure 35: Stress-strain plot, GFRP reinforcing bar specimens	71
Figure 36: Strain gauge location: pull-out specimen steel (top) and GFRP (bottom) reinforcing bars	75
Figure 37: Pull-out bar installation	76
Figure 38: pull-out restraining jig.....	79
Figure 39: Pull-out specimen modes of deterioration.....	81
Figure 40: Bar stress distribution, specimen P3 (Steel reinforced)	82
Figure 41: Bar stress distribution, specimen P4 (GFP-reinforced).....	82
Figure 42: Bar stress distribution, specimen P2 (steel-reinforced).....	83

Figure 43: Bar stress distribution, specimen P5 (GFRP-reinforced)	83
Figure 44: Bond shear stress distribution, specimen P3 (steel-reinforced)	84
Figure 45: Bond shear stress distribution, specimen P4 (GFRP-reinforced).....	85
Figure 46: Bond shear stress distribution, specimen P2 (steel-reinforced)	85
Figure 47: Bond shear stress distribution, specimen P5 (GFRP-reinforced).....	86
Figure 48: Bond shear stress vs. slip, specimen P3 (steel-reinforced).....	87
Figure 49: Bond shear stress vs. slip, specimen P4 (GFRP-reinforced).....	87
Figure 50: Bond shear stress vs. slip, specimen P2 (steel-reinforced).....	88
Figure 51: Bond shear stress vs. slip, specimen P5 (GFRP-reinforced).....	88
Figure 52: Bond shear stress vs slip, specimens P1-P5 (24.5mm from top of specimen)	89
Figure 53: Pull-out specimen: base lifting during testing	90
Figure 54: Stress concentration due to eccentric loading	90
Figure 55: Flexural specimen reinforcement strain gauge location.....	93
Figure 56: Flexural specimen strain gauge locations.....	94
Figure 57: Flexural specimen, pi-gauge and LVDT mount locations	96
Figure 58: Flexural four-point loading conditions.....	97
Figure 59: Flexural test set-up: welded support.....	98
Figure 60: Flexural test set-up	99
Figure 61: Flexural test set-up: close up	99
Figure 62: Flexural specimen hoisting jig	100
Figure 63: Flexural specimen held in place using bar clamps	101
Figure 64: Load vs. deflection, steel-reinforced flexural specimens	102
Figure 65: Load vs. deflection, GFRP-reinforced specimens.....	103

Figure 66: Load vs. crack opening width, steel-reinforced flexural specimens	103
Figure 67: Load vs crack opening width, steel reinforced flexural specimens.....	104
Figure 68: Load vs. strain, steel-reinforced specimen F1	104
Figure 69: Load vs. strain, GFRP-reinforced specimen F4	105
Figure 70: Steel-reinforced flexural displacement with code-predicted behaviour.....	111
Figure 71: GFRP-reinforced flexural displacement with code predicted behaviour	111
Figure 72: Conventional vs. SRCMU flexural stiffness - steel-reinforced.....	112
Figure 73: Conventional vs. SRCMU flexural stiffness - GFRP-reinforced.....	113
Figure 74: x-y coordinates for SRCMU cross-section numerical model.....	115
Figure 75: Pull-out FEA model.....	115
Figure 76: Flexural FEA model	116
Figure 77: Pull-out FEA model, support/loading conditions.....	121
Figure 78: Flexural FEA model, support conditions	122
Figure 79: Flexural FEA model, loading conditions	122
Figure 80: Steel-reinforced pull-out load vs. total slip (at surface), experimental and FEA data	123
Figure 81: Pull-out load vs strain at 45mm from the loaded end, steel-reinforced specimens...	124
Figure 82: Pull-out load vs strain at 145mm from the loaded end, steel-reinforced specimens.	125
Figure 83: Pull-out load vs strain at 245mm from the loaded end, steel-reinforced specimens.	125
Figure 84: Pull-out load vs strain at 345mm from the loaded end, steel-reinforced specimens.	126
Figure 85: GFRP-reinforced Pull-out load vs. total slip (at surface), experimental and FEA data	127
Figure 86: Pull-out load vs strain at 45mm from the loaded end, GFRP-reinforced specimens	128

Figure 87: Pull-out load vs strain at 245mm from the loaded end, GFRP-reinforced specimens	129
Figure 88: Load-deflection curve, comparison with ATENA FEA - steel-reinforced	130
Figure 89: Crack-width expansion, comparison with ATENA FEA - steel-reinforced	131
Figure 90: Reinforcing bar strain, comparison with ATENA FEA - steel-reinforced.....	132
Figure 91: Load-deflection curve, comparison with ATENA FEA - GFRP-reinforced.....	133
Figure 92: Crack-width expansion, comparison with ATENA FEA - GFRP-reinforced.....	134
Figure 93: Reinforcing bar strain, comparison with ATENA FEA - GFRP-reinforced.....	134

Glossary of Acronyms

CCMU	Commercially produced Concrete Masonry Unit
CFRP	Carbon Fibre Reinforced Polymer
CMU	Hollow Concrete Masonry Unit
CNC	Computer Numeric Controlled (cutting machine)
DAQ	Data Acquisition (system)
DOM	Drawn On Mandrel (steel tube)
EC	Embodied CO ₂
EE	Embodied Energy
FEA	Finite Element Analysis
FRP	Fibre Reinforced Polymer
GFRP	Glass Fibre Reinforced Polymer
GHG	Greenhouse Gas (emissions)
HSS	Hollow Structural Section
ICE	Inventory of Carbon and Energy (Bath University)
LCCMU	Laboratory-Cast Concrete Masonry Unit
LVDT	Linear Variable Differential Transducer
NSM	Near-Surface Mounted (reinforcement)
OC	Operating CO ₂
OE	Operating Energy
RC	Reinforced Concrete
SCM	Supplementary Cementing Material
SLS	Serviceability Limit State (design)
SRCMU	Surface-Reinforced Concrete Masonry Unit

Standard Notation

A	Effective cross-sectional area of a reinforcing bar
A_e	Effective cross-sectional area of masonry (mm^2/m)
A_{ep}	Cross-sectional area of epoxy grout within a masonry section
A_{rs}	Cross-sectional area of steel reinforcing bars within a masonry section
A_{rg}	Cross-sectional area of GFRP reinforcing bars within a masonry section
A_s	Effective cross-sectional area of reinforcing steel nearest the extreme tension face (mm^2/m)
a_w	Portion of the thickness of the webs and grouted cores engaged in compression (mm)
a_1	Portion of the thickness of the face shell nearest the extreme tension fibre engaged in compression (mm)
a_2	Portion of the thickness of the face shell nearest the extreme compression fibre engaged in compression (mm^2/mm)
b	Width of the masonry section under consideration
C	Sum of axial compressive forces carried by the masonry
c	Distance from the extreme compression fibre to the neutral
C_b	Circumference of a reinforcing bar's cross-section
C_w	Portion of the axial compressive force carried by area ba_w
C_1	Portion of the axial compressive force carried by area ba_1
C_2	Portion of the axial compressive force carried by area ba_2
d	Distance from the extreme compression fibre to the centroid of reinforcing bars in tension
d'	Distance from the extreme compression fibre to the centroid of reinforcing bars in compression

d_e	Distance from the extreme compression fibre to the centroid of dowelling epoxy in tension
d_e'	Distance from the extreme compression fibre to the centroid of dowelling epoxy in compression
E	Young's modulus
E_s	Young's modulus of reinforcing steel
f_y	Yield stress for reinforcing steel
f_m'	Effective masonry compressive strength (MPa)
f_{m-g}'	Specified compressive strength of grouted masonry assembly (MPa)
f_{m-h}'	Specified compressive strength of hollow masonry assembly (MPa)
I_{cr}	Moment of inertia of a cracked masonry section
I_{cr1}	Moment of inertia of a cracked masonry section
I_{cr2}	Moment of inertia of cracked masonry where epoxy in tension does not contribute to stiffness
I_h	Moment of inertia of the hollow cores of a CMU
I_{mcr}	Moment of inertia of the uncracked portion of masonry within a cracked masonry section
I_o	Uncracked moment of inertia
I_p	Moment of inertia of a fully solid CMU (no hollow)
I_r	Moment of inertia of a reinforcing bar relative to the neutral axis of the CMU in which it is placed
k_c	Out-of-plane flexural stiffness of a conventional masonry wall
k_{srcmu}	Out-of-plane flexural stiffness of an SRCMU masonry wall

k_d	Depth from the extreme compression fibre of a cracked masonry section to the neural axis
L	Distance or length
M_a	Bulk mass of aggregate (kg)
M_c	Mass of cement (kg)
M_f	Mass of fly ash (kg)
M_r	Resistance to applied moments
M_s	Bulk mass of sand (kg)
M_w	Mass of water (kg)
n_e	Modular ratio of epoxy grout relative to masonry
n_{gc}	Number of grouted cores per meter length of wall
n_{rg}	Modular ratio of GFRP reinforcing bars relative to masonry
n_{rs}	Modular ratio of steel reinforcing bars relative to masonry
P_a	Proportion of aggregate (kg/m^3)
P_c	Proportion of cement (kg/m^3)
P_f	Proportion of fly ash (kg/m^3)
P_r	Resistance to compressive stress
P_{rmax}	Maximum allowed compressive resistance of a masonry wall assembly
P_s	Proportion of sand (kg/m^3)
P_w	Proportion of water (kg/m^3)
R	Material heat flow resistance coefficient ($1/U$)
S_{ec}	Moment of area of epoxy grout in compression within a cracked section
S_{et}	Moment of area of epoxy grout in tension within a cracked section

S_m	Moment of area of masonry within a cracked section
S_{rc}	Moment of area of reinforcing bars in compression within a cracked section
S_{rt}	Moment of area of reinforcing bars in tension within a cracked section
T	Tensile force in a reinforcing bar
t	Total CMU thickness (mm)
t_f	CMU faceshell thickness (mm)
t_w	Total web thickness (mm/m)
U	Material heat transfer coefficient (1/R)
V_b	Batch volume; total volume of concrete elements to be cast (m^3)
V_t	Total volume (m^3)
W_d	Combined mass of dry sand/aggregate and its container
W_o	Combined mass of moist sand/aggregate and its container
W_{tare}	Mass of container
α_b	Batch factor
β_1	Ratio of the depth from of the equivalent rectangular stress block to the distance from the extreme compression fibre to the neutral axis
Δ	Used as a prefix to other variables to denote a differential value
ϵ	Strain
ϵ_m	Maximum allowable strain in a masonry specimen
ϵ_s	Strain in reinforcing steel in nearest the extreme tension face
ϵ_y	Yield strain for reinforcing steel
μ	Moisture content
μ_a	Moisture content of aggregate (g/g)

μ_s	Moisture content of sand (g/g)
τ	Local shear stress
Φ_m	Masonry material resistance factor
Φ_s	Steel material resistance factor
χ	Factor accounting for the direction of the compressive force relative to the bed joint of the masonry section

1 Chapter 1 – Introduction

Masonry, in various forms, has been used for the construction of buildings for thousands of years. Prehistoric humans built shelters and other structures by stacking stones, or bricks made from shaped clay; these techniques evolved over time to incorporate precision-cut stone, and fired clay brick, sometimes using primitive mortars to secure each piece to the next. Some of these structures, such as the great Egyptian pyramids, have withstood the test of time, and have endured for thousands of years until today.

Masonry as a material is much stronger in compression than it is in tension; for this reason, until the 20th century, masonry structures were built as compression structures; they make use of vaults and arches to span openings, and the dead weight of the structure to overcome horizontal bending and overturning loads such as wind loads on walls. The introduction of the mass-produced hollow Concrete Masonry Unit (CMU) allowed for the introduction of reinforcing bars to masonry systems. By placing reinforcing bars into the hollow cores of CMU assemblies, they could then be bonded to the masonry using a cement grout. This system, though relatively robust, has the disadvantage of being heavy because of the use of cement grout.

A new system proposed for masonry construction incorporates vertical channels along the outer faces of the masonry units so that reinforcing bars may be secured in place without filling the hollow cores of CMUs with grout. What follows is an exploratory study into the use of this innovative hollow structural masonry system reinforced with Near-Surface Mounted (NSM) reinforcing bars, for which the principal building block is the Surface Reinforced Concrete Masonry Unit (SRCMU). First will be discussed the general traits of the proposed system, followed by a review of the literature relating to similar construction methods including

conventional hollow concrete block construction, and the use of near-surface mounted (NSM) reinforcement. The remaining chapters describe in detail the four phases of a research project exploring the behaviour of the proposed new masonry system.

1.1 Conventional reinforced concrete masonry

Nowadays, conventional concrete masonry systems are constructed by laying the hollow CMUs in successive horizontal rows, each block being separated horizontally and vertically from adjacent blocks by a 10mm mortar joint. When laid in running, bond, blocks in successive rows are horizontally offset from the blocks of the lower row by half the length of a block. When arranged in that way, the hollow cores of the concrete blocks form continuous vertical cavities that run the entire height of the masonry assembly. When walls require reinforcement, reinforcing bars are placed within these vertical cavities, which are then filled in with masonry grout (a form of flowing concrete). In Canada, the design of masonry structures must conform to CSA S304.1.

This first step in conventional masonry construction is the laying of the foundation, or base, on which the masonry wall is to be constructed. Figure 1 shows a diagram of a grade-beam from which reinforcing bars are protruding; the first layer of CMUS is placed on the grade beam by threading the protruding reinforcing bars through their hollow cores, and leveling them using masonry mortar. Subsequent rows of CMUs are placed to overlap the blocks of the bottom row by 50% (i.e. each block is resting equally on two of the blocks from the preceding row) as shown in Figure 2. Joint reinforcement, in the form of a wire ladder is introduced into the mortar bed-joint every few courses depending on the design, as shown in Figure 3. Once a wall is constructed to the desired height, reinforcing bars are lowered into the cores being reinforced, then those cores are filled with masonry grout. These vertical bars overlap with the bars

protruding from the foundation to provide continuous reinforcement and a positive connection to the foundation. Clean-out holes at the base of the wall serve as an indication that the grout has filled the hollow cores of the wall all the way to the bottom.

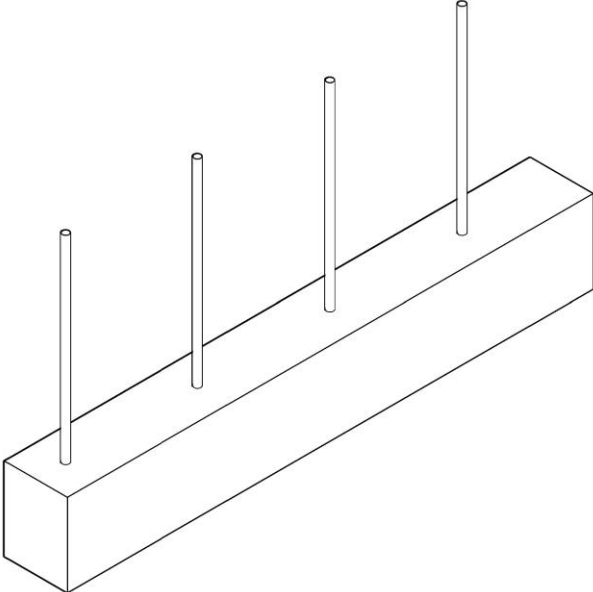


Figure 1: Grade beam segment with protruding reinforcing bars

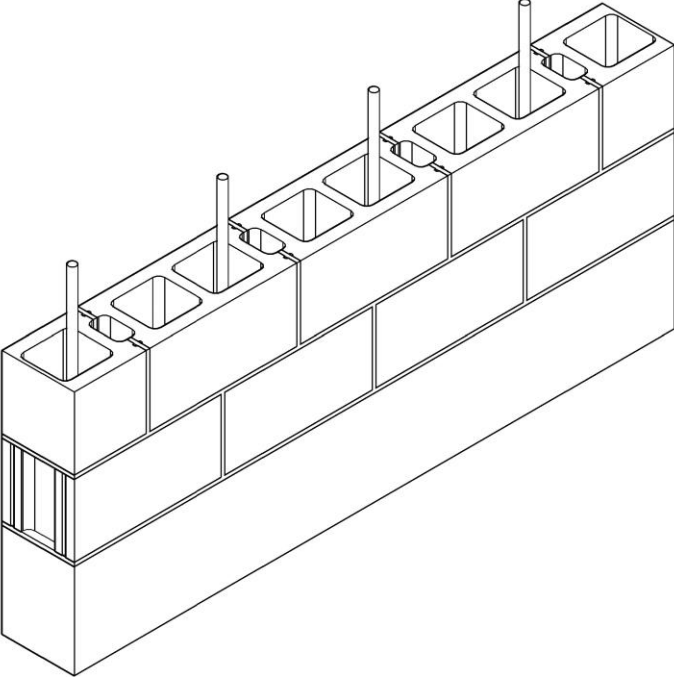


Figure 2: Conventional masonry construction in running bond

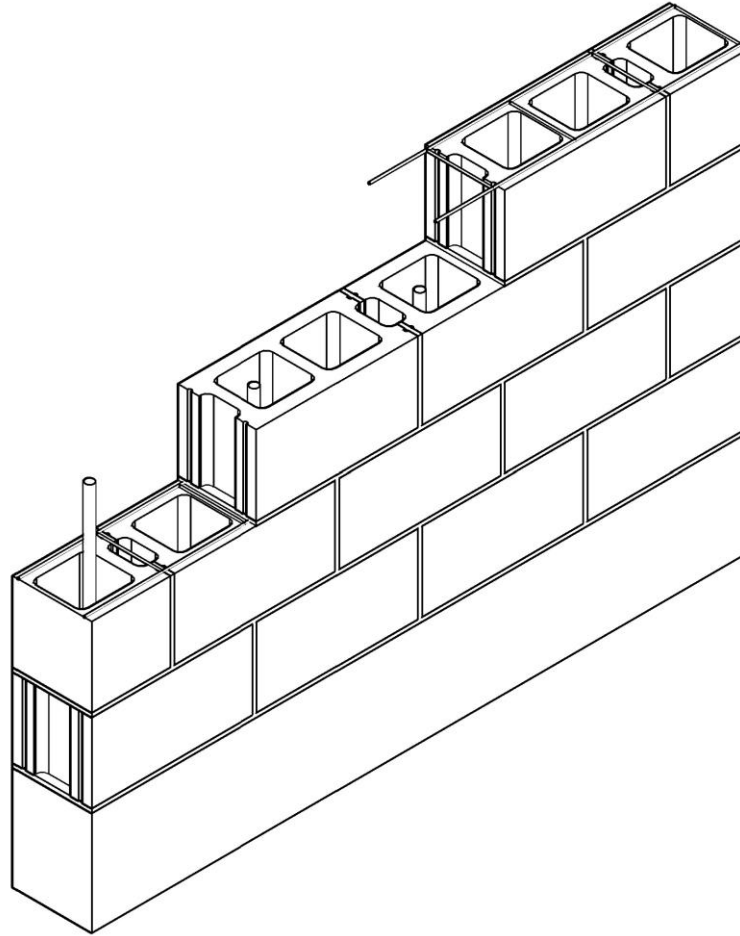


Figure 3: Location of joint reinforcement, conventional masonry system

If it is necessary to span an opening, a lintel beam is constructed. This is done by supporting a row of lintel blocks over the opening as seen in Figure 4, then placing a reinforcing bar horizontally into the bottom of the lintel blocks, while ensuring proper anchorage length is provided into the adjacent wall sections. Knockout blocks are used in the portion of the wall also accommodating horizontal reinforcement. These blocks have a breakable portion that allows a space for horizontal reinforcement as seen in Figure 4. The wall is then built to the desired height before being grout-filled to bond the reinforcing bars to the system.

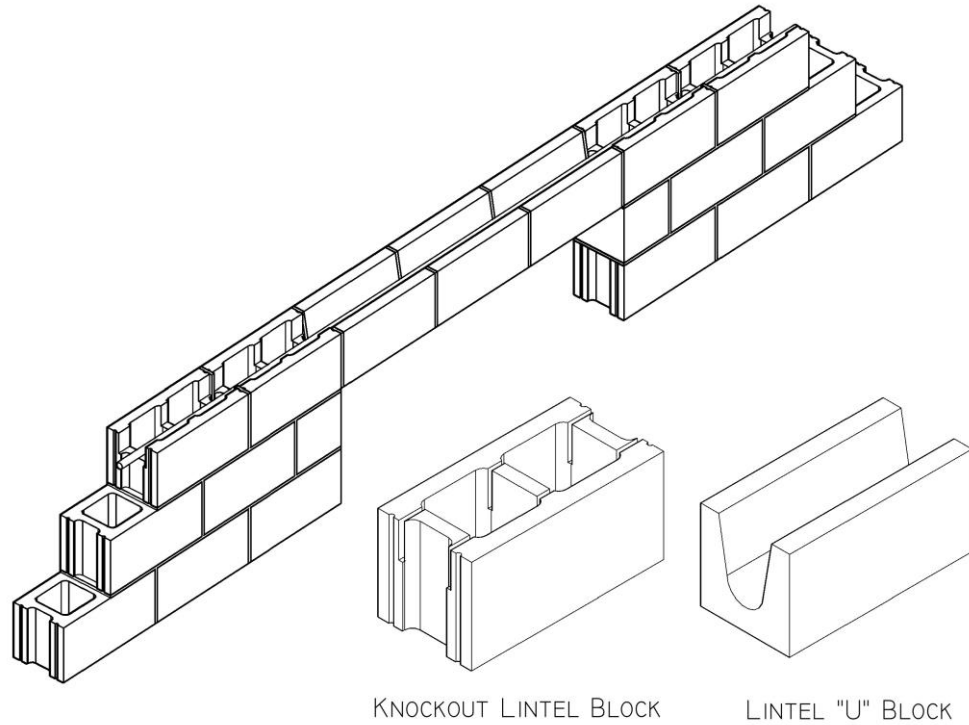


Figure 4: Lintel blocks and lintel construction

When construction takes place in winter, special provisions need to be implemented in order to allow the construction to occur. To ensure proper placement and hydration of the masonry mortar, all materials being used must be heated to above 5°C prior to use, and completed wall elements must remain warm until all mortar and grout has cured sufficiently to be allowed to freeze. In cases where it is only economical to pour grout in several walls at once, each of those walls must remain sheltered and heated until they are all constructed before grouting of a group of walls can occur. This may incur high costs in heating energy for the builder.

1.2 The surface-reinforced concrete masonry system

The SRCMU system is designed for use with NSM reinforcement. The SRCMU was developed based on the Canadian code requirements for hollow concrete masonry units (CMU) as described

in CSA A165. Figure 5 shows the required dimensions for the 200mm nominal standard hollow CMU.

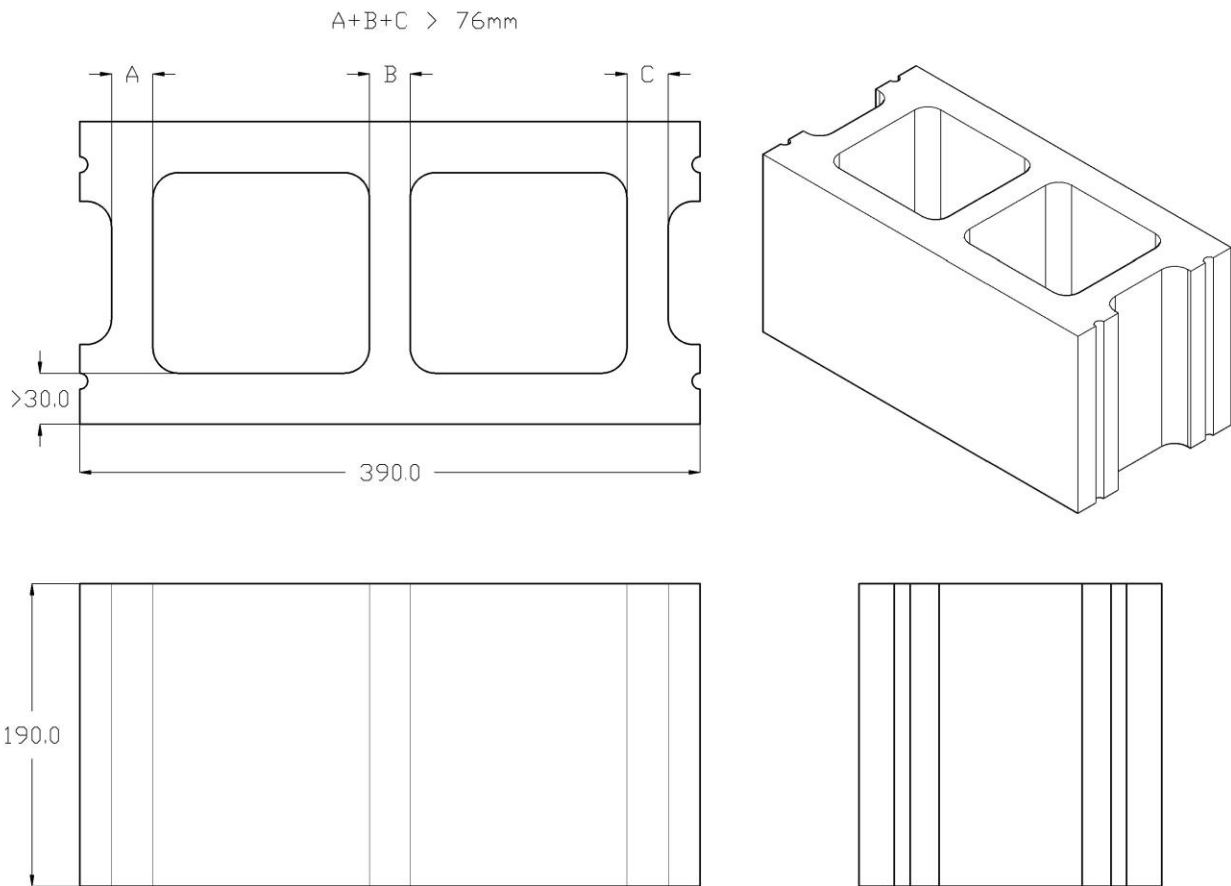


Figure 5: Conventional CMU dimensions

The SRCMU differs from conventional CMUs by the addition of a vertical channel in the middle of the face shells and a partial vertical channel on either side of each face shell as shown in Figure 6. The SRCMU was conceived to accommodate NSM reinforcement following the construction of masonry walls in running bond as shown in Figure 7. A first row of SRCMU blocks are laid horizontally, each separated by a 10mm vertical mortar joint. Successive rows of blocks are separated by a 10mm horizontal mortar joint, and staggered by 200mm relative to the row below in order to form a classical running-bond pattern. This running bond pattern allows

each central vertical face shell channel to align with two partial side channels above and below to form a continuous vertical channel running the full height of the finished masonry wall. This continuous vertical channel is therefore available to accept reinforcing bars placed therein in order to counteract the tensile stresses from out-of-plane flexural and overturning loads to which masonry walls are commonly subjected.

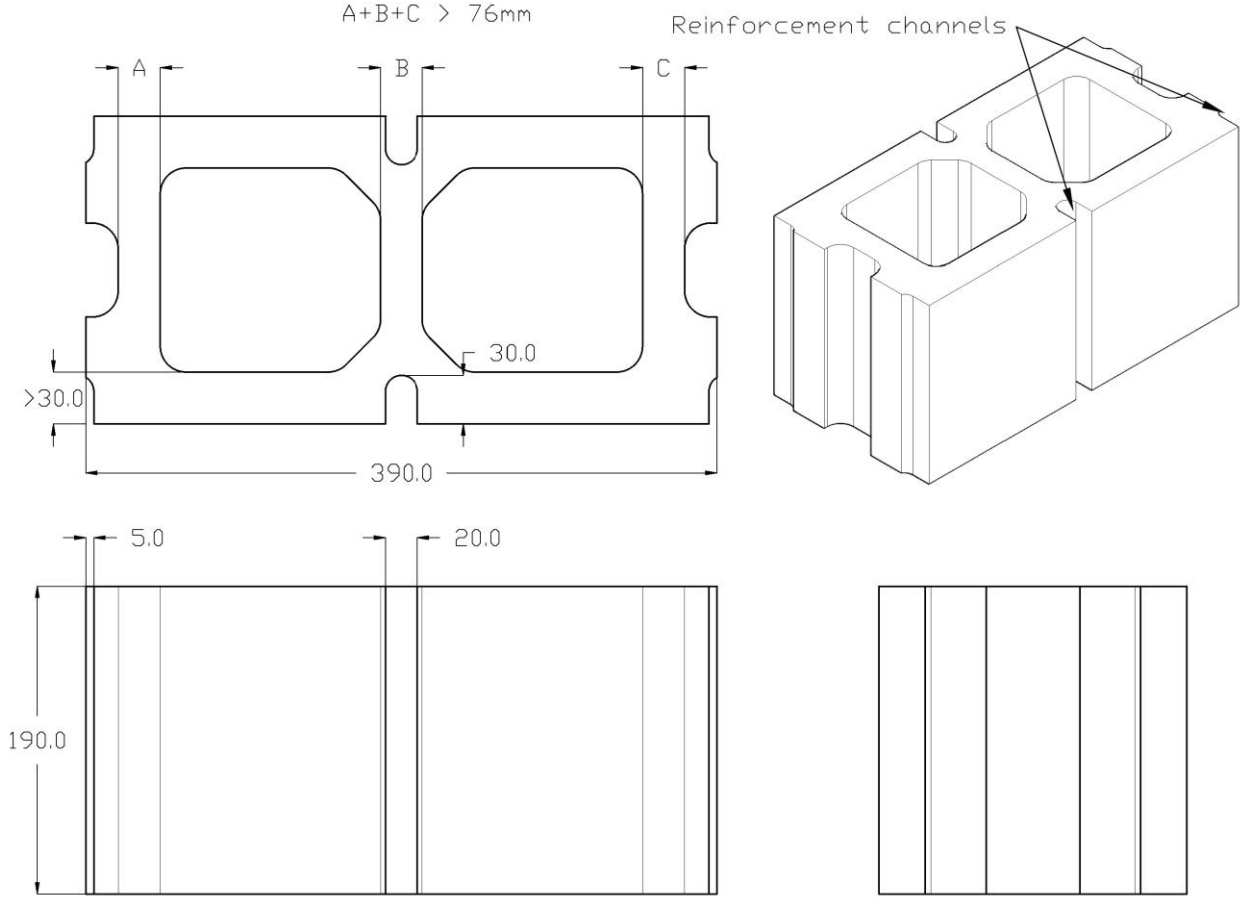


Figure 6: SRCMU dimensions

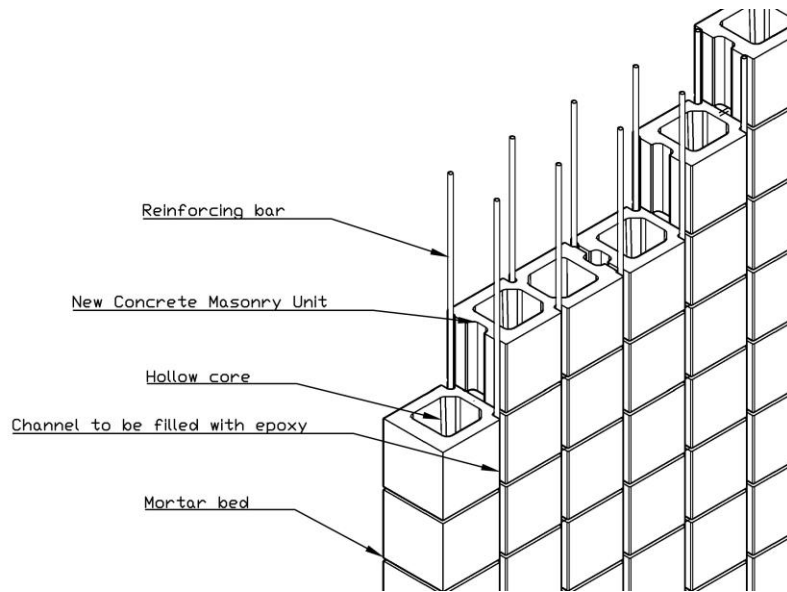


Figure 7: Fully reinforced SRCMU assembly

A visual comparison between the conventional hollow concrete masonry system and the SRCMU masonry system is shown in Figure 8. The main differences between the finished conventional and SRCMU assemblies are the location of reinforcing bars and the requirement for grout-filling of cores for reinforced conventional hollow concrete masonry assemblies.

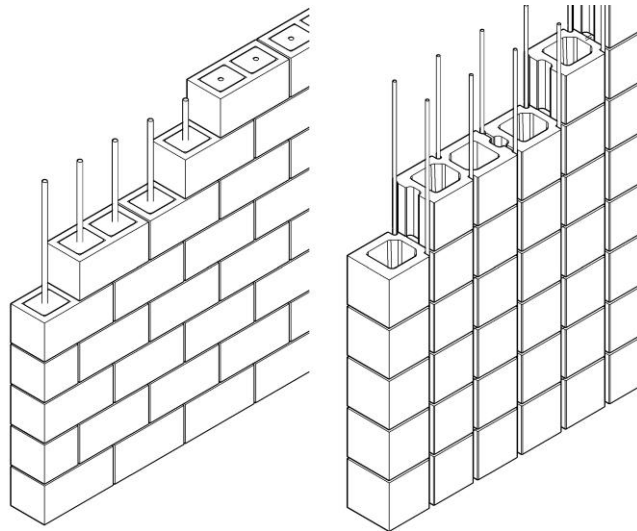


Figure 8: Conventional (left) and SRCMU (right) masonry assemblies; fully reinforced systems shown

1.2.1 SRCMU structural applications

The SRCMU was conceived for use in all applications where conventional hollow concrete masonry is currently in use. In many applications of conventional hollow concrete masonry, flexural resistance governs the design capacity. In these cases, only light axial loads are anticipated, meaning that the 50% hollow cross section of conventional masonry blocks are often sufficient to sustain the axial loads without increasing the effective cross-sectional area with masonry grout. In such cases, it is greatly advantageous for a masonry system to remain hollow while being reinforced against flexure, a case which cannot be achieved with conventional masonry systems.

1.2.2 Expected performance

A preliminary investigation into the potential benefits of the SRCMU system was performed by studying the behaviour of similarly reinforced SRCMU and conventional masonry walls as predicted by the CSA S304.1 masonry design code. For the purposes of this comparison, the most commonly used hollow CMU block type (15MPa nominal strength, 200mmX400mm nominal size) and type S (structural) mortar was used. Six wall configurations are discussed here, having the cross-sectional properties listed in Table 1; a schematic drawing of a representative meter-length for each of the configurations is shown in Table 2.

Table 1: Theoretical test wall properties

Identifier	Area of steel in tension (A_s) [mm ²]	Area of steel in compression [mm ²]	Number of grouted cores per metre length of wall (n_{gc})	Depth to steel in tension (d) [mm]	Depth to steel in compression [mm]
C/0/0	0	0	0	-	-
SR/1000/0	500	500	0	170	20
C/500/5	500	0	5	95	-
SR/500/5	250	250	5	170	20
C/250/2.5	250	0	2.5	95	-
SR/250/2.5	125	125	2.5	170	20

Table 2: Theoretical test wall configurations

Identifier	Schematic configuration
C/0/0	
SR/1000/0	
C/500/5	
SR/500/5	
C/250/2.5	
SR/250/2.5	

The interaction diagram (showing the interaction between the compressive resistance (P_r) and moment resistance (M_r)) of each wall was constructed by satisfying the conditions for equilibrium of forces and compatibility of strains for the constitutive models outlined in CSA S304.1 at various levels of load eccentricity. The tensile resistance of masonry in flexure as well as the stress contribution of reinforcing steel in compression were neglected.

The levels of load eccentricity were varied by changing the depth to the neutral axis (c) of the assumed internal stress distribution incrementally. The ultimate limit state of the wall was used for all cases by setting the value of strain in the extreme compression fibre of the masonry to 0.003 (maximum allowable strain in masonry from CSA S304.1). Following recommendations from S304, the values in Table 3 were assumed for all cases:

Table 3: Constants for S304.1 analysis

Variable	Definition	Value	Source
b	Width of the masonry section under consideration	1000mm	Arbitrary value
E_s	Young's modulus of reinforcing steel	200GPa	CSA S304
f_y	Yield stress for reinforcing steel	400MPa	CSA S304
f'_{m-g}	Specified compressive strength of grouted masonry assembly	7.5 MPa	CSA S304
f'_{m-h}	Specified compressive strength of hollow masonry assembly	9.8MPa	CSA S304
t	Total CMU thickness	190mm	CSA S304
t_f	CMU face shell thickness	32mm	Expocrete (2012) data sheet
t_w	Total web thickness	195mm/m	Expocrete (2012) data sheet
β_1	Ratio of the depth from of the equivalent rectangular stress block to the distance from the extreme compression fibre to the neutral axis	0.8	CSA S304
ϵ_m	Maximum allowable strain in a masonry specimen	0.003	CSA S304
ϵ_v	Yield strain for reinforcing steel	0.002	CSA S304
ϕ_m	Masonry material resistance factor	0.6	CSA S304
ϕ_s	Steel material resistance factor	0.85	CSA S304
χ	Factor accounting for the direction of the compressive force relative to the bed joint of the masonry section	1	Orientation being analysed

f'_m and A_e varied from case to case according to n_{gc} and equations (1) and (2):

$$f'_m [MPa] = f'_{m-g} + \frac{(f'_{m-h} - f'_{m-g}) n_{gc}}{5} \quad (1)$$

$$A_s [mm^2] = 2t_f b + (t - 2t_f) \left(t_w + \frac{(b - t_w) n_{gc}}{5} \right) \quad (2)$$

For each value of “c”, equations (3) to (14), derived from the CSA S304.1 design code using the equivalent rectangular masonry stress distribution, were solved sequentially to satisfy conditions of equilibrium of forces and compatibility of strains:

$$P_{rmax} = 0.8(0.85\phi_m f'_m A_s) \quad (3)$$

$$\varepsilon_s = \left(\frac{d\varepsilon_m}{c} \right) - \varepsilon_m \quad (4)$$

$$T = \varepsilon_s EA_s \quad (5)$$

$$a_1 = \min \left\{ \max \left\{ \begin{matrix} t_f \\ \beta_1 c - 190 + t_f \end{matrix} \right\} \right\} \quad (6)$$

$$a_2 = \min \left\{ \begin{matrix} t_f \\ \beta_1 c \end{matrix} \right\} \quad (7)$$

$$a_w = \left(t_w + \frac{n_{gc}(b - t_w)}{5} \right) \times \max \left\{ \min \left\{ \begin{matrix} 0 \\ 190 - 2t_f \\ \beta_1 c - t_f \end{matrix} \right\} \right\} \quad (8)$$

$$C_1 = 0.85\phi_m \chi f'_m a_1 b \quad (9)$$

$$C_w = 0.85\phi_m\chi f'_m a_w b \quad (10)$$

$$C_2 = 0.85\phi_m\chi f'_m a_2 b \quad (11)$$

$$C = C_1 + C_w + C_2 \quad (12)$$

$$P_r = \max \left\{ \min \left\{ \begin{array}{l} 0 \\ P_{rmax} \\ C - T \end{array} \right\} \right\} \quad (13)$$

$$M_r = C_1 \left(d - 190 + t_f - \frac{a_1}{2} \right) + C_w \left(d - \left(t_f + \frac{a_w}{2 \left(t_w + \frac{n_{gc}(b-t_w)}{5} \right)} \right) \right) + C_2 \left(d - \frac{a_2}{2} \right) + P_r \left(d - \frac{190}{2} \right) \quad (14)$$

P_r and M_r values were calculated for values of “c” ranging from approximately zero to 250mm at intervals of 1mm; corresponding values of P_r and M_r for the various configurations studied are displayed as interaction curves in Figure 9, Figure 10, and Figure 11. Note that the P_{rmax} values are dependant only on the masonry strength and effective area (f'_m and A_e) and are therefore identical for walls of the same dimensions, grouting, and strength. The area enclosed by the vertical and horizontal axis and the interaction curve is a representation of the range of values of compression and bending a wall can resist. Additional area enclosed by the reinforced SRCMU system interaction curve beyond the area enclosed by the conventional system interaction curve demonstrates the additional capacity of SRCMU systems.

Figure 9 illustrates the largest gain achievable with the SRCMU over conventional hollow concrete masonry systems. Since grouting of cores is the only conventional method for bonding reinforcing bars to hollow CMU walls, a vertically reinforced ungrouted masonry wall cannot be achieved by conventional means. For loading conditions with high out-of-plane flexural loads,

but low live and sustained axial loads, the fully reinforced SR/1000/0 demonstrates flexural resistance levels over five times that of the unreinforced C/0/0.

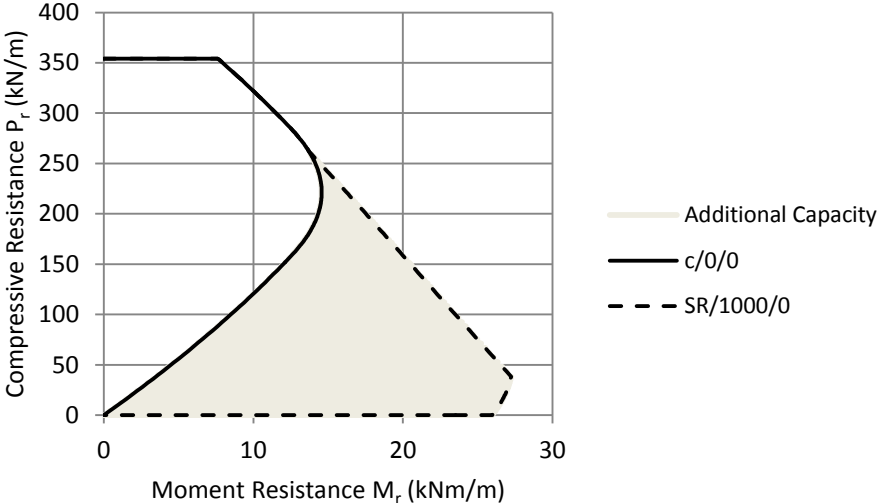


Figure 9: Interaction diagram; ungrouted walls

Figure 10 compares two fully grouted wall systems with the same area of reinforcing steel per meter length of wall. It is interesting to note that although the SR/500/5 wall has only half of its reinforcing bars engaged in tension, their location near the ultimate tension fibre results in an increase of 35% in maximum moment resistance for the SR/500/5 when compared to the C/500/5.

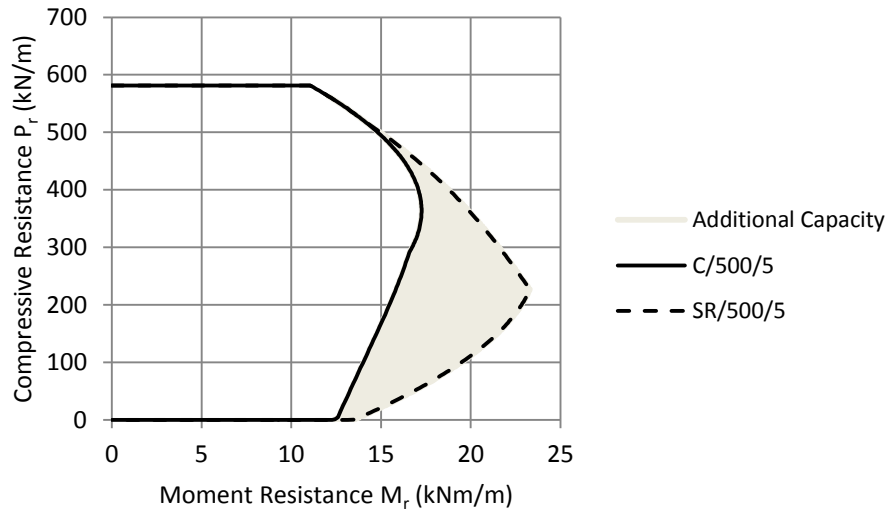


Figure 10: Interaction diagram; fully grouted walls

Less improvement in performance occurs at intermediate levels of grouting and reinforcement as can be observed in Figure 11. However, in all cases, analysis from CSA S304.1 indicates SRCMU masonry systems have the potential to perform equally well or better than conventional masonry systems.

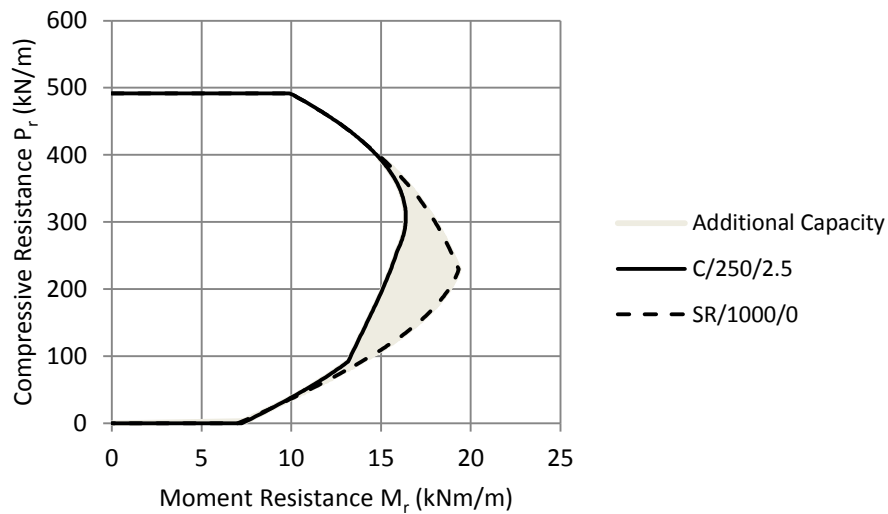


Figure 11: Interaction diagram; partially grouted walls

In addition to increased flexural strength, the SRCMU system displays greatly increased flexural stiffness. Following the initial cracking of a reinforced masonry system, the flexural stiffness is governed by the stiffness of the tension reinforcing material, as well as its cross-sectional area and distance from the neutral axis. Flexural stiffness increases linearly with respect to stiffness and cross-sectional area of tension reinforcement, but exponentially with respect to the distance between the centroid of the reinforcement and the neutral axis of the cracked section. This means, that although half of the reinforcing bars in the SRCMU system contribute very little to the flexural stiffness of the system, the placement of the remaining reinforcing bars near twice the distance from the neutral axis of the cracked section when compared to conventionally reinforced concrete masonry, results in an increase in flexural stiffness on the order of 100%.

In other words, assuming:

Stiffness, k_c , is directly proportional to $A_s E_s d^2$

Where A_s is the cross-sectional area of reinforcement in tension, E_s is the modulus of elasticity of the reinforcement in tension, and d is the distance from the neutral axis of the cracked masonry section to the centroid of the reinforcing bar.

If the stiffness of a conventional masonry wall, k_c , is:

$$k_c \propto A_s E_s d^2 \quad (15)$$

And the stiffness of an SRCMU wall, k_{srcmu} wall is:

$$k_{srcmu} \propto \frac{A_s}{2} E_s (2d)^2 \quad (16)$$

The net improvement in stiffness will be is expected to be on the order of two-fold:

$$\frac{k_{srcmu}}{k_c} \approx \frac{\frac{A_s}{2} E_s (2d)^2}{A_s E_s d^2} = 2 \quad (17)$$

$$\frac{k_{srcmu}}{k_c} \approx 2 \quad (18)$$

1.3 Construction materials reduction and sustainability

Global concerns over excessive and unnecessary energy expenditures and greenhouse gas emissions have been steadily growing over the past few decades. Governments world-wide have been imposing ever stricter regulations on energy efficiency and greenhouse gas emissions, while simultaneously businesses in various sectors have voluntarily (either through altruistic self-motivation, or because of pressure from their concerned customers) sought to decrease their energy and carbon footprint. The SRCMU is well placed to fit within this new mandate, and help the construction sector gain a position as leader when it comes to innovation to reduce humankind's impact on our shared environment.

1.3.1 Embodied energy (EE) vs. operating energy (OE)

Energy expenditures and greenhouse gas (GHG) emissions associated with structural systems can be subdivided into two main categories: Embodied Energy/Emissions (EE/EC) and Operating Energy/Emissions (OE/OC). Although the specific products and activities included in EE/EC and OE/OC varies greatly between research groups, EE/EC may be said to include energy expenditures or emissions associated with the construction of, and major renovations to a structure, including all the direct and indirect energy requirements for the products used during the construction process (whether or not to include energy expenditure for demolition and final disposal appears to be a contentious issue); OE/OC may be defined as the sum of the energy requirements or emissions associated with the maintenance of the structure, as well as for climate

control and other requirements for the proper operation of the structure during its useful life. Crawford and Treloar (2003) indicated that in Australia EE for a structure is typically 20 to 50 times its annual OE, from which it may be grossly extrapolated that in developed countries, over a structure's lifecycle, EE would likely account for roughly 15% to 70% of the total energy and emissions associated with a structure from cradle to grave.

In order to appropriately track the effects of design decisions on EE/EC and OE/OC for a project, much effort has gone into developing strategies to easily and consistently quantify energy usage and GHG emissions. Tracking OE over a structure's lifespan is usually relatively straight forward as it is usually governed by the quantity of energy used (which is metered at the inlet by the distribution company) and the average emission levels for the source energy, which is also easily estimated based on the method of generation. EE/EC is more challenging to accurately quantify as many steps exist in the fabrication of a structure, from the extraction and purification of primary minerals, to the manufacture of structural materials (such as cement, steel, lumber, and aggregate), to the production of structural and non-structural building products (such as precast concrete elements, steel girders, drywall, and carpeting), to the final assembly and finishing of each component.

Research articles such as Fay et al. (2000), Crawford and Treloar (2003), Goggins et al. (2010), and Jiao et al. (2012) discuss various methods for estimating EE/C for various types of structures in different parts of the world. Also helping to simplify the quantification of EE/EC for structures are libraries of EE/EC for various construction materials such as Bath University's Inventory of Carbon and Energy (ICE) (Hammond and Jones, 2008), which however require constant updating, and are only valid for the region for which they are intended as raw material

availability, production methods, and energy generation methods may differ greatly from country to country.

It is nonetheless widely agreed upon that the use of cement (such as in conventional reinforced concrete) is a major contributor to the EE and particularly EC of typical structures. In fact, a 2007 IPCC report (Bernstein et al., 2007) indicates that in 2003, cement production accounted for 5% of global CO₂ emissions.

The SRCMU system promises to reduce both EE/EC and OE/OC; lower material use and greater structural efficiency, as well as the potential for better insulating properties (operating energy efficiency) has the potential to greatly reduce the total energy and emissions associated with masonry structures. Masonry structures in general offer greater durability when compared to wood-framed structures, meaning their greater EE/EC can be distributed over a longer period of time.

1.3.2 Use of recycled and waste materials

One important method by which a structure's EE/EC may be reduced is by implementing the use of waste material, assumed to have negligible EE/EC into the structure as no additional energy has been used to produce them. A prime example of this in common use today is the partial replacement of cement powder in concrete with industrial waste materials such as fly ash and ground granulated blast furnace slag, which act as supplementary cementing materials.

Cabeza et al. (2013) discuss many cement substitution strategies that can contribute to reducing the EE/EC in concrete products. They note that the introduction of pozzolans such as fly ash can require high temperature curing, which is often a barrier for field application, but is not a problem when it comes to concrete block production. Haber and Roussel (2009) further indicate that EC reductions on the order of 15% could be achieved by increasing cement

substitution in France (where substitution was already common in some applications. Indeed many concrete block producers currently incorporate fly ash into their concrete mix designs.

1.3.3 Decreased use of materials

In some situations, replacement of high EE/EC materials with materials of lower EE/EC may be impractical, or insufficient to obtain the energy targets for a project. In such cases, decrease in overall material consumption may be desirable. Daminieli et al. (2010) propose such an alternative to substitution of cement powder; they found that with high strength modern concrete mix designs, cement powder can be used very efficiently in terms of cement concentration per MPa of concrete strength. In their report the term b_i is used to indicate binder intensity in units of $\text{kg m}^{-3}\text{MPa}^{-1}$ where the mass is that of cement binder, the volume and strength (pressure) is that of the finished concrete. They further indicate that conventional 20MPa concrete has a minimum b_i value of $15\text{kgm}^{-3}\text{MPa}^{-1}$ as compared to higher strength concrete which had minimum b_i values around $5\text{kgm}^{-3}\text{MPa}^{-1}$. Habert and Roussel (2009) also indicated it may be possible that although high strength concretes incorporate higher levels of cement into their mix, an over-all reduction in EE/EC may result from the reduction in necessary material usage due to its higher strength.

Along these lines, the SRCMU system proposes to replace grout-filling of the cores of hollow masonry systems with epoxy-grouting of reinforcing bars into specially designed channels. Using values from the Bath University's ICE it is possible to prepare a rudimentary comparison between the EE/EC of conventional masonry systems with grouted cores to the SRCMU system with epoxy-filled channels, for both energy and CO_2 emissions. Table 4 shows the values used for the comparison; a standard 190mm wall thickness was assumed.

Table 4: Embodied energy of conventional grouting vs. SRCMU epoxy grouting

Conventional		
Variable	Value	Explanation
Embodied Energy of grout	0.7 MJ/kg	ICE
Embodied Carbon of grout	.11kgCO ₂ /kg	ICE
Grout density	2200 kg/m ³	typical
Volume of grout per m ² of wall	.095 m ³ /m ²	Assume 50% hollow CMUs
<i>Total EE</i>	<i>146 MJ/m²</i>	
<i>Total EC</i>	<i>23.0 kgCO₂/m²</i>	
SRCMU		
Variable	Value	Explanation
Embodied Energy of grout	137 MJ/kg	ICE
Embodied Carbon of grout	5 kgCO ₂ /kg	ICE
Epoxy density	1200 kg/m ³	Typical value
Volume of epoxy per m ² of wall	.002285 m ³ /m ²	Assuming 100mm ² reinforcing bars and 50% filler within epoxy resin
<i>Total EE</i>	<i>375 MJ/m²</i>	
<i>Total EC</i>	<i>13.7 kgCO₂/m²</i>	

From this rudimentary calculation, some increase in embodied energy appears to be likely with the adoption of the SRCMU system, however a net reduction in embodied CO₂ is also observed. It is also important to note that other benefits of the SRCMU system, such as decreased weight and accelerated construction time may also incur large reductions in EE/EC when compared to conventional hollow masonry systems. Furthermore the values in Table 4 assume the reinforcement channels are completely filled with epoxy; in practical applications, the surface portion of the channels would most likely be filled with a more esthetically pleasing mortar, thus reducing the required volume of epoxy per square meter of wall.

1.3.4 Decrease energy input during construction

The total EE/EC of a structure does not only include the sum of the EE/EC for the construction materials used, but must also include energy expenditures and GHG emissions incurred during the construction process. Typical construction practice for conventional hollow masonry construction includes the filling of hollow masonry cores with grout in order to bind the

reinforcing bars to the masonry system; this activity require specialized concrete pumping equipment. Masonry contractors therefor will wait until several masonry walls are erected before bringing in the equipment to grout-fill them all at once. During winter construction, this means that erected masonry walls need to be continuously heated until sufficient walls are built to undergo the grouting procedure. The SRCMU system would make it viable to reinforce the masonry walls as soon as they are built, greatly decreasing the length of time during which walls must be heated. Furthermore, since the mass of epoxy necessary to reinforce the SRCMU system is far lesser than that of grout for conventional masonry systems, savings in transportation energy and emissions would likely be incurred as well.

1.3.5 Operating energy

A large portion of operating energy is allocated to heating and cooling of structures for the thermal comfort of the occupants. When outdoor temperatures deviate from roughly 20°C, Heating, Ventilation, and Air Conditioning (HVAC) costs are largely dependent on the insulating capacity of the building envelope. By inserting foam insulation into the hollow cores of the SRCMU wall systems, an increase in R-value may be achieved. Based on values from coloradoENERGY.com a comparison between a solid grouted CMU wall and an insulated SRCMU wall can be made. In Table 5, values from ColoradoENERGY.org are converted to SI units.

Table 5: Insulation characteristics of concrete and polyurethane foam

Characteristic	Value (for 1mm thickness)
R – concrete	.0005543 m ² K/W
U – concrete	1804 Wm ⁻² /K
R – formed in place polyurethane	.04331 m ² K/W
U – formed in place polyurethane	23.09 Wm ⁻² /K

For the comparison, the conventional grouted masonry system is assumed to have an R-value equivalent to that of concrete as shown in equation (19).

$$R_{\text{conventional CMU}} = 0.0005543 \left[\frac{m^2 K}{Wmm} \right] \times 190[mm] = 0.105 \left[\frac{m^2 K}{W} \right] \quad (19)$$

For the SRCMU system composite action is assumed. CMU webs constitute 19.5% of the length of each CMU at its centre (as mandated by CSA A179), and are assumed to constitute 50% of the length of each CMU for the first 10mm from each face shell. Three R-values must therefore be determined; that of concrete face shells, that of the composite insulation-concrete system near the faceshells and that of the composite insulation-concrete system at the centre of the web as shown in equations (20) to (23).

$$R_{\text{faceshell}} = 0.0005543 \left[\frac{m^2 K}{Wmm} \right] \times 64[mm] = 0.0355 \left[\frac{m^2 K}{W} \right] \quad (20)$$

$$R_{\text{near faceshell}} = \frac{1}{20[mm] \left(0.5 \times 1804 \left[\frac{mmW}{m^2 K} \right] + 0.5 \times 23.09 \left[\frac{mmW}{m^2 K} \right] \right)} = 0.0219 \left[\frac{m^2 K}{W} \right] \quad (21)$$

$$R_{\text{webregion}} = \frac{1}{106[mm] \left(0.195 \times 1804 \left[\frac{mmW}{m^2 K} \right] + 0.195 \times 23.09 \left[\frac{mmW}{m^2 K} \right] \right)} = 0.286 \left[\frac{m^2 K}{W} \right] \quad (22)$$

Therefore

$$R_{\text{SRCMU}} = 0.0355 \left[\frac{m^2 K}{W} \right] + 0.0219 \left[\frac{m^2 K}{W} \right] + 0.286 \left[\frac{m^2 K}{W} \right] = 0.343 \left[\frac{m^2 K}{W} \right] \quad (23)$$

This represents a three-fold increase in R-value for the wall system. It should however be noted that if the same volume of insulation as is required to fill the cores of the SRCMU wall were placed in a continuous layer outside the wall, the R-value of that insulation alone would be approximately 4.13m²K/W.

1.3.6 Near-surface mounted reinforcing bars

NSM reinforcement is a technique by which a narrow channel is cut into an existing structural element in order to embed a reinforcing bar into its surface. It is a re-immersing technology, particularly useful as an alternative to surface mounted reinforcement when retrofitting heritage structures in order to increase their flexural load-bearing capacity (e.g. (Derakhshan et al. 2014), (Dizhur et al. 2014), and (Tumialan et al. 2001), or to increase the useful service life of modern infrastructure (e.g. (Tumialan et al. 2007) and (Täljsten et al. 2003)). Most often cited as the earliest example of NSM reinforcement in a structure is Asplund's (1949) report of the American Concrete Institute; this report describes the retrofitting of a reinforced concrete bridge in which the original reinforcing bars were incorrectly located. Additional reinforcing bars were installed by cutting channels into the concrete deck of the bridge and grouting them in place with a cement-based grout. Little further scholarly research can be found on the subject of NSM reinforcement applications until the early 2000s. More recent studies have closely examined the characteristics of the bond between NSM reinforcing members and the substrate to which it is applied (e.g. concrete or masonry), an important factor being the thickness of the bonding agent used. Of particular interest to this document are a selection of studies into the behaviour of concrete masonry reinforced with NSM (e.g. (Kashyap et al. 2011), (Petersen et al. 2010), (Dizhur et al. 2014), (Gustavo et al. 2002)).

1.3.7 NSM application case studies

In recent structural rehabilitation projects, NSM reinforcement is preferred over surface reinforcement applications for many reasons, including those listed by De Lorenzis and Teng (2007), i.e. decreased effort in surface preparation; ease of reinforcement anchorage into adjacent

elements; ease of prestressing; protection of the reinforcement afforded by the embedment cover; reduced aesthetic impact.

Derakhshan et al. (2014) describe a series of in-situ tests performed on unreinforced masonry (URM) structures in New Zealand. Test-walls having been previously exposed to earthquake loading over their service life were tested in out-of-plane flexure both in their original unreinforced condition and after being retrofitted with NSM carbon fiber reinforced polymer (CFRP) strips or twisted steel bars. An epoxy grout was used to bond the CFRP strips within the NSM grooves; a cementitious paste was used for the twisted steel bars. In all cases, the application of NSM reinforcement was found to substantially increase the flexural capacity and ductility of the test walls. NSM has also been successfully used as a rehabilitation method for heritage structures in New Zealand; for example Dizhur et al. (2014) discusses two heritage structures which have undergone targeted NSM retrofitting in order to preserve their heritage architecture; the parapets of a kindergarten building constructed in 1910 were fitted with NSM CFRP strips to increase their resistance to earthquake loading, and the chimneys of a tavern building constructed in 1886 were stabilised with the same technique to allow the entire structure to be relocated. Other reports such as Tumialan et al. (2001) indicate that NSM reinforcement retrofitting can be practical means of preserving both the function and aesthetics of heritage masonry structures.

Examples of rehabilitation projects for more modern structures such as parking structures (Tumialan et al. 2007) and concrete bridges (Täljsten et al. 2003) can also be found. These case studies further indicate NSM reinforcement's potential as an economical and effective structural reinforcement method.

1.3.8 Experimental laboratory studies

Within the last decade, a large volume of controlled laboratory studies have been published to aid in the understanding of the physical principles at work in NSM reinforced elements and structures. As NSM reinforcement can contribute greatly to structural elements under both in-plane, and out-of-plane loading conditions, two broad categories can be distinguished for the types of tests performed on NSM-reinforced laboratory specimens; shear-reinforced, and flexural-reinforced. Within these broad categories, the characteristics of the bond between the NSM reinforcement and the substrate, and its effect on the performance of a structural element are often studied in detail. The bulk of studies into applications of NSM reinforcement are intended for reinforced concrete substrates, however, some studies consider applications with fired clay brick and concrete masonry.

Barros et al. (2006) in their study of CFRP NSM shear reinforcement in beams were able to develop flexural shear strength in a reinforced concrete (RC) beam equal to that of conventionally reinforced beam with equivalent shear strengthening. Rahal and Rumaih (2011) also showed that significant gains in flexural shear strength may be achieved through the application of NSM steel or CFRP reinforcement to the webs of RC beams. Shear strengthening in masonry specimens has been studied for the most part in small wall specimens reinforced using an NSM reinforcement technique also known as structural repointing, by which the mortar in selected bed-joints within a wall are removed to a certain depth to form a channel into which reinforcing bars may be adhered. Turco et al. (2006), performed shear tests on 1.6mX1.6mX150mm hollow concrete block wall samples, reinforced by structural repointing; Petersen et al. (2010) performed shear tests on 1.2mX1.2mX110mm solid clay brick walls reinforced by structural repointing (horizontal), and NSM in saw cut grooves (vertical); Dizhur et

al. (2013) performed shear tests on 1.17mX1.15mX230mm and 350mm clay brick wall reinforced with NSM FRP strips placed into vertical and diagonal saw-cut channels. All three of these reports indicate major gains in shear strength and ductility of walls with NSM reinforcement when compared to unreinforced systems, however, none of them compared their results to conventionally reinforced masonry shear wall systems.

Various research groups also studied the effect of NSM reinforcement on the out-of-plane flexural resistance of URM walls (e.g. (Turco et al. 2006), (Derakhshan et al. 2014), (Dizhur et al. 2014), (Lunn and Rizkalla 2014), and (Kashyap et al. 2011)). Once again large gains in strength and ductility were observed when compared to unreinforced systems, however no comparison appears to be available between conventionally reinforced masonry walls and NSM reinforced URM walls.

Only one study was found concerning the application of NSM reinforcement to hollow concrete block walls; Carney and Myers (2003) compared the behaviour of hollow unreinforced concrete masonry walls, to walls retrofitted with surface-bonded FRP sheets as well as NSM FRP reinforcement when subjected to extreme out of plane (blast) loading. By comparing the scatter of debris of the various systems tested, the study found that surface-mounted FRP sheets worked best against the blast loads and that anchoring of the NSM FRP rods into the boundary elements was critical to the effectiveness of the system. No comparison of the performance of the NSM-reinforced system to conventional static loading was provided.

1.3.9 Numerical analysis of NSM reinforced systems

To better understand and predict the behaviour of structures retrofitted with NSM reinforcement, many research groups have attempted to simulate NSM reinforced structures through Finite Element Analysis (FEA). Critical to the FEA models is the load-slip behaviour of the NSM

reinforcement; given that the behaviour of NSM systems necessarily depends on the interaction of three dissimilar materials (concrete or masonry substrate, reinforcement bars, and grouting material) the load-slip interaction of reinforcing bars in NSM-reinforced systems is particularly complex.

Kashyap et al. (2011) list common modes of failure for NSM-reinforced flexural clay brick masonry elements, which include: intermediate crack debonding, flexural-shear cracking, FRP rupture, plate end debonding, sliding of the masonry units, perpendicular shear failure, and crushing of brick in compression. However, the load-deflection behaviour of NSM flexural elements prior to failure is largely influenced by the shear-slip interaction of the reinforcement bars.

The idealized bilinear shear-slip model is typically displayed as shown in Figure 12 has been employed in several studies (e.g. (Dizhur et al. 2014), (Petersen et al. 2010), and (Kashyap et al. 2011)) and is appropriate for modelling conditions in which progressive debonding of reinforcement occurs, and therefore no determinate development length exists (i.e. the shear resistance of the bar-substrate interface goes to zero after a certain amount of slip occurs). De Lorenzis and Teng (2007) in their review of NSM applications also outline a shear-slip model that includes a non-linear shear softening branch in which shear stress does not tend toward zero with increasing slip. This type of model is also employed in various studies including de Sena Cruz and De Barros (2004) and De Lorenzis et al. (2002). Note that the studies found during the literature review process focus on the shear-slip behaviour of FRP strips and bars used with an epoxy-based bonding agent.

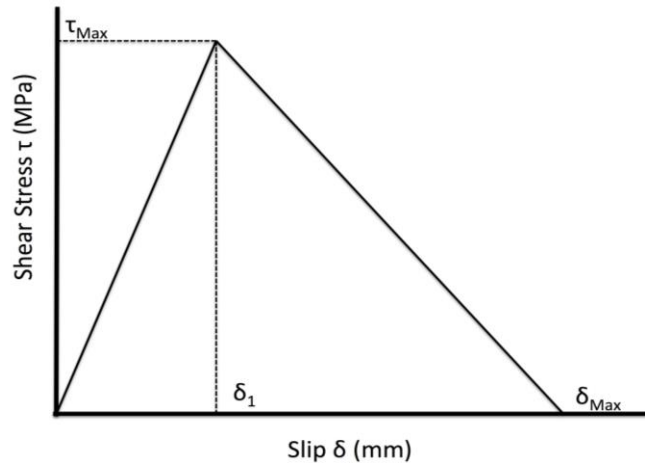


Figure 12: Generic bilinear shear-slip bond model

1.4 Commercial block production

Current production methods aim to produce an economic and environmentally friendly product and contribute to CMUs' particular strength, porosity and microstructure characteristics that have a marked effect on the structural properties of the CMUs as well as their interaction with other components within a masonry system. The production process is described by the Concrete Masonry Association of Australia (2000) and can be summarized as follows:

The components of a batch of concrete used for the casting of CMUs are measured and combined; these components include sand, coarse sand, Portland Cement, water, and supplementary cementitious materials such as fly ash, and water. The amount of concrete required to fill the mould is weighed and poured into the mould (a single mould will be used to cast 3-6 blocks at once). The mould is then vibrated while the concrete is compacted into the block mould by a heavy weight. The blocks are then immediately stripped from the mould and transported by conveyor to a curing chamber where the CMUs are steam cured before being stored outdoors to await shipment. All steps in this process are highly automated. The heavy

equipment used in this manufacture process makes it difficult to reproduce in a laboratory environment.

1.4.1 Mix design

To keep the cost of producing CMUs competitive with other construction materials as well as to decrease the environmental impact associated with CMU production, many producers incorporate supplementary cementitious materials (SCM) into the concrete mixes they use in production, as partial replacement of Portland Cement. In addition to commonly used SCMs such as fly ash and ground granulated blast furnace slag, other materials such as rice husk ash (Cook et al. 1977) and municipal solid waste bottom ash (Rashid and Frantz 1992) have also been explored. The main hurdle to increased use of pozzolanic SCMs in CMU production is the requirement for rapid strength gain. Since increasing curing time of the CMUs would result in an unacceptable decrease in plant capacity and increase in operating costs, the cementitious materials used must have the capacity to develop their design strength within the 24 hour steam curing time provided.

Also key to a suitable mix design is the over-all grading of the materials in the mix as well as their surface texture. Hüsken and Brouwers (2012) in comparing the effect of fly ash and quartz flour of similar particle size distribution on the green strength (green strength being the unconfined uniaxial strength of the material after casting and before any significant cement hydration occurs) of zero slump concrete noted that the spherical shape of the fly ash particles allowed greater compaction than the quartz flour and greater hardened strength after curing. However the particle interlock of the quartz flour imparted a higher green strength to the mix. The effect of increasing the proportion of cement powder on the maximum compaction of a concrete mix was studied by Hazaree et al. (2011). The authors noted that increasing cement

content increased the maximum dry density of their mixes up to cement contents of around 300 kg/m³ [18.7 lb/ft³] with decreasing maximum dry density for larger cement content values in mixes with similar water content.

For applications in CMU production, the goal is not necessarily to maximize strength or density, but to achieve an acceptable product at the lowest practical cost. Density and cement content therefore vary according to the required design strength of the blocks being produced. Green strength of the mix is judged by the capacity of the block to maintain its shape during transportation from the casting equipment to the curing chamber. The author was unable to find any guidance on typical levels of green strength. For the purposes of small-scale production in a laboratory environment, the capacity for immediate unmoulding of units is not a requisite property of the concrete mix being used.

1.4.2 Block casting

Casting of concrete blocks is done using specialized block-making equipment. The weight of concrete required to produce a set of blocks is automatically measured and poured into a set of moulds. The concrete is then consolidated by applying tremendous pressure and vibration. The cohesiveness and stiffness of the concrete mix is such that the freshly cast blocks can be immediately unmoulded while still retaining their shape.

1.4.3 Curing

Curing of CMUs is done at a high temperature and high levels of humidity in order to decrease the production time as well as decrease the footprint (area) of the curing chambers in a manufacturing facility while continuing to produce a product with consistent properties. It is well known that high temperature curing of concrete yields higher early strength, but lower strength gain as the concrete ages. Türkel and Alabas (2005) in their study of strength gain in composite

Portland Cement concrete, showed findings that suggest that nearly 100% of the 28 day strength of all their concrete mixes were achieved after 24 hours of moist curing at both 65°C and 85°C. However, these results were associated with final strengths as low as 40% lower than those observed for specimens moist cured at room temperature. Tan and Gjørsv (1996) observed a loss in strength of up to 15% for concrete cured at 65°C and up to 23% for concrete cured at 80°C when compared to concrete samples cured at 20°C. The authors also studied the effect of curing temperature on water and chloride penetration in hardened concrete, and although temperature appeared to have little effect on permeability to water, a large increase in permeability to chlorides was observed. This effect is suggested to be caused by the increased coarseness of the concrete paste caused by the rapid curing induced by the high temperature. A study by Patel et al. (1995) supports this theory with a microstructure analysis using both optical and electron microscopy. Concrete cubes cured at 85°C in which “a coarse texture was evident with concentrations of larger crystals in microcracks, especially those at the paste/aggregate interface, and in air voids” were documented.

2 Chapter 2 – Experimental Phase 1: Block Fabrication

The SRCMU is not yet commercially available, it was therefore necessary to produce them in laboratory; however the properties of the product produced in laboratory had to closely match those of commercially produced CMUs. As the compacting methods used for commercial production of CMUs, requiring pressure and vibration that could not be applied in the laboratory, a unique mix design and concrete consolidation technique was developed.

The experimental work for this study was performed in three phases which are described in Chapters 2, 3, and 4. The first experimental phase, described in this chapter, discusses the laboratory manufacturing process of the masonry units. The second experimental phase, discussed in Chapter 3, shows that CMUs produced in Phase 1 perform similarly to those produced commercially. The third experimental phase makes use of the blocks validated in Phase 2 to test the performance of reinforced SRCMU assemblies. The fourth and final experimental phase consists of numerical FEA of the tests performed in Phase 3.

2.1 Manufacture of concrete block moulds

For ease of construction and assembly, and to control experimental costs, the moulds used for the production of all laboratory-cast concrete blocks were made from 19mm formwork plywood. To facilitate the extraction of the finished blocks, the moulds were made in 6 parts as shown in Figure 13. The mould parts used to form the vertical exterior faces of the blocks were fitted with protruding elements to form the vertical exterior channels including the frogs, and central reinforcement channels and partial side channels. The protruding elements were manufactured from pine studs. The mould parts used to form the hollow cores of the blocks were made from stacked sections of 19mm formwork plywood bonded together with carpenter's glue. Alignment

holes incorporated into the cutting pattern of each plywood section allowed precision alignment of the pieces making up the core mould parts. The properly aligned and glued cross sections were clamped for at least 30 minutes as per the glue manufacturer's recommendation. The stepped surfaces of the completed stacks were smoothed using a sanding block, then fully covered in a moisture repellent adhesive tape.

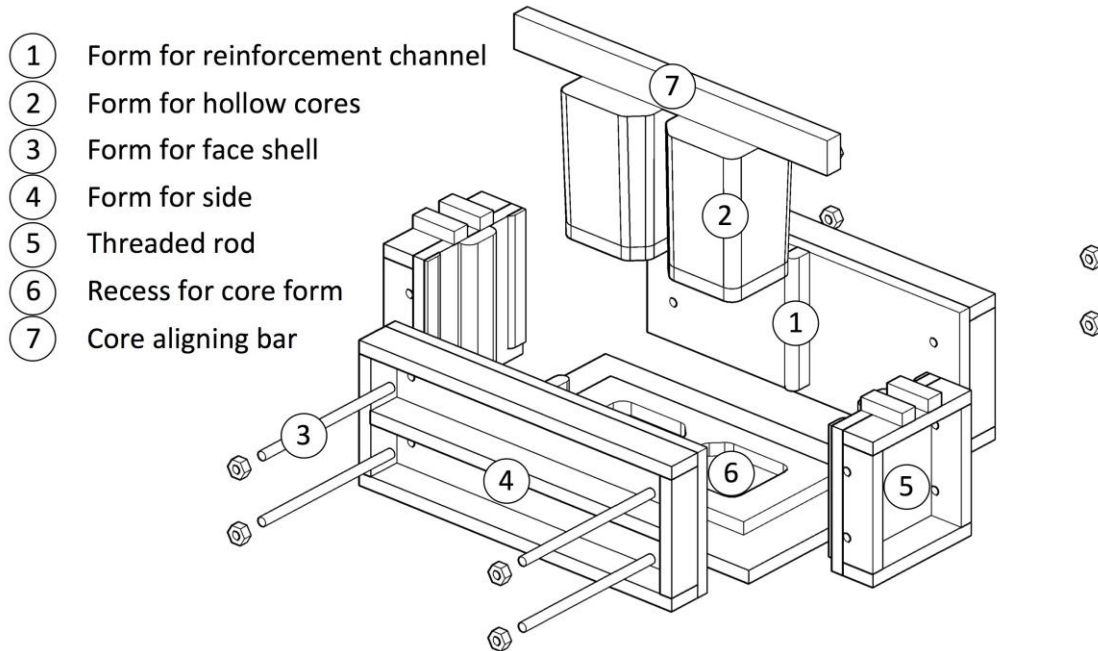


Figure 13: SRCMU mould; exploded view

All plywood pieces were cut precisely to size by a Computer Numeric Controlled (CNC) milling machine. All protruding elements were fabricated with a combination of hand and power tools. Alignment holes were incorporated into the sides of the moulds in order to allow the four mould parts forming the four vertical faces of the blocks to be securely aligned and tightened together for casting using 12.5mm threaded rod. The mould parts forming the hollow cores of the blocks were held in place at the top by an aligning bar member and at the base by recesses in the mould part forming the base of the block.

Given that every fabricated mould segment varied slightly from the design dimensions, small adjustments were necessary during assembly. To ensure consistency in dimensions of the concrete blocks produced, each mould segment was adjusted to fit precisely within a specific set of segments to precisely form a complete mould; each mould segment was then given a unique alphanumeric identifier to ensure it was only used within the set of segments to which it had been adjusted.

Each assembled mould was then assigned an identifying alphabetical letter, A, B, C, D, E, F, G, or H. Moulds A, B, and D were constructed to form conventionally shaped CMUs; moulds C, E, F, G, and H were constructed to form SRCMUs.

2.2 Development of a concrete mix design for casting CMUs in laboratory

As a starting point for the development of a mix design for the laboratory-produced concrete blocks, a proprietary mix design was obtained from a local concrete block manufacturer. This mix was used to produce a series of standard concrete test cylinders (100mm diameter, 200mm height) with varying water content. Six cylinders each were produced from concrete batches with water to cement ratios (w/c) of 0.25, 0.30, 0.35, 0.40, and 0.45 by mass.

The concrete mixes produced were very dry and did not exhibit a measurable slump, the standard consolidation method for concrete test cylinders outlined in CSA A23.2 therefore needed to be modified in order to cast the test cylinders; the procedure employed to produce the test cylinders is outlined in Section 2.2.1.

2.2.1 Production of dry-mix concrete cylinders

Materials batching:

The mass of each material was determined according to the volume of concrete necessary for casting while maintaining the proportions of the concrete mix design. The necessary mass of

each dry component was weighed to the nearest 5g and dispensed separately into buckets. The necessary mixing water was weighed to the nearest 1g and dispensed into a separate bucket. Note that the moisture content of the sand and aggregate components was determined using the procedure outlined in Section 2.3.2. The moisture fraction from the sand and aggregate was subtracted from the mixing water for each mix.

Concrete mixing:

Concrete mixing was done by hand in a mixing basin using a shovel. The dry components including sand, aggregate and cement powder were poured into the mixing basin and thoroughly blended. Mixing water was introduced gradually to the mix while mixing continued for approximately ten minutes until a homogenous blend was achieved.

Casting:

Concrete casting was done in three equal lifts into 100mm diameter and 200mm height cylindrical polymer moulds. Each lift was rodded 25 times per lift with a 10mm rod then tamped down using a 19mmX25mmX300mm plywood stick. The top surface of every specimen was trowelled smooth, then covered with a cylinder cap and allowed to set overnight (approximately 16 hours).

Curing:

Three specimens from each mix were allowed to remain covered and in their respective non-porous moulds for 14 days at ambient laboratory temperature ($21\pm 2^{\circ}\text{C}$) until testing. Remaining cylinders were unmoulded and cured in a warm water bath for 22 hours. The water temperature as recorded over the curing period is shown graphically in Figure 14. Moist-cured cylinders were allowed to dry at ambient temperature and humidity for 7 days before testing.

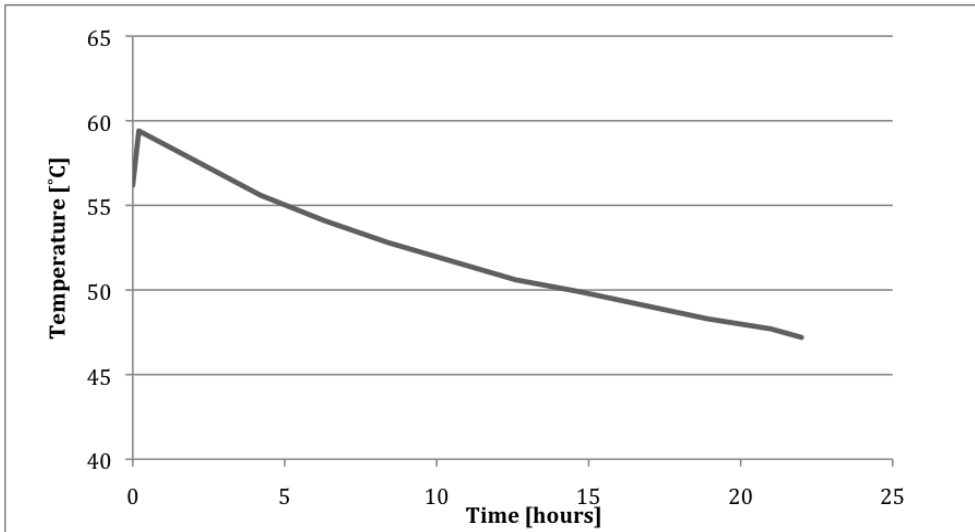


Figure 14: Curing water bath temperature

2.2.2 Outcomes from dry-mix concrete casting

Cylinders produced for this first trial had strength levels well below that required for the production of concrete blocks. In fact all 30 cylinders manifested strength levels below that which could be accurately measured utilizing the available laboratory testing equipment. Visual inspection of the test cylinders suggest the poor cohesion of the concrete specimens was most likely due to poor consolidation (as exhibited by the open pore structure and grainy appearance of the test cylinders seen in Figure 15).



Figure 15: Low cohesion of poorly consolidated commercial concrete mix

2.2.3 Workable concrete mix for concrete block production

From the information gathered from the first set of test cylinders, a modified concrete mix was conceived which included fly ash as well as type HE cement for a larger fines content in the mix, and a much higher water to cement ratio. The fly ash was introduced to act as a lubricant for the mix, allowing greater consolidation at moderate w/c levels. The final proportions for the concrete mix are shown in Table 6.

Table 6: Concrete mix proportions

Material	Proportion (kg/m ³)
Type HE cement (P_c)	210
Fly Ash – class F (P_f)	105
Sand (P_s)	1850
Aggregate (P_a)	65
Mixing water (P_w)	236

For simplicity, neither steam curing, nor hot water bath curing was employed for the production of laboratory-cast masonry units. As speed of production was less critical for this experimental program than it is for mass production of CMUs, curing was done in a curing chamber at $21^{\circ}\text{C}\pm 1$ and 100% relative humidity over 7 days.

The procedure employed for the casting of concrete test cylinders and concrete blocks using the final mix design is outlined in Sections 2.3.3 to 2.3.5.

2.3 Block production

The production of blocks was divided into four separate activities; preparation of the moulds, concrete mixing, concrete casting, and unmolding and curing. Each activity is discussed separately. Concrete test cylinders were cast along with select batches of blocks to ensure consistency in concrete properties.

2.3.1 Preparation of moulds

After each casting, all moulds were cleaned of concrete residue and inspected for damage. Any damage identified was immediately corrected prior to reassembly of the mould. Typical damage included tearing of the waterproof adhesive tape and, rarely, delamination of the plywood sections constituting the mould sections for the casting of the hollow cores of the blocks. Any location where damage occurred to the adhesive tape was stripped of tape and appropriately recovered. If delamination of a mould section occurred, that section was disassembled, sanded and re-glued under appropriate clamping to restore its original properties.

Once all sections of the moulds were cleaned, inspected, and appropriately repaired, reassembly of the moulds could commence. Every surface of each mould section that would be exposed to fresh concrete was lightly brushed with a mould release compound. The four sides of the mould were connected together by inserting a 12.5mm ($\frac{1}{2}$ ") threaded steel rod into the appropriate holes as shown in Figure 16 and tightening the nuts to, at once, clamp the four sides together, and hold them to the base of the mould by friction. The core mould segments were then inserted in the appropriate location. Friction between the core mould segments and the alignment slots was sufficient to completely restrain them.

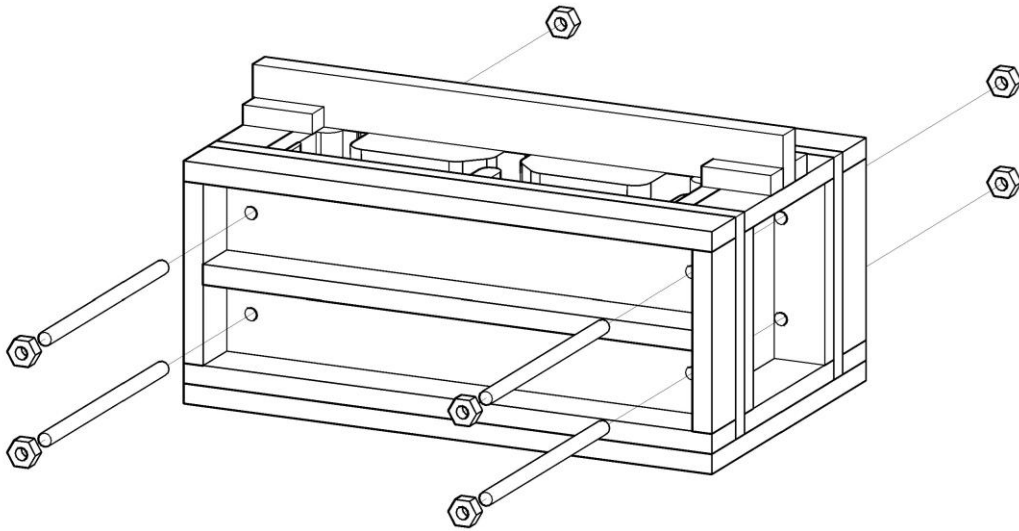


Figure 16: SRCMU mould; threaded rod alignment

2.3.2 Determination of moisture content for sand and aggregate (based on ASTM C566)

The moisture content of the aggregate and sand was determined at least twice weekly during casting.

Sample collection:

The aggregate to be used for casting is thoroughly mixed to ensure even distribution of moisture within the sample. A clean steel tray is weighed to the nearest 0.01 gram; this mass is recorded as W_{tare} . A sample of at least 1 kg of material is then collected into that steel tray. The aggregate container is then sealed to avoid subsequent moisture loss. The tray and moist aggregate are weighed together to the nearest 0.01 gram; this original mass is recorded as W_o .

Sample drying:

The metal tray is then placed in a ventilated drying oven at 110°C for 24 hours. The sample and tray are then weighed to the nearest 0.01 g, and returned to the drying oven for an additional 1

hour. Weight readings are taken every hour until two successive readings show a difference in weight of no more than 0.01%; this mass is recoded as W_d .

Moisture content calculation:

Moisture content (μ) is calculated as using equation (24).

$$\mu = \frac{W_o - W_d}{W_o - W_{tare}} \quad (24)$$

2.3.3 Concrete batching and mixing

Materials batching:

The necessary mass of each dry component is weighed to the nearest 5g and dispensed separately into buckets. The necessary mixing water is weighed to the nearest 1g and dispensed into a separate bucket. Note that the moisture content of the sand and aggregate components were determined using the procedure outlined in Section 2.3.2. The moisture fraction from the sand and aggregate are subtracted from the mixing water for each mix.

Concrete blocks were cast in two batches; only concrete sufficient to cast four concrete blocks was mixed at once. In this manner, less than one hour was allowed to pass between the initial contact of mixing water with the cementitious materials and casting so that the fresh properties of the concrete were maintained throughout the casting of a single batch of concrete. Additional concrete for the production of 4 test cylinders was provided for the first four and final four batches of concrete produced.

A batching factor of 1.025 was used in order to limit wastage during casting. The variables in Table 7 were used to calculate the necessary mass of each component for a given batch of concrete. An example of the mass measurements of materials used in a batch of concrete

mix, along with associated calculations is outlined below. Mass proportions are calculated with equations (25) to (30).

Table 7: Concrete batching variables

M_a	Mass of aggregate
M_c	Mass of cement powder
M_f	Mass of fly ash
M_s	Mass of sand
M_w	Mass of water
P_a	Proportion of aggregate (from Table 6)
P_c	Proportion of cement (from Table 6)
P_f	Proportion of fly ash (from Table 6)
P_s	Proportion of sand (from Table 6)
P_w	Proportion of water (from Table 6)
V_b	Gross batch volume
V_t	Factored total batch volume
α_b	Batching factor
μ_a	Moisture content of aggregate
μ_s	Moisture content of sand

$$V_t = \alpha_b V_b \quad (25)$$

$$M_c = P_c V_t \quad (26)$$

$$M_f = P_f V_t \quad (27)$$

$$M_a = \frac{P_a V_t}{(1 - \mu_a)} \quad (28)$$

$$M_s = \frac{P_s V_t}{(1 - \mu_s)} \quad (29)$$

$$M_w = P_w V_t - (M_s \mu_s + M_a \mu_a) \quad (30)$$

For example, on May 26th, 2014, the values in Table 8 and proportions from Table 6 were used to develop the mix in Table 9 and cast two batches of 4 blocks each.

Table 8: 2014-06-26 concrete mix variables

Variable	2014-06-26 Value
α_b	1.025
V_b	.0308m ³
μ_a	.040
μ_s	.052

$$V_t = 1.025(0.0308\text{m}^3)$$

$$V_t = 0.0316\text{m}^3$$

$$M_c = 210\text{kg/m}^3(0.0316\text{m}^3)$$

$$M_c = 6.630\text{kg}$$

$$M_f = 105\text{kg/m}^3(0.0316\text{m}^3)$$

$$M_f = 3.315\text{kg}$$

$$M_a = 65\text{kg/m}^3(0.0316\text{m}^3)/(1-0.040)$$

$$M_a = 2.135\text{kg}$$

$$M_s = 1850\text{kg/m}^3(0.0316\text{m}^3)/(1-0.052)$$

$$M_s = 61.625\text{kg}$$

$$M_w = 236\text{ kg/m}^3(0.0316\text{m}^3) - (61.625\text{kg}(0.052) + 2.135(0.040))$$

$$M_w = 4.320\text{kg}$$

Table 9: 2014-06-26 concrete mix component mass

Component	2014-06-26 Mass [kg]
M_c	6.630
M_f	3.315
M_a	2.135
M_s	61.625
M_w	4.320

Note that the mass of each component was determined to the nearest 5g which corresponds to the sensitivity of the scale used to weigh the materials.

Concrete mixing:

Concrete mixing was performed with the vertical axis electric concrete mixer shown in Figure 17. The sand and aggregate were poured into the dry mixer and thoroughly blended. The mixer was then stopped in order to introduce the cement powder and fly ash. All dry components were blended for approximately one minute before gradually introducing the mixing water; mixing water was introduced to the mixer while in operation at a steady rate over approximately one minute. The concrete was then blended for an additional two minutes, intermittently reversing the direction of mixing to ensure a homogenous blend was achieved.



Figure 17: Vertical axis electric concrete mixer

2.3.4 Concrete casting

Concrete casting was done in three equal lifts. For the concrete blocks (both conventional shape and SRCMU), each lift was rodded 40 times with a 16mm diameter steel rod, then the mould was vibrated on a vibrating table for 3 seconds to ensure proper consolidation. Concrete cylinder samples were cast in three lifts into 100mm diameter by 200mm height cylindrical polymer moulds. Each lift was then rodded 20 times and vibrated for three seconds for each lift. The top surface of every specimen was trowelled smooth.

Filled moulds were stacked onto a wooden pallet near the concrete mixing lab. Once all moulds were filled, the pallet could be carefully moved to a location where it would not be disturbed for the duration of the setting time. The pallet along with the concrete-filled moulds were covered with a polymer sheet weighed down with clay bricks as shown in Figure 18 in order to avoid plastic shrinkage cracks from developing on the surface of the freshly cast concrete blocks. The blocks were thus allowed to set overnight (roughly 18 hours).



Figure 18: Filled concrete block moulds covered by a polymer sheet

2.3.5 Unmolding and curing

Following roughly 18 hours of setting time, the blocks were carefully unmoulded. The four sides of the mould were removed by loosening and removing the threaded rods connecting the mould sides and gently striking the mould segments with a rubber mallet. The block was then pulled free from the base and overturned in order to expose the slender end of the mould segments forming the hollow cores of the blocks; those segments were then pushed through from the top, thereby freeing the block.

Blocks freed from their respective moulds were marked with a letter indicating the specific mould from which it was produced, the date of casting and two letters specifying the type of concrete mix (which was consistent throughout testing). For example, the SRCMU shown in Figure 19 was cast in mould “E” on July 8th, 2014; the concrete mix used (which incorporated fly ash) is denoted by “FA” on all the blocks.

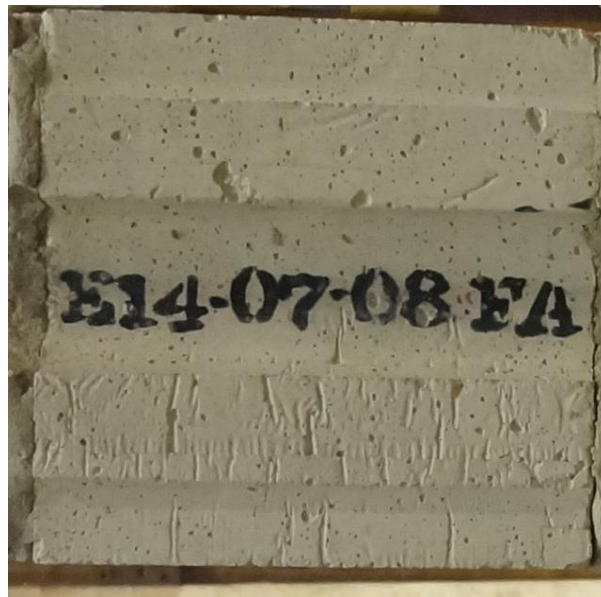


Figure 19: SRCMU sample date stamp

The blocks were then transferred to a curing chamber where they were moist-cured for 7 days at $21\text{ }^{\circ}\text{C}\pm 1$ and 100% humidity. Cured blocks were removed from the curing chamber and allowed to dry at the ambient temperature and humidity within the testing laboratory for a minimum of 7 days before use.

3 Chapter 3 – Experimental Phase 2: Material Testing and Block Validation

The behaviour of individual concrete blocks, and simple masonry assemblies under conditions of axial compression is discussed in this chapter. These experimental procedures were performed in order to determine whether or not the CMUs produced in laboratory in Chapter 2 displayed behaviour comparable to that of commercially-produced CMUs. Further characterization of the concrete used to produce the CMUs in laboratory was performed through the axial testing of standard cylindrical concrete samples. Testing of reinforced SRCMU assemblies will be discussed in Chapter 4.

The concrete blocks produced in Chapter 2 displayed physical dissimilarity when compared to commercially-produced blocks. Most importantly, the finish and surface texture of the blocks produced in laboratory appeared to be significantly smoother than that of commercially-produced CMUs as shown in Figure 20. The properties of the surfaces of CMUs undoubtedly play an important role in the interaction between CMUs and mortar within masonry assemblies, however only the macroscopic behaviour of the masonry assembly is material to this study. The purpose of this chapter is to demonstrate whether or not the concrete blocks produced in Chapter 2 accurately simulate the behaviour of commercially-produced CMUs in axial compression. Flexural tension behaviour was deemed to be outside the scope of this study since, although marked differences in behaviour likely existed between commercially-produced CMUs and the blocks cast in laboratory, this difference in behaviour was assumed not to affect the overall failure mechanism for the specimen configurations described in later chapters.



Figure 20: Laboratory-cast vs. commercial CMU surface texture

Tension tests performed on reinforcing materials used in Chapter 4 are also presented in this chapter.

3.1 Preparation of axial compression specimens

Two types of masonry specimens are discussed in this chapter; individual CMUs, and masonry prisms. Individual masonry blocks were tested without any surface preparation, as produced. Masonry prisms consisted of four CMUs stacked one on top of the other, each separated by a 10mm mortar joint over the entire surface of the blocks, including the web. Additionally, concrete test cylinders prepared from the same concrete as that used to produce the lab-cast CMUs are prepared for testing in this section

3.1.1 Casting of masonry prisms

All masonry prisms were assembled by professional masons. CSA Type S mortar was prepared by the masons with Type S masonry cement and loose sand following a 1:3 volumetric ratio, as prescribed by CSA A179. The amount of mixing water varied throughout the casting as it was adjusted by the masons to achieve the desired workability.

3.1.2 Curing of masonry prisms

Immediately after casting, all masonry prisms were covered with a polymer sheet, weighed down along its edges with concrete blocks to limit air exchange. Buckets filled with warm water were then placed under the polymer sheet along with the prisms in order to maintain high levels of humidity during the curing period. Masonry prisms were allowed to cure for 14 days under the polymer sheet as per CSA S304.1 Annex D. After 14 days, the polymer sheet was removed and the prisms were allowed to dry for at least an additional 14 days prior to testing. The age of the blocks and prisms is indicated in Table 10; note that the age of the commercial CMUs (CCMU) could not be determined.

Table 10: Prism age at testing

Specimen number	Block type	Average block age (days)	Prism age (days)
1	LCCMU	68	38
2	LCCMU	66	38
3	LCCMU	63	40
4	CCMU	-	40
5	CCMU	-	40
6	CCMU	-	40
7	SRCMU	65	40
8	SRCMU	71	40
9	SRCMU	63	40
10	SRCMU	55	40
11	SRCMU	54	40

3.1.3 Instrumentation of masonry prisms

In order to measure strain in the masonry specimens during loading, each masonry prism was fitted with six pi-gauges. Each pi-gauge was set on two mounts located 200mm apart at the locations indicated in Figure 21 and Figure 23; the gauges were located as close as practical to the centre line of the prism, above the central web. The difference between the location of the mounts for the conventional shaped blocks and the SRCMUs is due to the presence of the central

channel in the SRCMU blocks. An example of a commercial CCMU prism fitted with pi-gauges is shown in Figure 22.

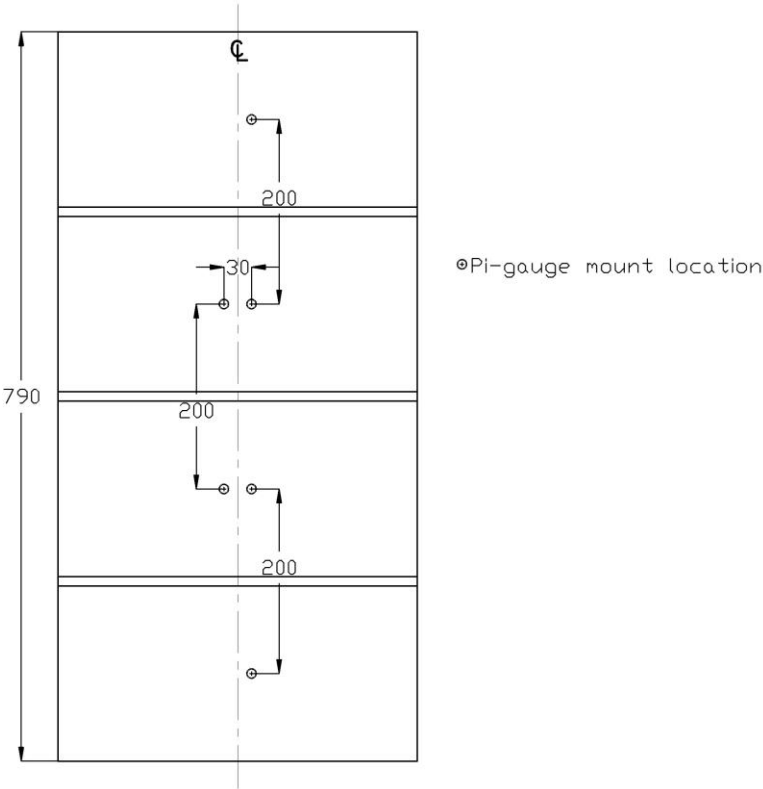


Figure 21: Location of pi-gauges; conventional shaped blocks, front and back



Figure 22: Conventional CMU prism fitted with pi-gauges

Prisms made from SRCMUs were also fitted with gauge points in order to facilitate readings of widening or contraction of the central channel of the SRCMU specimens. The locations of the points are indicated in Figure 23.

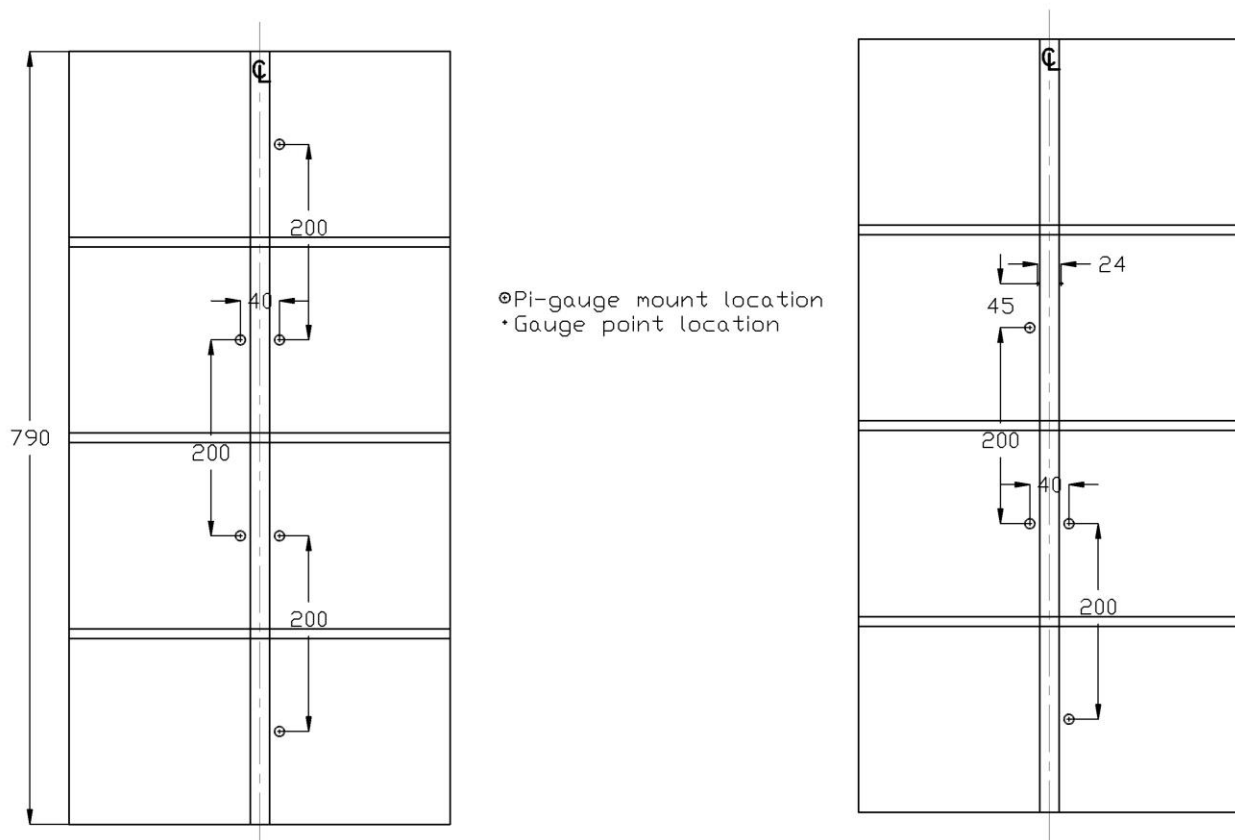


Figure 23: Location of pi-gauges and gauge points; SRCMUs, front (left) and back (right)

3.1.4 Preparation of concrete test cylinders

Concrete test cylinders were prepared by creating flat parallel-plane loading surfaces. This was achieved by bonding a sulphur-based capping material to both flat faces of each cylinder to be tested using the jig shown in Figure 24. Molten sulphur-based capping compound was poured into the base of the jig, the cylinder face to be capped was then gently lowered into the base of

the jig while maintaining contact between the concrete cylinder sides and the alignment arms of the capping jig. The cylinder was then held in place until the sulphur cap cooled and hardened sufficiently to hold its shape (roughly 30 seconds).



Figure 24: Cylinder capping jig

3.2 Axial testing of concrete and masonry specimens

The procedures employed to test the masonry prisms constructed as described in section 3.1, as well as a sampling of conventional-shaped, laboratory-produced CMUs and concrete test cylinders is described herein. For the testing of masonry prisms, ultimate load, and axial stress-strain behaviour were recorded. For SRCMU prisms, the widening/contraction of the reinforcement channels were also tracked. For the testing of CMUs and test cylinders, only the ultimate load was recorded.

3.2.1 Prism test set-up

Un-bonded capping was used for this test because of its ease of use. The material used was fibreboard as recommended by CSA S304.1 – Annex D; 1220mmX2440mm (4'X8') sheets of

fibreboard were cut into 210mmX410mm pieces for use as capping. Each specimen was centred on a piece of fibreboard and centred in the loading frame as shown in Figure 25. Another piece of fibreboard was then centred on the top of the prism, under the loading head.



Figure 25: Masonry prism centered in loading frame

The prisms were loaded using a Baldwin load frame with a maximum load of 2679kN and a maximum stroke of 300mm. The loading rate was controlled manually. The rate of displacement of the top cross-head was adjusted throughout the test to maintain a constant loading rate of 200kN/minute. This allowed for the final 50% of the ultimate load of the prism to be applied uniformly over approximately two minutes. A Data Acquisition system (DAQ) recorded total load, as well as the strain data from the six pi-gauges at a rate of 4Hz during testing.

Once 75% of the expected failure load was achieved, the load was paused in order to allow the instruments to be safely removed from the prisms before failure occurred. For the SRCMU specimens, the load was paused at intervals of 200 kN in order to allow for the

measurement of any displacement of the gauge points associated with widening or contraction of the central reinforcement channel.

The elastic modulus of a prism was determined for each pi-gauge by calculating the secant modulus between the stress levels of 0.05 and 0.33 of the mean prism compressive strength, as recommended by S304.1 Annex D.4.6.

3.2.2 CMU test set-up

Axial testing of CMUs was performed similarly to the testing of masonry prisms in axial compression. Fibreboard was used top and bottom for each CMU. The load frame and DAQ were the same as was used for the testing of prisms, however only readings from the load cell were recorded during testing. Again, the loading rate was controlled manually so that the final 50% of the ultimate load of the masonry block was applied over the course of approximately two minutes (200kN/minute). To expedite testing, the first 400kN of load was applied at a rate of 400kN/minute for each specimen.

3.2.3 Concrete cylinder testing

Axial testing of concrete test cylinders was done according to ASTM C39. The displacement rate of the loading platens of the cylinder testing machine was set in order to load the cylinder at a rate of 0.225 ± 0.005 MPa/s. No adjustment was made to the displacement rate of the loading platens after stress in each specimen reached 15MPa. The concrete cylinder testing machine is shown in Figure 26.



Figure 26: Concrete cylinder testing machine

3.3 Experimental results of axial compression tests

Here are discussed the results from axial loading tests performed on a range of masonry blocks and prisms as well as concrete test cylinders. These results indicate that blocks cast in laboratory behaved in a manner similar to commercially-produced CMUs.

3.3.1 Masonry prisms

Three behavioural traits were observed during testing of masonry prism specimens; elastic modulus, ultimate stress, and modes of failure. Note that in this section, prism specimens made from different types of CMUs are referred to by their constituent block type as indicated in Table 11.

Table 11: CMU type acronym

Acronym	Block type
SRCMU	Surface Reinforced Concrete Masonry Unit
LCCMU	Laboratory-Cast Concrete Masonry Unit (conventional shape)
CCMU	Commercially produced Concrete Masonry Unit

3.3.1.1 Elastic modulus

The elastic modulus as measured from each pi-gauge was averaged for each prism tested. This average data is presented in Figure 27 for all masonry prisms tested. Note that the modulus of elasticity was not recorded for specimens 1 and 7 because the failure load and mode of failure were unknown, and damage to the testing equipment could have resulted from premature specimen failure.

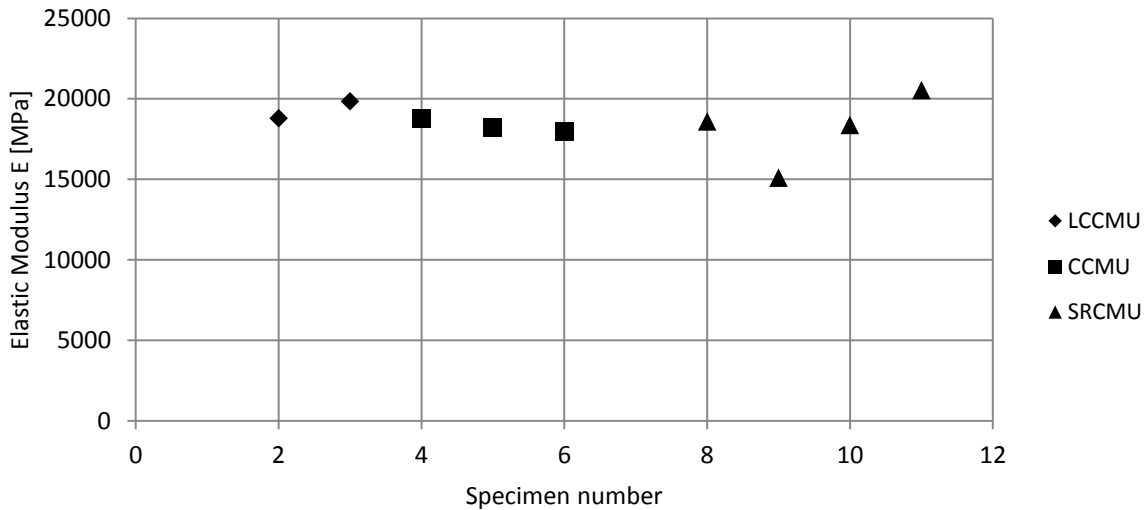


Figure 27: Compressive masonry prisms, elastic modulus E

Table 12 lists some statistical information about the modulus of elasticity of the prism specimens tested. Here it may be noted that the average modulus of elasticity of the SRCMU prisms and LCCMU prisms vary by less than 6% from the CCMU prisms. This information does

not indicated any statistically significant difference in modulus of elasticity between laboratory-cast CMUs and commercial CMUs, or between SRCMUs and conventionally shaped CMUs.

Table 12: Compressive masonry prisms, elastic modulus E

Average Modulus of Elasticity	
CCMU	19,310 MPa
LCCMU	18,310 MPa
SRCMU	18,150 MPa
Global statistical characteristics	
Average Modulus of Elasticity	18,460 MPa
Standard deviation	1,414 MPa
Coefficient of variation	.077

3.3.1.2 Ultimate load

The ultimate strength of each prism specimen was calculated by dividing the maximum load sustained by each specimen prior to failure by the minimum cross-sectional area of the type of block being used. The ultimate strength of each specimen is shown in Figure 28.

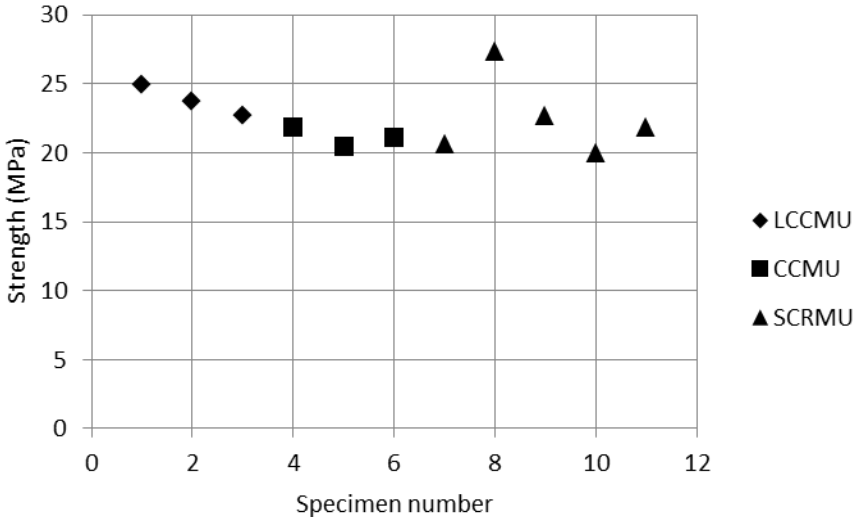


Figure 28: Compressive masonry prisms, ultimate strength

Statistical information on the compressive strength of prisms tested in this phase are displayed in Table 13. Little variation is observed between the average strength of the three prism populations tested and most importantly, the global coefficient of variation, at 0.093, is within the acceptable 0.15 outlined by S304.1 Annex D for a minimum prism sample size of 5.

Table 13: Compressive masonry prisms, ultimate strength

Average Strength	
CCMU	21.1 MPa
LCCMU	23.8 MPa
SRCMU	22.5 MPa
Global statistical characteristics	
Average Strength	22.5 MPa
Standard deviation	2.1 MPa
Coefficient of variation	.093

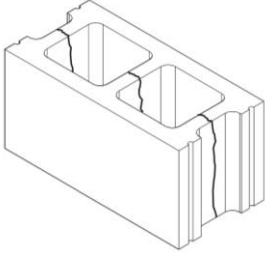
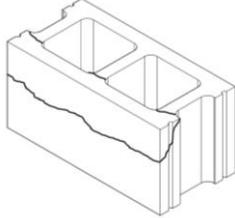
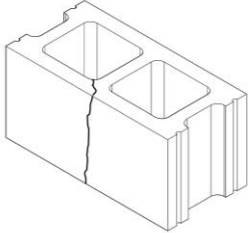
3.3.1.3 Channel expansion

The expansion and/or contraction of the SRCMU reinforcement channel was in all cases less than the lowest limit of the measuring instrumentation. Subsequent studies should make use of more sensitive instrumentation.

3.3.1.4 Modes of failure

The over-all mode of failure for all prism specimens consisted of splitting through the webs of the blocks, in combination with other local failures. A description of the types of failure observed along with diagrammatic and photographic representations are shown in Table 14.

Table 14: Axial compression prisms modes of failure

Mode of failure	Description	Diagram	Photograph
Web splitting	Vertical cracking through all three webs of a CMU. These cracks initiate near the centre of the prism specimens and propagate vertically upwards and downwards through mortar joints and into adjacent concrete blocks.		
Face-shell spalling	Diagonal cracking of a face shell propagating from a mortar joint, diagonally through a CMU face shell toward the surface.		
Face-shell splitting	Vertical cracks through the face shell of CMUs near the location of the central web.		

3.3.2 Masonry Units

To further characterize the behaviour of the laboratory-cast CMUs, a sampling of single masonry blocks were tested in axial compression. The main purpose of this section is to show whether or not uniform compressive properties were achieved between various days of casting. Note that individual blocks were tested at a much later age than the prisms due to scheduling issues in the laboratory. Although little change in strength is expected to have occurred between the time of the testing of prisms and individual blocks (due to the use of HE cement, which gains the majority of its strength over the first 14 days of curing), no correlation between the two will be attempted here.

3.3.2.1 Ultimate load

A sampling of LCCMUs was tested following the procedure outlined in section 3.2.2. The average ultimate strength of concrete blocks cast on select dates, as well as their age at the time of testing is indicated for each concrete batch in Table 15. The global average block strength is 23.7 MPa with a standard deviation of 1.88 (coefficient of variation=7.9%).

Table 15: Axial testing of LCCMU concrete blocks

Casting date [yyyy-mm-dd]	Block age at testing [days]	Number of blocks tested	Average block strength [MPa]
2014-07-02	145	2	24.6
2014-07-03	144	1	24.5
2014-07-04	143	1	24.6
2014-07-07	140	2	24.3
2014-07-08	139	1	21.8
2014-07-09	138	3	22.5
2014-07-10	137	3	25.5
2014-07-11	136	3	22.5

3.3.2.2 Modes of failure

All blocks tested failed following a similar mode. Vertical and diagonal splitting fracture of the face shells and webs occurred suddenly at the failure load. A diagrammatic drawing of the mode of failure of the specimens alongside an annotated photograph of a typical failed specimen is shown in Figure 29.

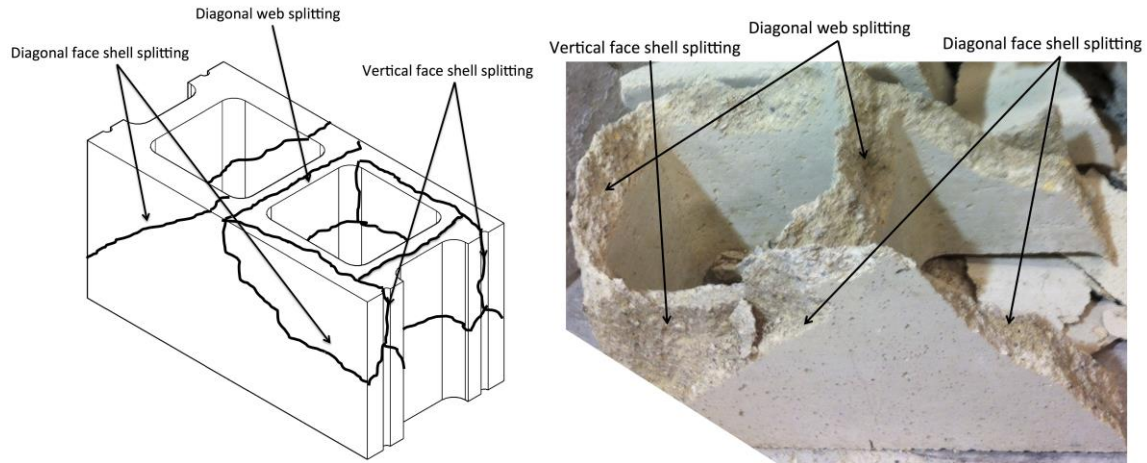


Figure 29: CMU mode of failure

3.3.3 Concrete test cylinders

Concrete cylinders made from the same batches of concrete as used to cast the concrete blocks tested in 3.3.2 were tested in compression following the procedure outlined in section 3.2.3. The number of cylinder specimens tested for each batch of concrete tested is shown with the average cylinder strength for that batch in Table 16. The global average strength of the cylinders aged more than 28 days is 32.7 MPa with a standard deviation of 2.28 (coefficient of variation=7.0%).

Table 16: Axial testing of concrete cylinder samples

Casting date [yyyy-mm-dd]	Cylinder age at testing [days]	Number of cylinders tested	Average cylinder strength [MPa]	Standard deviation [MPa]
2014-06-10	14	4	25.5	-
2014-06-10	162	3	36.5	-
2014-06-12	160	8	33.7	1.28
2014-07-09	139	3	31.6	-
2014-07-10	138	7	30.1	1.19
2014-07-11	137	8	33.1	1.57

3.4 Preparation of tensile specimens

In this section, reinforcing bars are tested in order to determine their tensile stress-strain relationship. The relationships developed herein are used in Chapter 4 to characterize the stress distribution within the reinforcing bars of reinforced SRCMU specimens. Both conventional steel reinforcing bars and GFRP bars are tested in this section.

3.4.1 Steel reinforcing bar specimens

Three sample pieces of 10M 400W reinforcing steel from the same stock used in Chapter 4 were cut into pieces 600mm long. This length was selected to conform to ASTM A370 Annex 9 for the available loading frame; it exceeds the sum of gauge length (200mm), twice 2 bar diameters (40mm total) between the gauge marks and load frame grips, and twice the length of the load frame grips (200mm total). Each piece was fitted with an electrical strain gauge at mid length following the procedure outlined in section 3.4.1.1.

3.4.1.1 Installation of electronic strain gauges on reinforcing bars

Surface Preparation:

A belt sander is used to smooth the surface to which the strain gauge is to be fixed; bar deformations and sand coating are removed from steel bars and GFRP bars respectively on one side of the reinforcing bar, being careful not to reduce the effective cross-sectional area of the bar, as shown in Figure 30. The cylindrical shape of the bar is maintained. The smoothed area roughly 5mmX10mm is thoroughly cleaned and degreased with ethanol; lint-free wipes dipped in ethanol are used to wipe the surface until no visible contaminants are removed with subsequent wipes. For steel bars only, the prepared surface is then wiped once with steel conditioner and once with neutralizer.



Figure 30: Steel rebar - prepared surface for strain gauge installation

Strain gauge preparation:

A sheet of lexan is carefully cleaned by wiping it with ethanol until no additional visible contaminants may be removed. A strain gauge is carefully removed from its protective jacket and the lead wires are carefully splayed to avoid any risk of short circuit as shown in Figure 31. The gauge is then taped down onto the lexan sheet using adhesive polymer tape being careful to ensure the gauge wires are positioned against the adhesive tape. The adhesive tape and gauge (now affixed to the tape) are both lifted from the lexan sheet and carefully placed on the bar so that the strain gauge is positioned lengthwise at the centre of the prepared surface, positioning it to measure longitudinal strains in the bar.

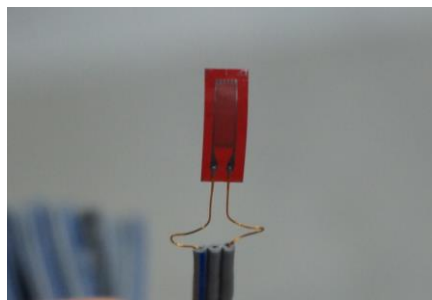


Figure 31: Prepared electronic strain gauge

Strain gauge gluing:

The lead wires of the strain gauge are carefully held in place with a finger so that a portion of the adhesive tape is also held in place on the reinforcing bar. The other end of the adhesive tape is then carefully lifted to expose the prepared surface of the reinforcing bar as well as the underside of the strain gauge. One stroke of glue conditioner is spread onto the underside of the strain gauge. A drop of glue is placed at the base of the strain gauge at the location of the lead wires; this location should also conform to the location where the lifted adhesive meets the prepared surface of the reinforcing bar. Continuing to hold the end of the adhesive tape and lead wires with one finger, the strain gauge is pressed into place by carefully pressing the adhesive tape to expel excess glue and cover the full underside of the strain gauge where it is in contact with the prepared surface. The gauge is held in place with a finger for 60seconds until the glue has fully hardened.

Strain gauge covering/protection:

The adhesive tape used to hold the gauge in place is carefully removed. The exposed surface of the strain gauge is then coated with nitrol rubber. After 2 minutes of setting, a piece of Teflon tape slightly larger than the strain gauge is placed on the nitrol rubber coating. The nitrol rubber is allowed to cure for 15 minutes. Finally, the strain gauge and lead wires are covered with a 2mm coat of 2-part epoxy, which is sprinkled with fine sand for a completed installation as shown in Figure 32.



Figure 32: Strain gauge - installation complete

3.4.2 GFRP reinforcing bar specimens

Three samples pieces of #3 (9.5mm diameter) sand-coated GFRP bars were cut to a length of 1030mm. This length was selected to conform to ASTM D7205; it exceeds the sum of gauge length (380mm), and twice the minimum anchoring length (300mm). Each bar specimen was then anchored on both ends into 300mm lengths of Drawn on Mandrel (DOM) steel tubing with an inside diameter of 20mm and a wall thickness of 5mm. The anchoring procedure is outlined in Section 3.4.2.1. Bars anchored on both ends into DOM steel tubes, were then fitted with an electronic strain gauge following the procedure outlined in Section 3.4.1.1.

3.4.2.1 Installation of DOM anchors onto GFRP bar ends

DOM tube preparation:

A continuous piece of DOM tube is cut to a length of 300mm using a metal band saw. Rough edges around the cut surfaces of the tube are ground using a bench grinder to prevent injury during handling of the tube. The inner surface of the tube is brushed with a rotary metal brush, then thoroughly cleaned and degreased. An alignment cap is welded to one end of the tube.

Restraining of DOM and GFRP:

An alignment jig is secured in a vertically aligned position. Prepared lengths of DOM tube are secured into place at the bottom of the jig. The piece of GFRP bar to be anchored is secured into position by threading the bar through the tube and ensuring that the bar protrudes through the alignment cap at the bottom of the tube, and securing the upper portion of the bar to the jig such that the upper portion of the bar is centered with respect to the opening at the top end of the DOM tube. The joints between the GFRP bar and the alignment cap as well as the joint between the alignment cap and DOM tube are sealed with hot glue.

Expansive grout preparation and casting:

Expansive cement grout is prepared according to the manufacturer's instructions using a water to binder ratio of 0.3 by weight, and thoroughly mixed using a drill with a paddle mixer attachment for 60 seconds. The prepared cement grout is then carefully poured into the top end of the DOM tube filling the space around the GFRP bar in three lifts. Between each lift, the grout is vibrated by gently striking the DOM tube with a mallet ten times to evacuate any entrapped air within the grout. The grout is then allowed to cure overnight before the anchored bar is released from the jig.

3.5 Tension test procedure

Both steel and GFRP specimens were tested using the same load frame and DAQ. The load frame was the Instron Universal Testing Machine shown in Figure 33; the DAQ recorded the total load, and strain readings from the electronic strain gauge at a rate of 2Hz. Load data could then be converted to bar stress by dividing them by the bar's cross-sectional area (100mm^2 for the steel bars, 71.3mm^2 for the GFRP bars). The first steel bar was loaded under displacement control at a rate of 0.5mm/minute , for a total test duration until rupture of 12 minutes and 15

seconds; in the interest of time, the load rate was accelerated for the remaining two steel specimens to a rate of 2mm/minute for a total test duration until rupture of roughly 3 minutes. Both testing speeds are acceptable based of ASTM A370, which sets only a maximum loading rate of 0.0625mm/minute per mm length between grips, corresponding to approximately 15mm/minute for this test set-up.



Figure 33: Instron universal testing machine

The first GFRP specimen was tested under displacement control at a rate of 0.66mm/minute for a total test duration until rupture of 10 minutes and 27 seconds; in the interest of time, the load rate was accelerated for the remaining two GFRP specimens to a rate of 1.2mm/minute for a total test duration of roughly 5 minutes. ASTM D7205 dictates testing speeds for GFRP bars, allowing for total test durations between 1 and 10 minutes. The first bar

test duration only slightly exceeded that recommended, and was therefore accepted for the purposes of this study.

3.6 Experimental results of reinforcing bar testing

Figure 34 shows the strain data for all three steel test specimens plotted against the calculated stress, based on the load data and the effective cross sectional area of the steel bars. Note that the strain gauge readings became erroneous from approximately 36000microstrain. Also plotted on Figure 34 is the best fit model for the behaviour of the steel constructed in the following way;

The slope of the elastic portion of the stress-strain diagram was determined by taking the average of the slope of the elastic portion of the three bars tested. The elastic slope was determined for each specimen using the least squares method from zero load to $0.9f_y$ for that bar. f_y was determined for each specimen by taking the average stress reading in the middle third of the yield plateau. The end of the yield plateau was determined by taking the average of maximum strain readings before significant gain in stress is observed at the end of the yield plateau. The strain hardening portion was constructed by fitting a fourth order polynomial to the data from the three specimens. The maximum strength was determined by taking the average of the maximum load recorded for each of the steel bars tested. Note that the strain gauges did not capture the strain at maximum stress for any of the bars. An extensometer allowed the estimation of the average bar strain at maximum stress levels.

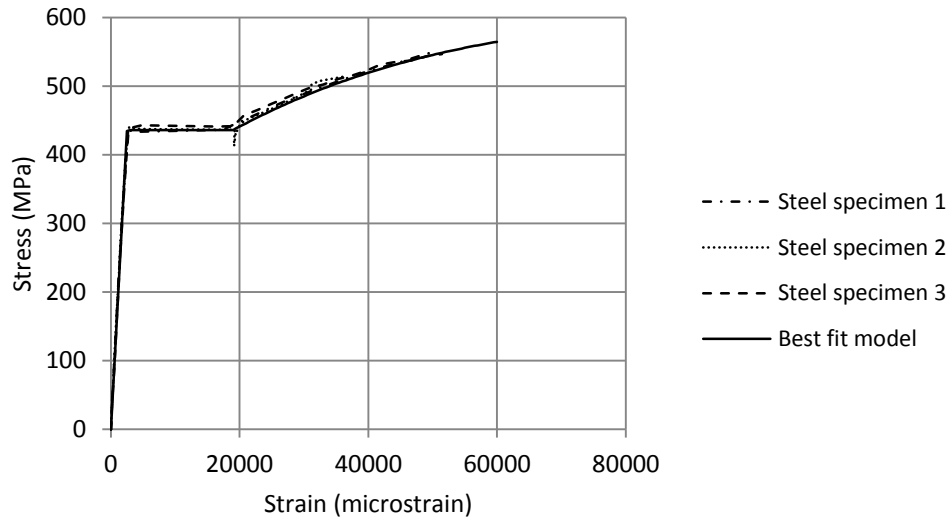


Figure 34: Stress-strain plot, steel reinforcing bar specimens

The average properties indicated in Table 17 are therefore assigned to the steel reinforcing bar material for the remainder of this document.

Table 17: Steel rebar material properties

Property	Value
Modulus of Elasticity, E (MPa)	173.7×10^3
Yield stress, f_y (MPa)	436.0
Strain hardening curve (MPa)	$-5.93 \times 10^{-19} (\epsilon - 148000)^4 + 612.2$
Maximum stress (MPa)	612.2
Strain at end of yield plateau (microstrain)	19035
Strain at maximum stress (microstrain)	148000

The stress-strain data collected from the testing of GFRP bar specimens are displayed in Figure 35. Also displayed in Figure 35 is the best fit linear elastic curve to the data from all three specimens. The slope of the best fit curve was determined by taking the average of the best fit slope for each specimen between zero and 95% of the maximum stress developed in that specimen using the least squares method. The maximum stress for the best fit curve was

determined by taking the average of the maximum stress recorded for each of the three GFRP bar specimens.

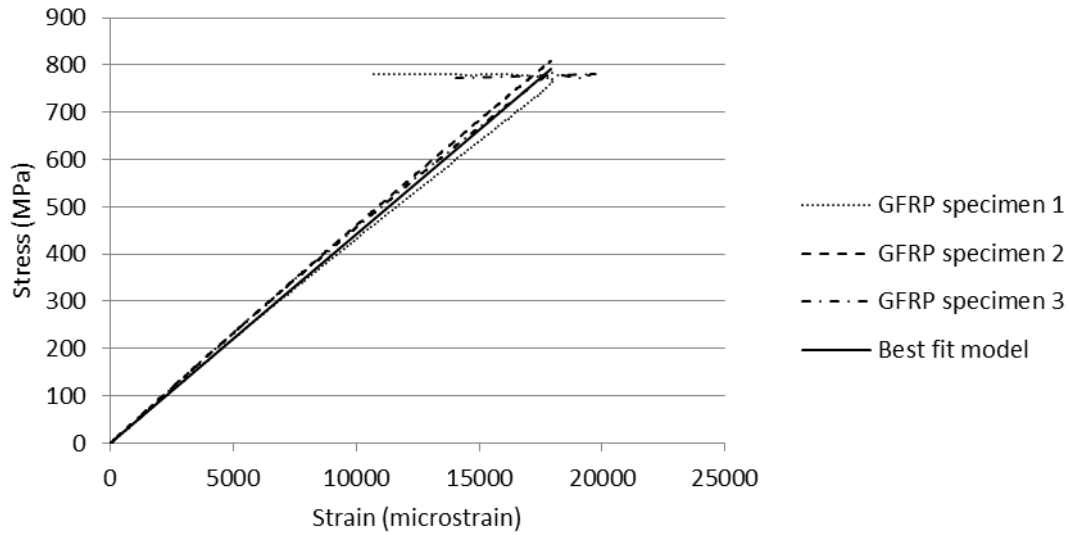


Figure 35: Stress-strain plot, GFRP reinforcing bar specimens

The average properties indicated in Table 18 are therefore assigned to the GFRP reinforcing bar material for the remainder of this document.

Table 18: GFRP reinforcing bar material properties

Property	Value
Modulus of Elasticity, E (MPa)	44.1×10^3
Maximum stress (MPa)	791.4

3.7 Discussion

The purpose of this chapter was to analyse the properties of the materials used in this experimental study. Discussed herein are the behaviour of simple masonry assemblies (masonry prisms) under unconfined axial compressive stress, samples of the concrete (cylinders and

blocks) from which SRCMU blocks were made under unconfined axial compressive stress, and samples of the reinforcing bars (both steel and GFRP) under axial tensile stress.

3.7.1 Masonry prisms

The masonry prism tests had two main objectives: to contrast the behaviour of masonry assemblies made from commercially produced CMUs to those made from CMUs of the same shape, but cast in the laboratory, and to determine the effect of the SRCMU shape on the axial compressive behaviour of masonry prisms when compared to those made from conventionally shaped CMUs.

The small population of test specimens does not allow for a strong statistical analysis. However, given that all three populations of prisms exhibited the same modes of failure and similar failure loads and elastic moduli, it may be stated that there is no strong evidence to suggest significant difference in axial compressive behaviour between SRCMUs and conventionally shaped CMUs.

3.7.2 Concrete blocks and test cylinders

Concrete blocks and test cylinders showed similar variability of strength properties. In both cases, the coefficient of variation of the entire population of specimens was approximately twice as large as the coefficient of variation of specimens cast on the same day. The coefficient of variation for the block strength as well as that of the test cylinders was under 10%, indicating consistency in results.

Comparing the average strength of concrete blocks to that of test cylinders, it may be observed that concrete blocks have on average 72.4% the strength of concrete cylinders made from the same concrete. Comparing data for concrete produced on July 9th, 10th, and 11th 2015, CMUs were recorded as having 71.2%, 84.7%, and 68.0% the strength of concrete test cylinders

cast on the same day, respectively. The lower strength of concrete blocks when compared to concrete cylinders is expected because of the size factor and shape factor; concrete blocks are both larger in volume than concrete test cylinders and the walls of CMUs are much more slender. Larger concrete specimens have a greater chance of having local discontinuities that could result in premature failure; slender specimens are known to exhibit lower strength due to decreased confinement from bulk concrete.

3.7.3 Reinforcing bars

The results from the testing of reinforcing bars agreed well with expected results from the manufacturers. The steel reinforcing bar stock had a nominal elastic modulus of 200 GPa and a nominal yield strength of 400MPa. The test results showed an average elastic modulus of 173.7GPa (13.5% lower than nominal) and a yield strength of 436.0MPa (9% higher than nominal). The GFRP bars had a designated elastic modulus of 42.5 MPa and minimum rupture strength of 880MPa. Test results showed an average elastic modulus of 44.1 MPa (3.7% higher) and rupture strength of 791.4 MPa (10% lower). The lower observed strength of the GFRP bars is likely due to the slight reduction in cross-sectional area and asymmetry caused by surface preparation for the mounting of strain gauges.

4 Experimental Phase 3: Testing of Reinforced SRCMU Assemblies

The masonry units produced following the procedures described in Chapter 2, were shown to behave similarly to commercially-produced CMUs in Chapter 3. Furthermore, no significant difference was observed between the axial compressive behaviour of unreinforced conventionally shaped CMU assemblies and unreinforced SRCMU assemblies.

The experimental procedures described in this chapter characterize the global behaviour of the reinforced SRCMU system for out-of-plane flexural loading conditions. In this section a 2-part epoxy anchoring adhesive was used to bond reinforcing bars into the reinforcement channels of SRCMU masonry specimens. This type of adhesive was selected because it is currently available on the market, and is designed to bond well with concrete. The use of both steel and FRP reinforcing bars were studied because although FRP bars are not yet commonly used in new masonry construction, their adoption is becoming more widespread in reinforced concrete construction; GFRP specifically was selected since it is the most commonly used type of FRP reinforcement. Two types of tests were performed in this phase; a pull-out test and a flexural test.

4.1 Pull-out testing

Pull-out test specimens consisted of 3-high masonry prisms in which a protruding reinforcing bar was grouted into one of the central face-shell surface channels. This set-up allowed the masonry prism to be restrained while tension was applied on the protruding reinforcing bar. This test was selected to characterize the bond between the epoxy and the reinforcing bars, and between the epoxy and the concrete.

4.1.1 Specimen fabrication

The first step in the fabrication of pull-out specimens was to construct the prisms into which the reinforcing bars would be mounted. Casting of prisms was performed by professional masons following the procedure outlined in Section 3.1.1. The prisms were allowed to cure under a polymer sheet at 100% relative humidity for 14 days, and then allowed to dry for 7 days prior to the installation of the reinforcing bars.

Steel reinforcing bars were cut to a length of 950mm to accommodate the height of the masonry specimen (590mm) in addition to 200mm free length and a 200mm allowance for the load frame to grip the reinforcing bar. Visible oxidation was removed from the steel bars by brushing them with a rotary steel brush. GFRP bars were cut to a length of 1105mm to allow for the height of the masonry specimen in addition to the 200mm of free length, 300 of anchored length and 15mm of protrusion from the anchor. Each GFRP bar was fitted on one end with a DOM steel tube anchor following the procedure outlined in Section 3.4.2.1. Six electronic strain gauges were installed on each bar following the procedure outlined in Section 3.4.1.1 at intervals of 100mm as indicated in Figure 36.

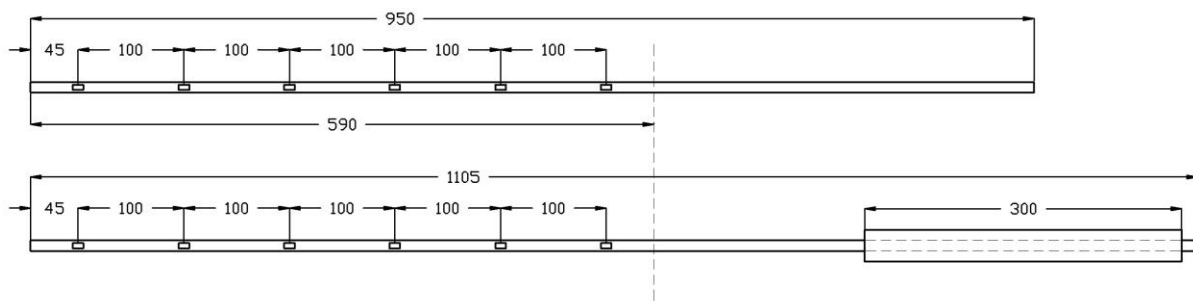


Figure 36: Strain gauge location: pull-out specimen steel (top) and GFRP (bottom) reinforcing bars

A plywood jig was used to centre the reinforcing bars in place during installation. Figure 37 shows the jig installed on a concrete block; by tying a bar against the jig at the central mark, it is held in vertical alignment concentrically with the semi-circular end of the reinforcement channel.



Figure 37: Pull-out bar installation

Each specimen was reinforced while standing in the upright position to simulate conditions during field applications as well as to avoid any unnecessary manipulation of the specimens. The reinforcement channel in which the reinforcing bar was to be installed was prepared according to the instructions provided by the manufacturers of the dowelling epoxy

used for the installation of reinforcing bars; the inner surfaces of the reinforcement channel was brushed with a stiff wire brush, then cleared of debris by blowing it out with compressed air (this procedure was repeated twice, as per manufacturer’s instructions). The surface of the face shell on either side of the reinforcement channel was lined with adhesive tape to protect the concrete from excess epoxy. The reinforcement jig was then installed on each specimen and held in place using “C” clamps. The reinforcement channel on the side to be reinforced was filled half-way with 2-part dowelling epoxy. A prepared reinforcing bar fitted with strain gauges was then fitted into place by tying it to the centring jig with wire. The reinforcement channel was then completely filled with the epoxy, which was then trowelled smooth. The adhesive tape was removed from the surface of the face shells before the epoxy began to harden. The epoxy was allowed to cure for at least 7 days prior to testing. Table 19 indicates the age of the blocks, prism, and epoxy at the time of testing for each of the pull-out specimens.

Table 19: Pull-out specimen age at time of testing

Specimen number	Reinforcing bar type	Average age of SRCMUs (days)	Age of prism (days)	Age of epoxy grout (days)
P1	Steel	169	35	19
P2	Steel	177	35	19
P3	Steel	189	35	19
P4	GFRP	184	35	19
P5	GFRP	178	35	19
P6	GFRP	187	35	19

4.1.2 Test procedure

Pull-out tests should ideally be performed with a concentric loading configuration to avoid the influence of additional bending stresses on the modes of failure. Such concentric loading configuration is difficult to achieve; De Lorenzis et al. (2002) designed a pull-out test for concentric loading of NSM reinforcement in a RC specimen, however for masonry tests, we are

constrained by the actual geometry of the specimen. The test procedure described herein follows that of Dizhur et al. (2014), for eccentrically loaded masonry samples with NSM reinforcement.

The test set-up was comprised of two main components; the load frame and the restraining jig. The load frame was an Instron universal testing machine. The restraining jig was constructed as shown in Figure 38. Four 76mmx76mmx13mm (3"x3"x1/2") steel angles were cut to a length of 476mm. Holes were drilled at the locations indicated to accommodate 19mm steel threaded rod. One of the angles was also notched at the middle of one leg to accommodate the protruding end of the reinforcing bars of the pull-out specimens. A notched 13mm steel plate was used to distribute the load from the restraining jig onto the top surface of the pull-out specimen. A sheet of fiberboard was placed both on the top and bottom surfaces of the pull-out specimens to avoid stress concentrations and premature failure.

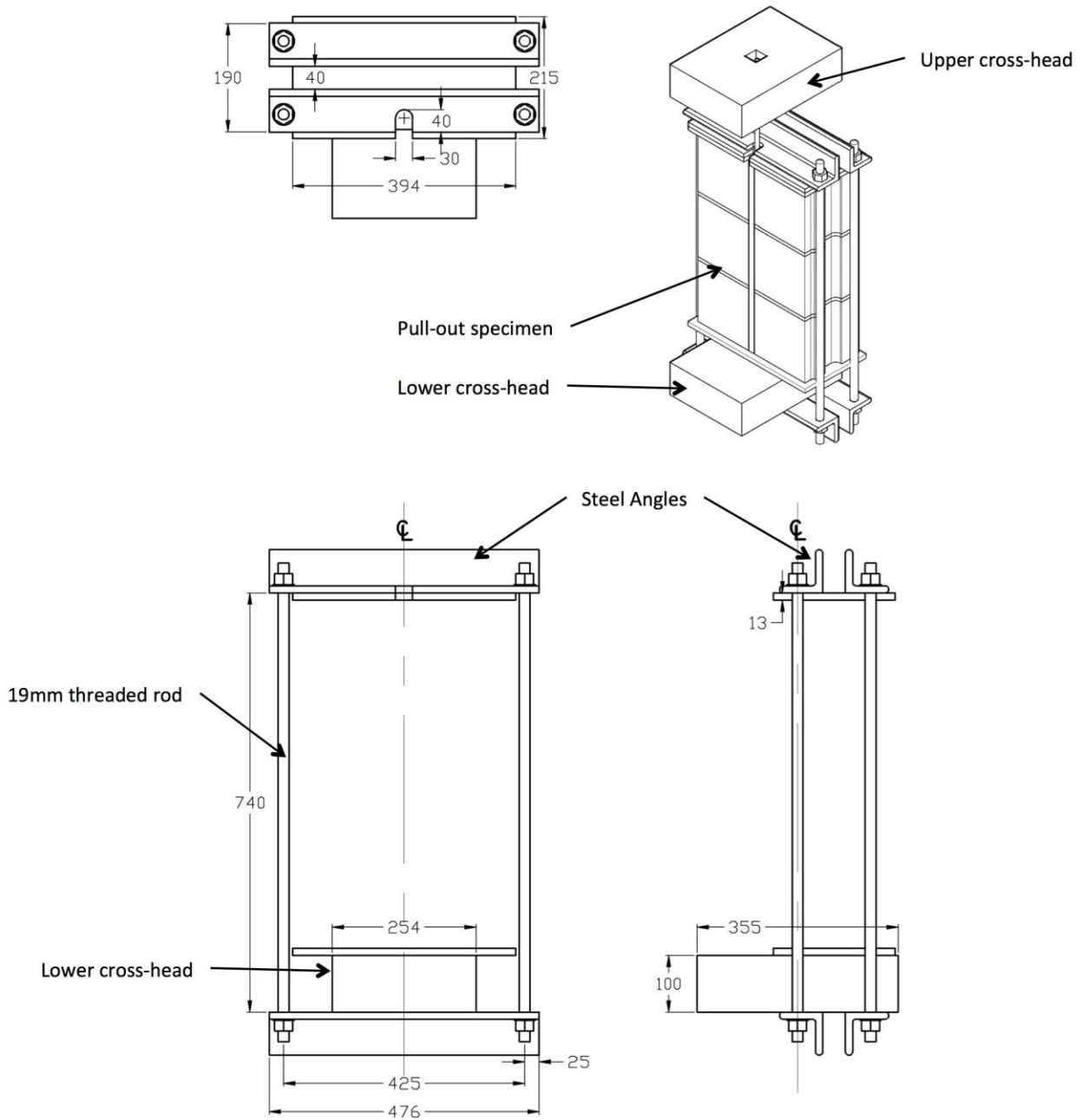


Figure 38: pull-out restraining jig

Each pull-out specimen was lifted into position using a hydraulic crane. The protruding end of the reinforcing bar was centered in the grips of the upper crosshead before the specimen was carefully secured to the lower cross-head of the load frame with the restraining jig. The

restraining jig was tightened against the lower cross-head of the load frame by sequentially tightening the nuts on threaded rod to finger tight plus one full turn.

Once the masonry portion of the specimen was secured onto the lower crosshead, and the protruding portion of the reinforcing bar secured in the grips of the upper crosshead, the electronic strain gauges and the load cell from the load frame were connected to the DAQ. The specimen was then loaded by lowering the lower crosshead under displacement control at a rate of 1.5mm/minute.

4.1.3 Results

At load levels approaching failure, hairline horizontal cracks could be observed in the epoxy grout, as well as diagonal “herring bone” cracks in the concrete, and vertical cracks along the interface between the epoxy and the concrete channel; these signs of deterioration are shown in Figure 39. Comparing the behaviour of the GFRP reinforced specimens to that of steel reinforced specimens, it may be noted that cracking in steel reinforced specimens was minimal prior to failure and localized to the area directly adjacent to the protruding reinforcing bar. In fact, no cracking was observed in the steel-reinforced specimens until the onset of strain hardening in the bar. Table 20 summarises the ultimate failure load and the mode of failure for each pull-out specimen. Two of the steel-reinforced specimens and one of the GFRP-reinforced specimens failed by rupture of the reinforcing bar; the remaining specimens failed by pull-out (mechanical separation of the bar and epoxy from the masonry assembly). The specimens that failed by pull-out did so in the concrete region, indicating a good bond between the epoxy and the masonry was achieved; cement paste and broken aggregate remained adhered to the bar-epoxy assembly extracted from the failed masonry specimen.

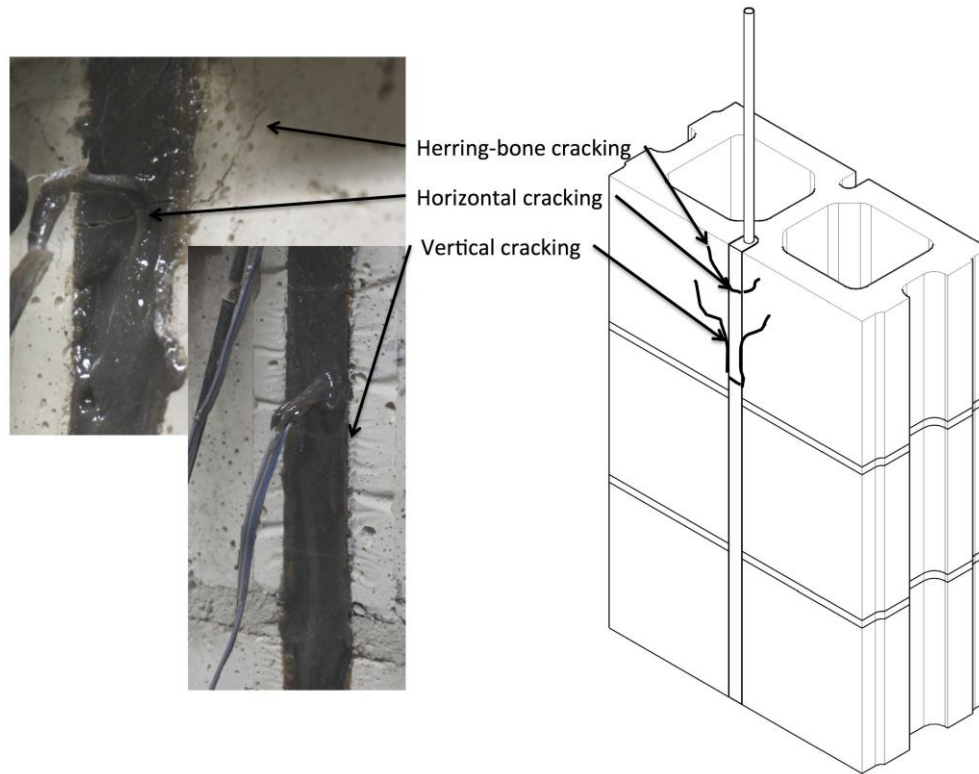


Figure 39: Pull-out specimen modes of deterioration

Table 20: Pull-out specimens maximum load and mode of failure

Specimen ID	Reinforcement material	Ultimate failure load (kN)	Mode of failure
P1	10M steel rebar	59.8	Bar rupture
P2	10M steel rebar	57.6	Bar pull-out
P3	10M steel rebar	59.5	Bar rupture
P4	#3 GFRP bar	52.6	Bar rupture
P5	#3 GFRP bar	47.3	Bar pull-out
P6	#3 GFRP bar	46.5	Bar pull-out

Data collected by the strain gauges installed on the reinforcing bars are displayed in Figure 40, Figure 41, Figure 42, and Figure 43; these figure show the variation in stress in the reinforcing bars in relation to distance from the loaded end at various load levels up to failure. Figure 40 and Figure 41 show bar stress distribution curves for specimens that failed through rupture of the reinforcing bars; Figure 42 and Figure 43 show bar stress distribution curves for specimens that failed through pull-out of the reinforcing bar and epoxy.

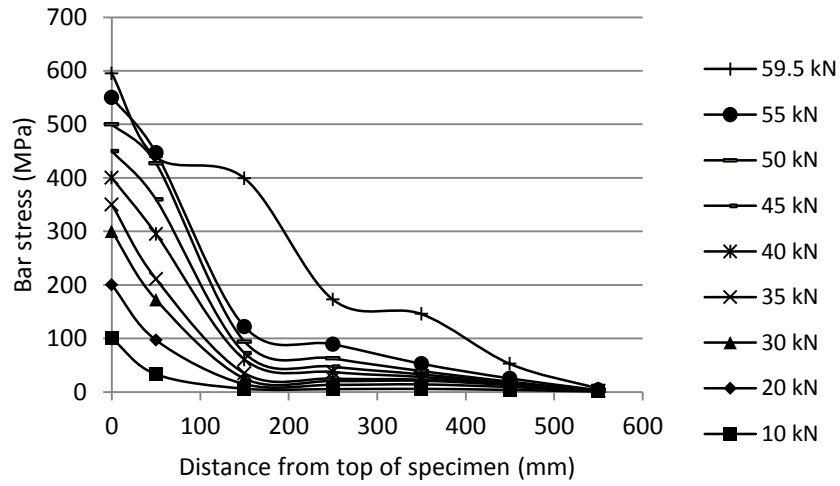


Figure 40: Bar stress distribution, specimen P3 (Steel reinforced)

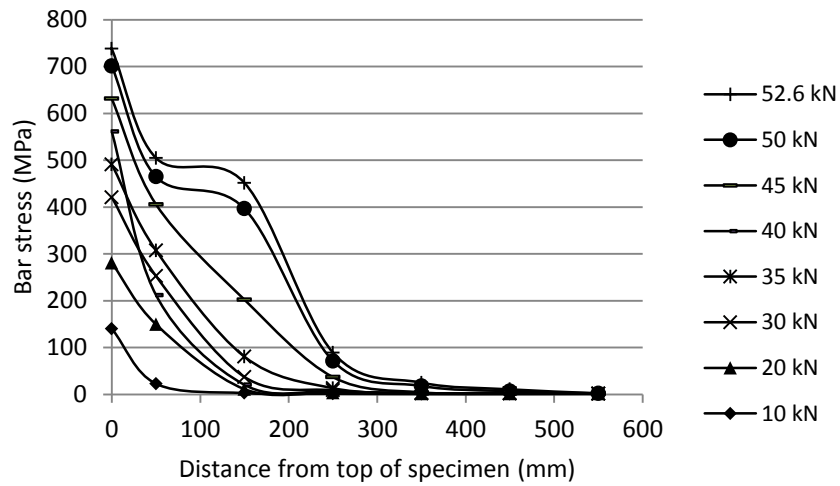


Figure 41: Bar stress distribution, specimen P4 (GFP-reinforced)

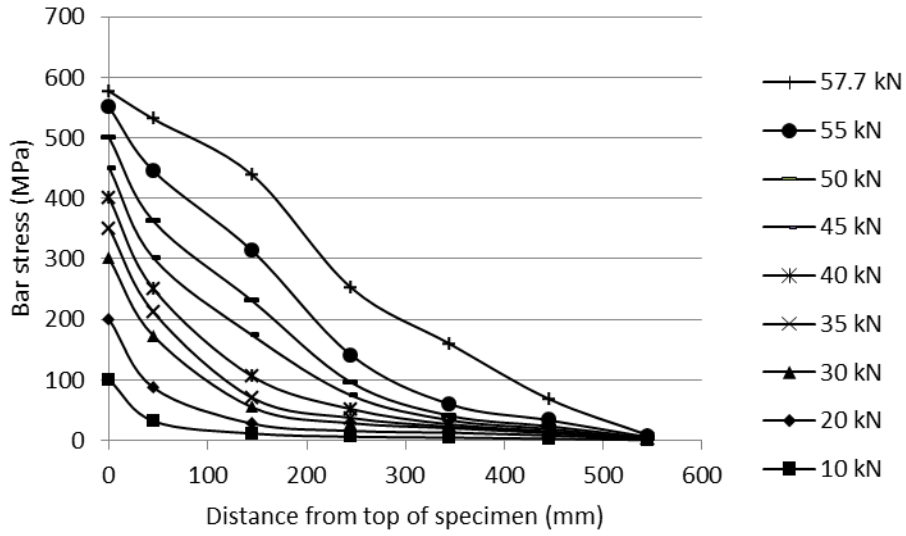


Figure 42: Bar stress distribution, specimen P2 (steel-reinforced)

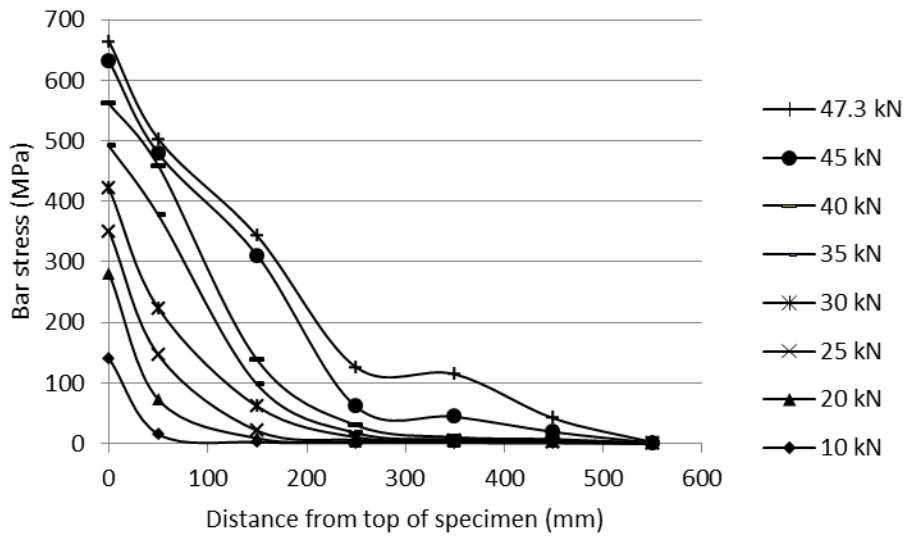


Figure 43: Bar stress distribution, specimen P5 (GFRP-reinforced)

From the bar stress distribution data, two additional parameters that may be used to characterize the relationship between bond shear stress and bond slip were calculated. Average local bond shear stress was calculated based on equation (31), adapted from Dizhur et al. (2013):

$$\tau = \frac{\Delta \varepsilon EA}{\Delta LC_b} \quad (31)$$

Where τ is the average local shear stress, $\Delta \varepsilon$ is the differential strain over the length ΔL between two adjacent strain gauges, E is the elastic modulus of the reinforcing bar, C_b is the circumference of the bar, and A is the cross-sectional area of the bar. The local bond shear stress distribution of specimens P3, P4, P2, and P5 are displayed in Figure 44, Figure 45, Figure 46, and Figure 47, respectively.

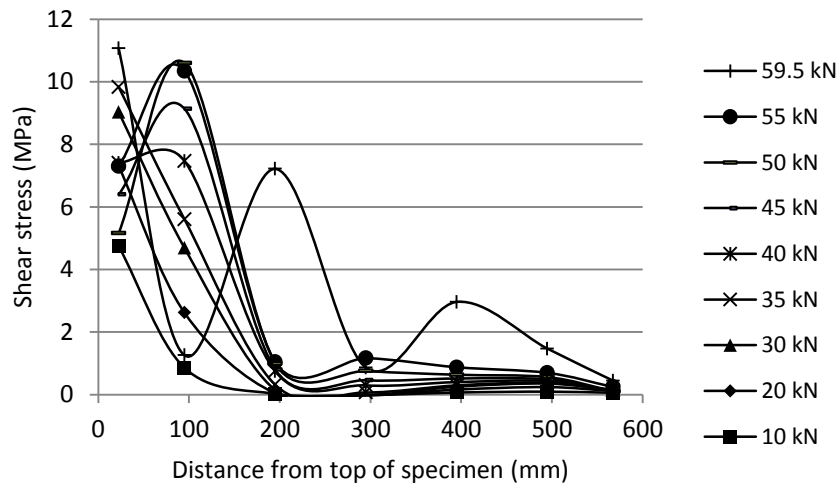


Figure 44: Bond shear stress distribution, specimen P3 (steel-reinforced)

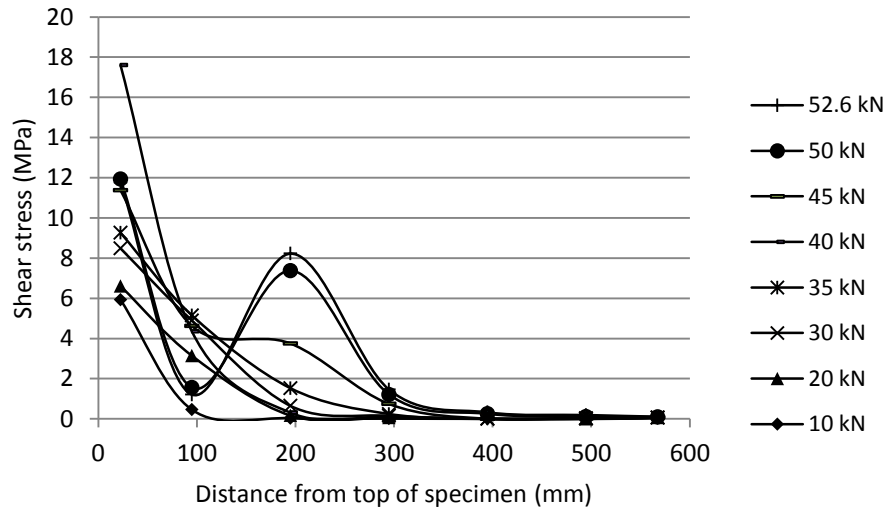


Figure 45: Bond shear stress distribution, specimen P4 (GFRP-reinforced)

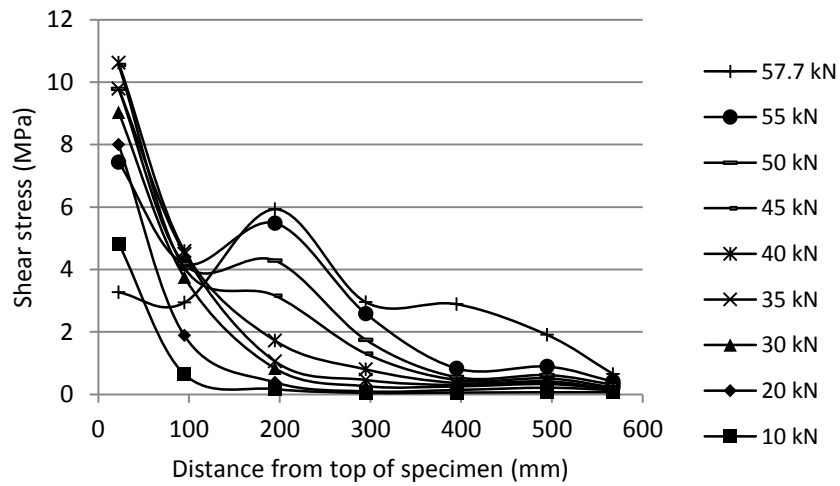


Figure 46: Bond shear stress distribution, specimen P2 (steel-reinforced)

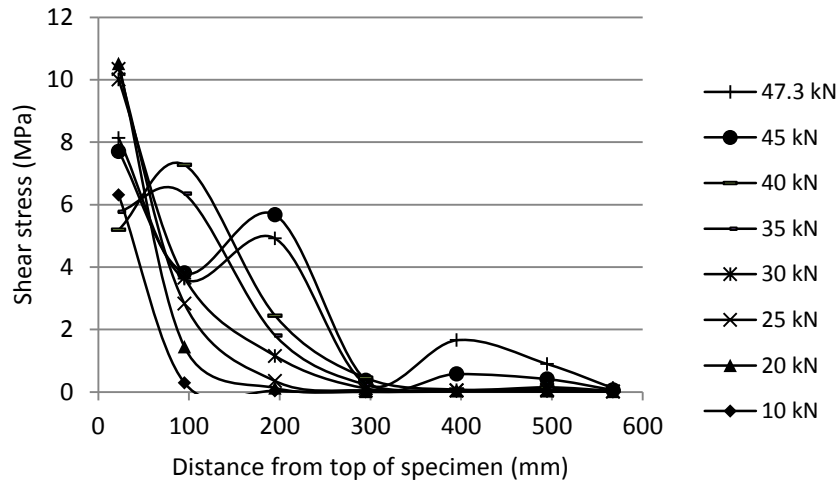


Figure 47: Bond shear stress distribution, specimen P5 (GFRP-reinforced)

Local bond slip was calculated from local strain readings by integrating the strain data using the trapezoid rule. Consistently with Dizhur et al. (2013), slip at the unloaded end of the specimens was neglected. Local bond slip was calculated for the same locations as the shear stress readings, and are displayed in Figure 48, Figure 49, Figure 50, and Figure 51, each indicating the bond stress-slip relationship for locations 22.5mm, 95mm, and 195mm from the loaded end of the specimen.

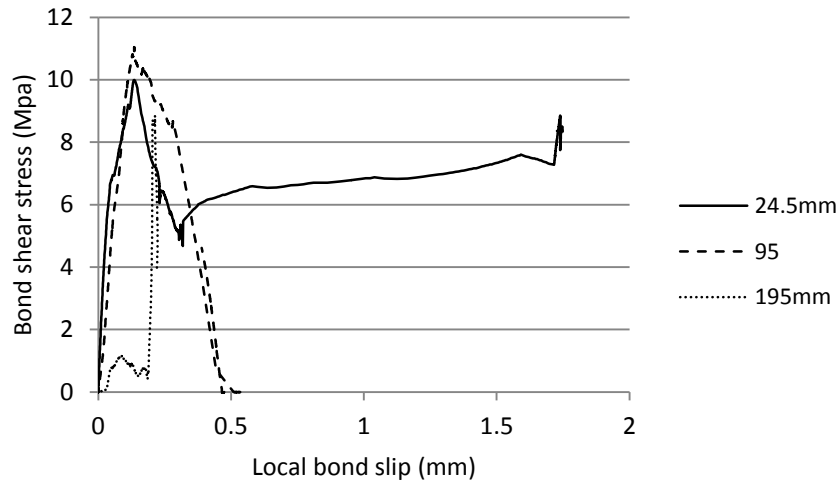


Figure 48: Bond shear stress vs. slip, specimen P3 (steel-reinforced)

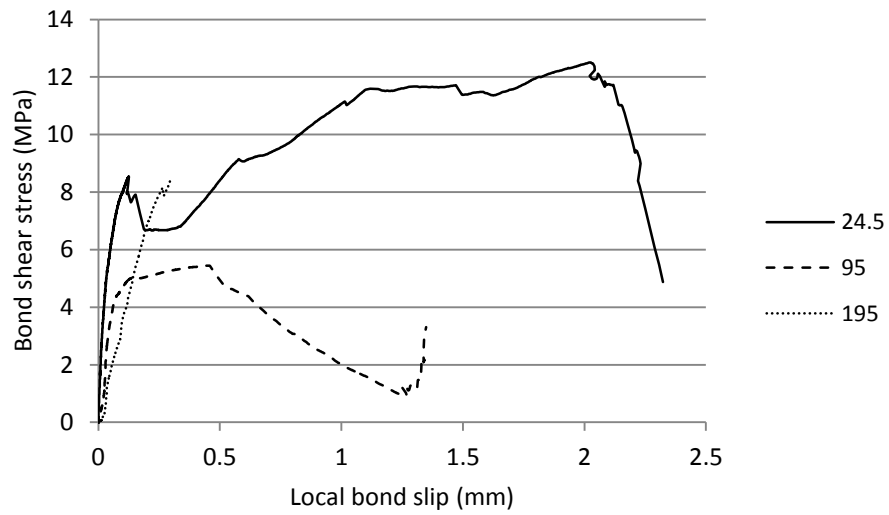


Figure 49: Bond shear stress vs. slip, specimen P4 (GFRP-reinforced)

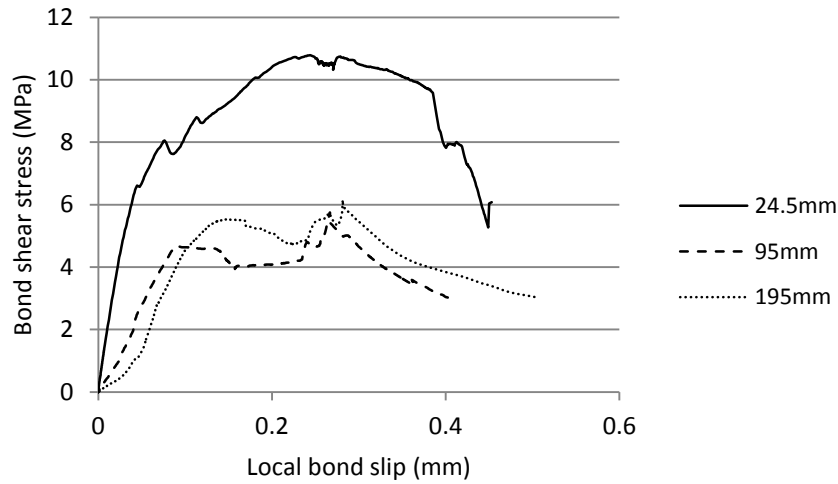


Figure 50: Bond shear stress vs. slip, specimen P2 (steel-reinforced)

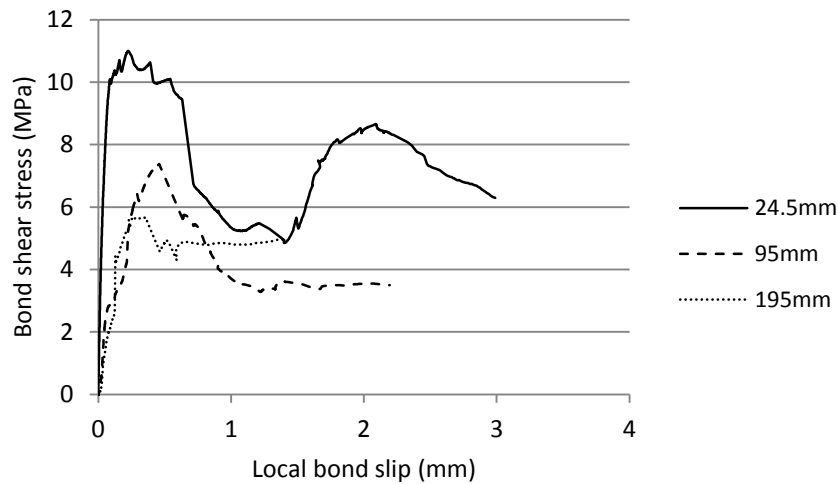


Figure 51: Bond shear stress vs. slip, specimen P5 (GFRP-reinforced)

Figure 52: Bond shear stress vs slip, specimens P1-P5 (24.5mm from top of specimen) Figure 52 displays the shear slip curves for all six pull-out specimens at 24.5mm from the loaded end of the specimen. From this figure it appears that the bond shear-slip relationship is independent from the reinforcing bar material and loosely follows a bilinear behaviour. A

major feature however not captured by the bilinear model is the large shear plateau observed in the GFRP-reinforced specimens. As this behaviour is likely due to local confinement, it is natural that it be not properly captured by a simple bilinear shear-slip model.

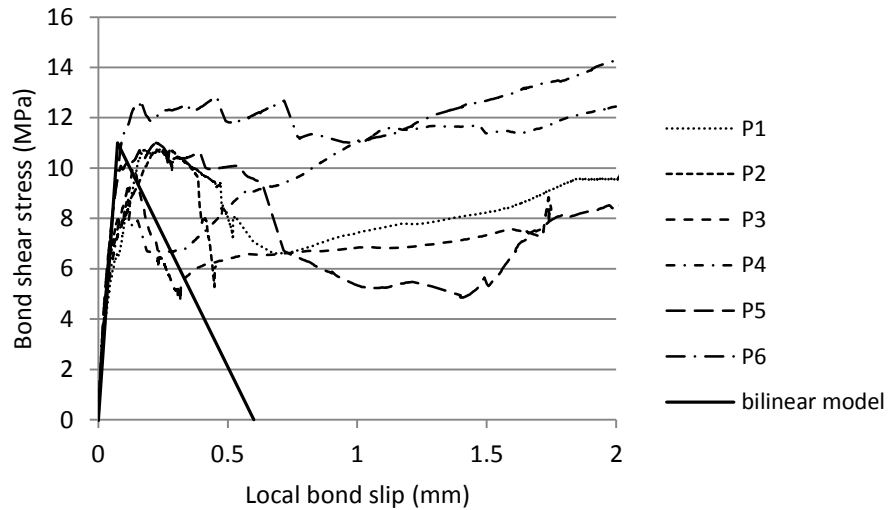


Figure 52: Bond shear stress vs slip, specimens P1-P5 (24.5mm from top of specimen)

4.1.4 Discussion

It should also be noted that visible rust and packing grease that coated the steel reinforcing bars was removed for this test to limit their possible interference with the bonding of the epoxy grout. This may not be representative of the condition of steel reinforcing bars used in the field; the effect of small amounts of rust and grease on the bond with the epoxy grout will require further study.

During loading, some lifting of the base from the lower cross-head of the load frame, as well as deviation of the masonry specimen from the vertical was observed at load levels approaching failure. This behaviour, shown in Figure 53, likely lowered the apparent ultimate strength of the free reinforcing bar by concentrating stresses on one side of the bar. This

eccentricity in loading of the bar, demonstrated in Figure 54, explains the lower failure loads for bar rupture observed in this section when compared to those observed in Section 3.6.



Figure 53: Pull-out specimen: base lifting during testing

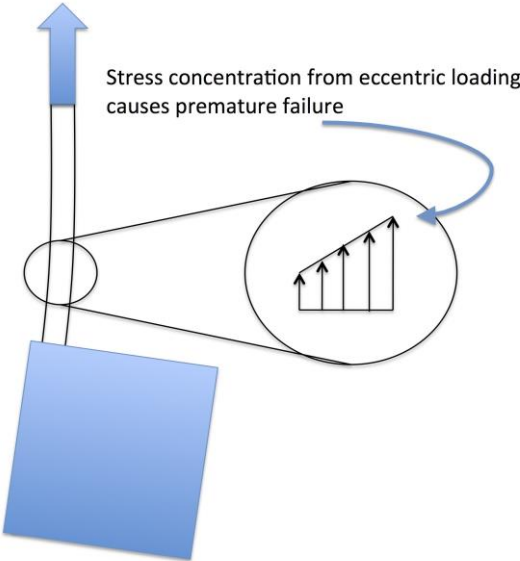


Figure 54: Stress concentration due to eccentric loading

The higher stiffness of the steel reinforcing bars when compared to the GFRP bars is evident through the higher stress levels in the steel-reinforcing bars near the base of the pull-out

specimens at low stress levels (up to 50% of the failure load), when compared to the specimens reinforced with GFRP. Taking a closer look at the distribution of stresses within the reinforcing bars, it may be noted that for every specimen, stress within the bars decrease with increasing distance from the loaded end. Furthermore, at low to moderate load levels, stress levels in the bar decrease rapidly from the loaded end of the specimen to a depth of 200mm. For specimens that failed by rupture of the reinforcing bar, stresses remain very low in the bottom 200mm of the specimen; however, for specimens that failed by pull-out (e.g. P2 and P5), as the applied load approached the failure load, the stress distribution approached a linear shape from the upper (loaded) end of the specimen to the bottom, with significant stresses recorded in the bottom 200mm of the specimens.

The bond shear distribution and shear slip diagrams together characterize the deterioration of the bond between the reinforcing bar and the masonry system with increasing load. For specimens P2 and P5 (see Figure 46 and Figure 47), which failed by pull-out, increasing bond shear stress in the top 50mm of the specimen is observed until approximately 50% of the failure load is applied; shear stress in that region then decreases with increasing applied load. This behaviour indicates shear-softening in the upper bonded region of the specimen. Figure 50 and Figure 51 clearly show increasing then decreasing shear stress with increasing slip at locations 95mm and 195mm from the loaded end, further indicating that the high shear strength attained in the top 50mm of the specimen is not attained in the lower portions of the specimen. This suggests that damage incurred by the specimen during loading and shear-softening of the upper portion of the specimens can cause reduced bonding capacity further down the specimen. Specimens P3 and P4 which failed by bar rupture also displayed some shear softening in the upper 50mm of the bond between the reinforcing bar and the masonry, however

the bonded regions further away from the loaded end of the specimen showed similar shear strength to that of the first 50mm of the bond, indicating better maintenance of bond integrity away from the shear-softened regions for those specimens.

The bonding characteristics of the reinforcing bar-epoxy-masonry interface display similar characteristics to those observed by Dizhur et al. (2013), however the descending portion of the shear-slip curve differ greatly. Dizhur et al. (2013) observed decreasing shear stress approaching zero within 1mm of slip. Constant or even increasing shear stress at slip levels far beyond 1mm observed in this experimental procedure may be attributed to increased confinement of the bonded region afforded by a larger masonry specimen.

4.2 Flexural testing

Flexural test specimens consisted of 6-high SRCMU prisms fitted with reinforcing bars in the central reinforcement channel of both face shells. The reinforcement of both faces of the flexural specimens imparted sufficient strength to the specimens for them to be lifted in place and tested in flexure while standing vertically. The height of the specimens was limited to the maximum practical height at which masons could comfortably construct the specimens, and at which the specimens would remain stable without additional support.

4.2.1 Specimen fabrication

First, the prisms into which the reinforcing bars would be mounted were constructed. Casting of prisms was performed by professional masons following the procedure outlined in Section 3.1.1. The prisms were then allowed to cure under a polymer sheet at 100% relative humidity for 14 days, then allowed to dry for 7 days prior to the installation of the reinforcing bars.

Six steel and six GFRP reinforcing bars were cut to a length of 1290mm. This length was selected to accommodate the full height of the masonry prisms (1190mm) in addition to 100mm

excess length to aid in positioning the bar during the epoxy grouting procedure. The steel bars were brushed with a rotary wire brush to remove any excess oil and oxidation. Strain gauges were installed at the locations indicated in Figure 55 following the procedure outlined in Section 3.4.1.1. Three each of the steel and GFRP reinforcing bars were fitted with three strain gauges; these strain gauges would be located at the central mortar joint and 100mm above and below on the tension side of the specimen during testing as shown in Figure 56. The remaining bars were fitted with a single electronic strain gauge, located such that it would monitor strains at the central mortar joint of the specimen on the compression side during testing. Each bar was then fitted with 2 twisted wire depth markers at approximately third points of the bars, the end of which would indicate the 15mm required thickness of epoxy cover.

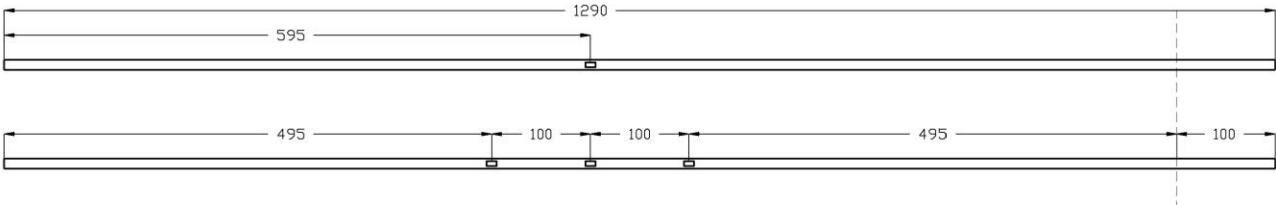


Figure 55: Flexural specimen reinforcement strain gauge location

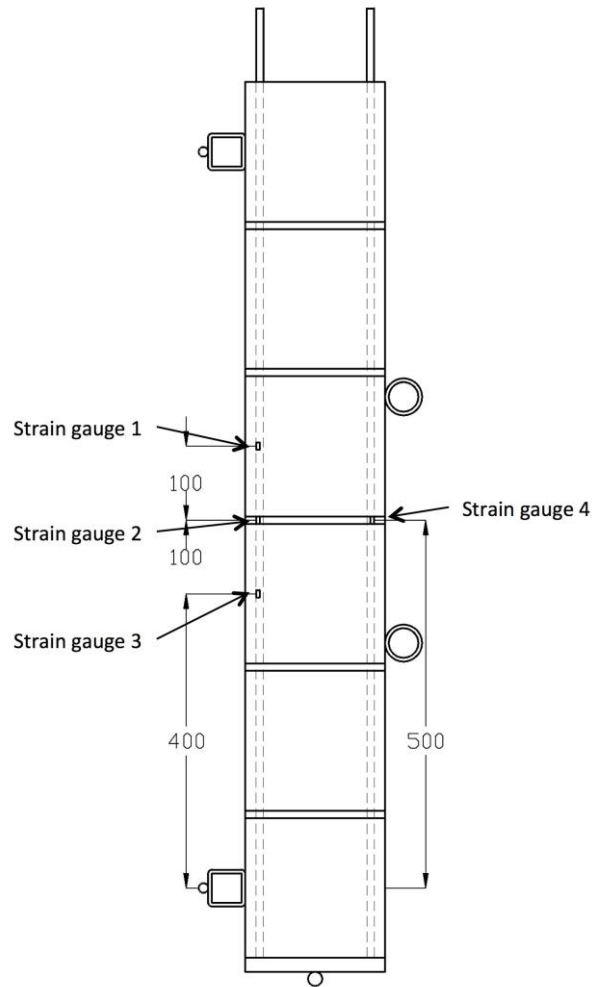


Figure 56: Flexural specimen strain gauge locations

The flexural specimens were reinforced while free-standing in a vertical position at the location at which they were cast in order to simulate the conditions expected on construction sites for field applications of NSM reinforcement to SRCMU systems and to avoid unnecessarily moving the specimens. The reinforcement channel in which the reinforcing bar was to be installed was prepared according to the instructions provided by the manufacturers of the dowelling epoxy used for the installation of reinforcing bars; the inner surfaces of the reinforcement channel was brushed with a stiff wire brush, then cleared of debris by blowing it

out with compressed air (this procedure was repeated twice as per the manufacturer's instructions). The surface of the face shell on either side of the reinforcement channel was lined with adhesive tape to protect the concrete from excess epoxy. A reinforcing channel was then first half-filled with epoxy grout, then a prepared reinforcing bar was carefully pressed into place until the end of the wire depth markers were centred in the reinforcement channel and flush with the surface of the face-shell. The reinforcement channel was then filled in with epoxy and the surface trowelled smooth. The adhesive tape on either side of the reinforcement channel was removed prior to the epoxy setting.

Finally, mounts for pi-gauges and Linear Variable Differential Transducers (LVDT) were glued in place using hot-glue, then secured using 2-part epoxy adhesive. The mounts for the pi-gauges were located along the centreline of the face-shells on the tension side of the specimens; these were precisely placed using a jig to locate them exactly 200mm centre to centre from each-other. Mounts for the LVDTs were located on the sides of the specimens near the mid-span. Since the mid-span of the specimens was located at a mortar joint, which would most likely fail during testing, the mounts were placed on the SRCMUs directly above and below the central mortar joint. The location of each mount is indicated in Figure 57.

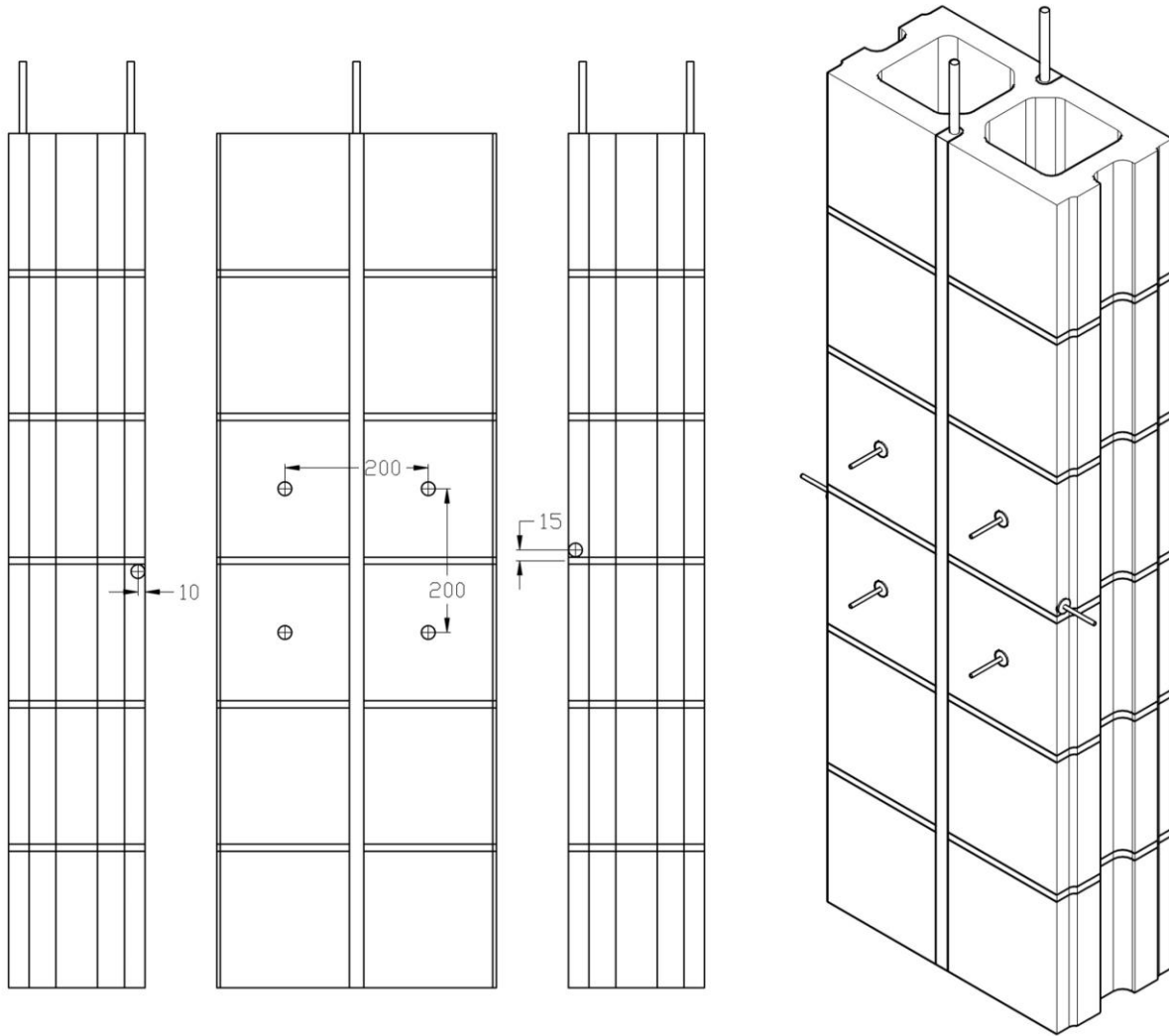


Figure 57: Flexural specimen, pi-gauge and LVDT mount locations

Table 21 indicates the age of the blocks, prism, and epoxy at the time of testing for each of the flexural specimens.

Table 21: Flexural specimen age at time of testing

Specimen number	Reinforcing bar type	Average age of SRCMUs (days)	Age of prism (days)	Age of epoxy grout (days)
F1	Steel	155	28	11
F2	Steel	159	28	11
F3	Steel	152	30	13
F4	GFRP	158	28	11
F5	GFRP	151	30	13
F6	GFRP	153	30	13

4.2.2 Test set-up

The test set-up was constructed in order to allow each specimen to be loaded under conventional 4-point loading conditions where external loads are applied at third points along the unsupported length of a simply-supported specimen. A diagram indicating the locations of supports and external loads is provided in Figure 58. The supports were located along the centreline of the uppermost and lowermost blocks of the specimens (1000mm apart). Loading points were located 333mm from either support.

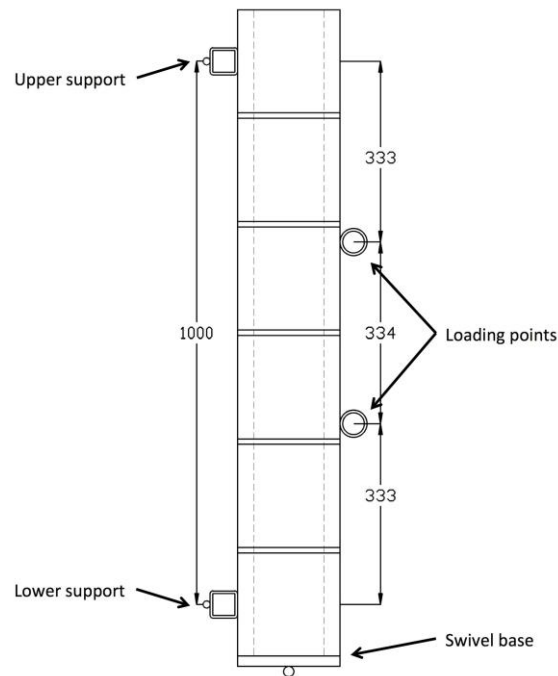


Figure 58: Flexural four-point loading conditions

The supports were maintained in place by welding them onto the reaction frame as shown in Figure 59. This frame was designed to sustained loads much larger than those expected for this test without significant deflection, and was anchored to the laboratory strong-floor. The supports themselves were set on swivels to allow free rotation. The specimens were supported at the bottom by a vertically adjustable base support, also set on a swivel.

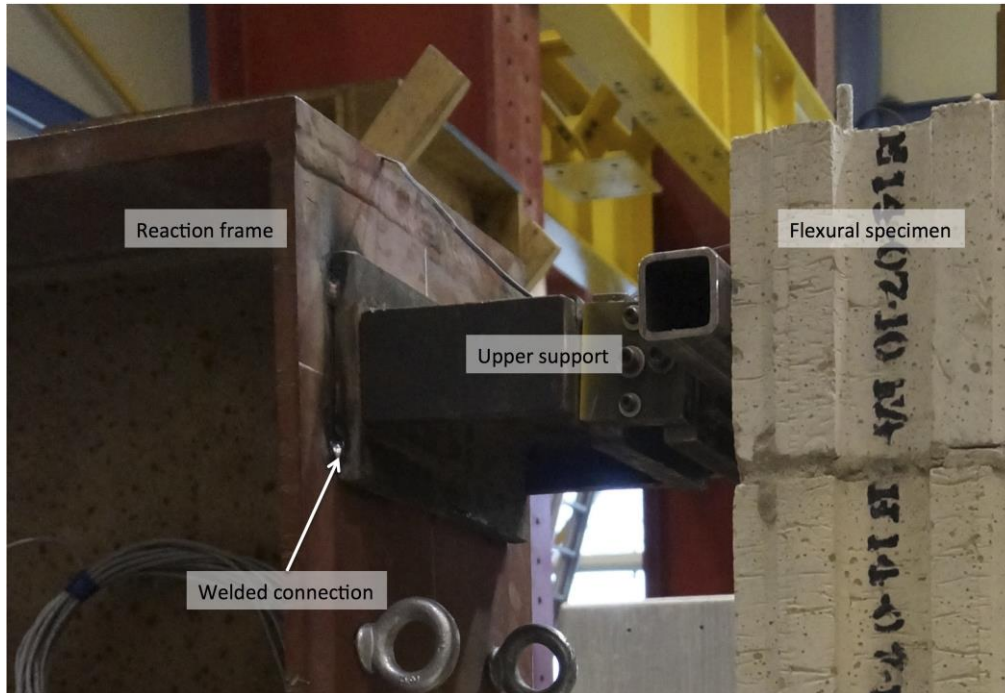


Figure 59: Flexural test set-up: welded support

The out-of-plane loads were applied through the loading jig. A rectangular steel Hollow Structural Section (HSS) was welded to two circular steel HSS segments to hold the latter parallel to each other at a distance of 334mm. A swivel support was attached to the middle of the rectangular HSS to allow it to be attached to the loading actuator. The actuator was itself fixed to a reaction frame, and chained in place in order to keep it in horizontal alignment during testing. The entire set-up is shown in Figure 60 and Figure 61.



Figure 60: Flexural test set-up



Figure 61: Flexural test set-up: close up

It was also necessary to construct a lifting jig to position the reinforced specimens for testing. The jig shown in Figure 62 consists of a 12mm steel plate welded to 2 steel angles fitted with holes for lifting shackles. Specimens were lifted into place using the laboratory's overhead crane, then secured to the support frame using bar clamps as shown in Figure 63. The loading jig was then brought into contact with the specimen by advancing the hydraulic actuator. The specimens were loaded under displacement control at a rate of 0.5mm/minute. The bar clamps were removed from the specimen once the total applied load exceeded 1kN. Loading continued for all specimens until a drop off in load of at least 90% occurred.



Figure 62: Flexural specimen hoisting jig

Table 22: Flexural specimens maximum load

Specimen ID	Reinforcement material	Maximum load (kN)	Deflection at mid-span at maximum load (mm)	Maximum deflection at mid-span (mm)
F1	10M steel rebar	40.6	2.33	3.69
F2	10M steel rebar	41.5	2.57	8.91
F3	10M steel rebar	49.6	6.36	6.36
F4	#3 GFRP bar	38.5	9.10	12.18
F5	#3 GFRP bar	32.7	4.70	6.20
F6	#3 GFRP bar	34.6	7.30	11.44

Figure 64 and Figure 65 show the load-deflection diagram for the steel-reinforced, and GFRP-reinforced specimens, respectively. The deflection readings displayed are the average of the two LVDTs used for each specimen.

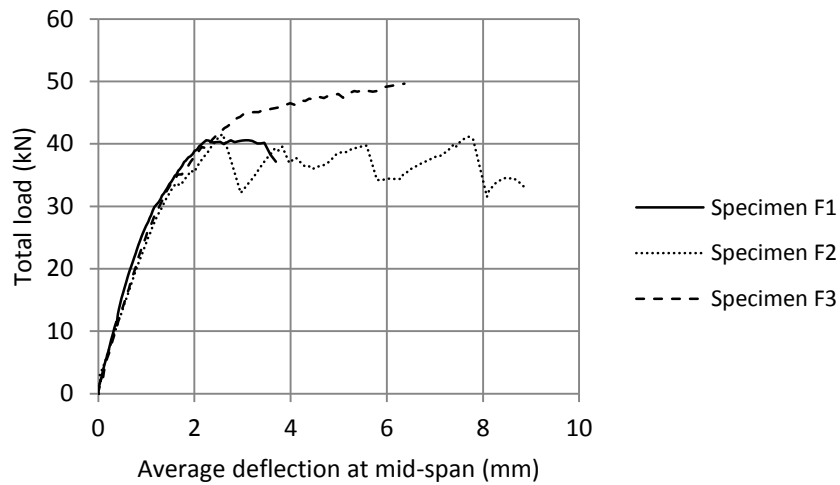


Figure 64: Load vs. deflection, steel-reinforced flexural specimens

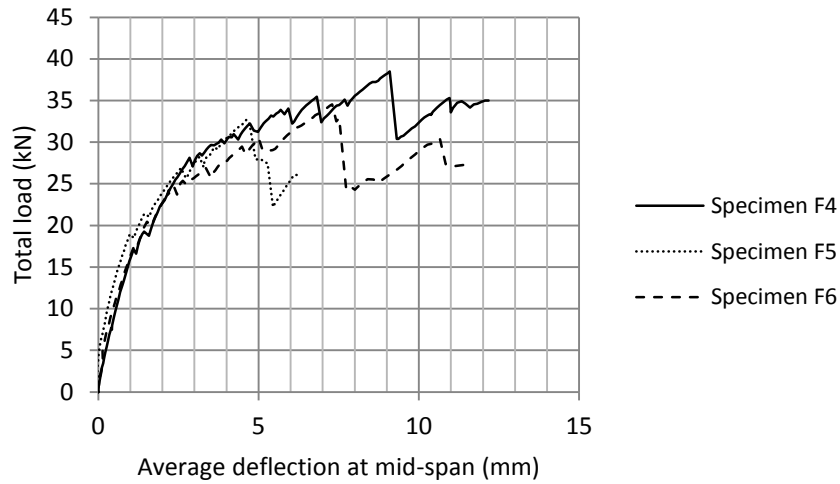


Figure 65: Load vs. deflection, GFRP-reinforced specimens

Figure 66 and Figure 67 show the width of the crack opening at the central mortar joint for the steel-reinforced and the GFRP-reinforced specimens. The crack width data shown is the average from the two pi-gauges used for each specimen.

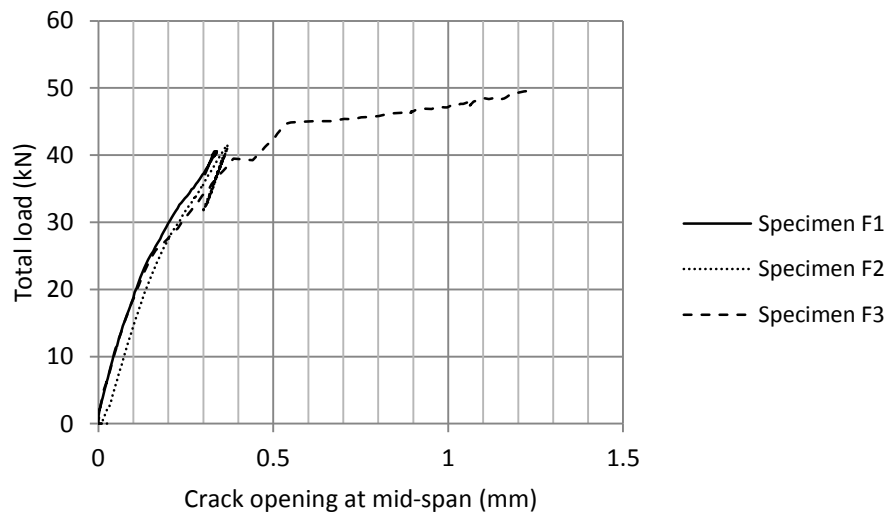


Figure 66: Load vs. crack opening width, steel-reinforced flexural specimens

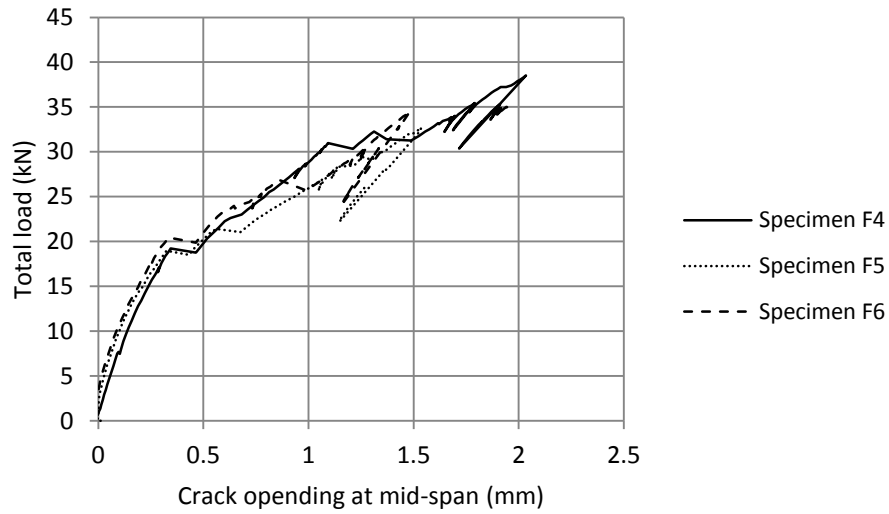


Figure 67: Load vs crack opening width, steel reinforced flexural specimens

Strain data from a sample steel-reinforced specimen (F1) is shown in Figure 68. Strain data from a sample GFRP-reinforced specimen (F4) is shown in Figure 69. Note that the strain gauge numbers correspond to those indicated in Figure 56.

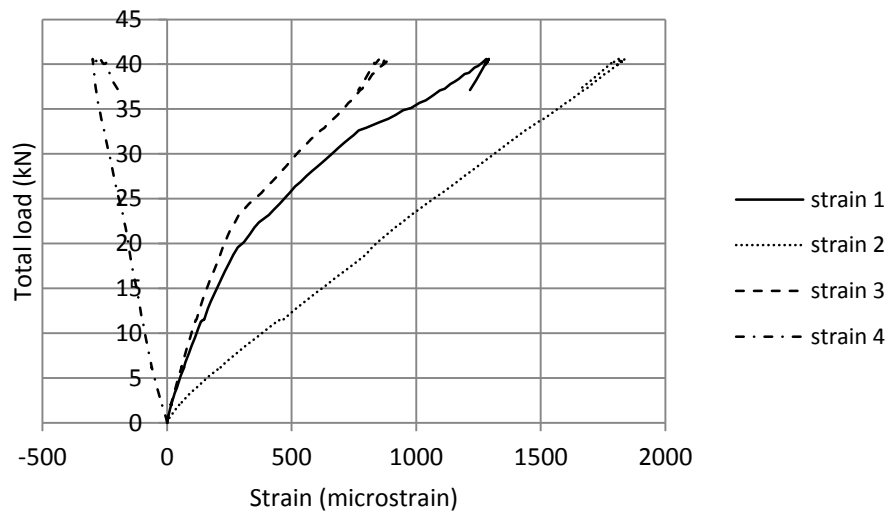


Figure 68: Load vs. strain, steel-reinforced specimen F1

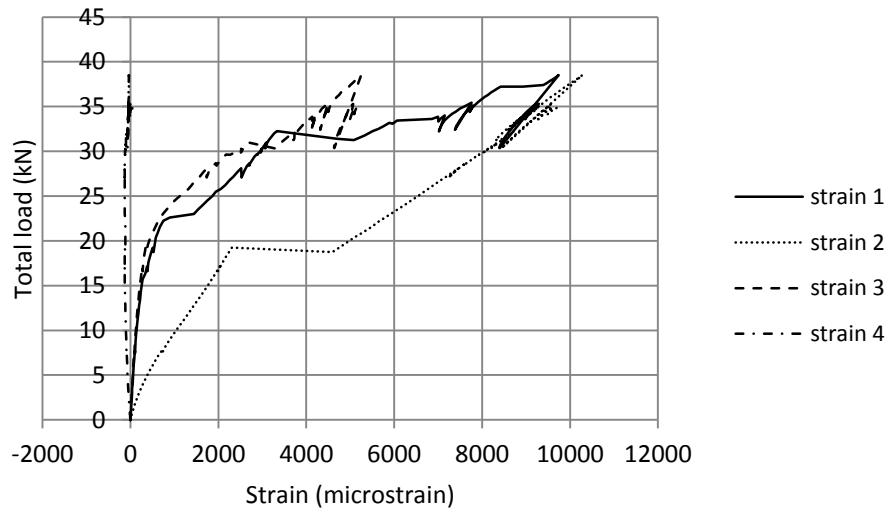


Figure 69: Load vs. strain, GFRP-reinforced specimen F4

4.2.4 Discussion

It is important to note that all six flexural specimens failed in shear because their limited height forced a high shear force to accompany increases in moment. It is unusual for a designed structural masonry section to be expected to fail in out-of-plane tension shear because this is a brittle mode of failure; however in this set of laboratory tests, shear failure prevented the test-specimens from reaching their full flexural capacity. In other words, the capacity of the reinforced SRCMU assembly was so high that it forced a different mode of failure to occur. The flexural behaviour of specimens F1 through F6 are studied in this section.

4.2.4.1 Flexural behaviour

Comparing the load-deflection curves of the steel-reinforced specimens to that of the GFRP-reinforced specimens, it may be noted that the former are much stiffer. This is due to the high elastic modulus and larger cross-sectional area of the steel rebar when compared to the GFRP reinforcing bars. The stress-strain behaviour of the flexural specimens was also compared to that

predicted by the equations for Serviceability Limit State (SLS) design from CSA S304.1 based on the transformed masonry section.

When the behaviour of a section is controlled by flexure, the load-deflection relationship is governed by the Young's modulus (E) and moment of inertia (I) of the object being studied; together these two properties make up an object's stiffness. Common practice in civil engineering is to use a material's bulk Young's modulus and calculate the global moment of inertia based on a transformed section, accounting for dissimilar materials by converting them analytically to the bulk material using a modular ratio. "I" is calculated before and after cracking of the masonry since a large drop in stiffness occurs after cracking. The notation indicated in Table 23 is used in the calculations associated with CSA S304.1 deflection calculations.

Table 23: Notation used for moment of inertia calculations

A_{ep}	Cross-sectional area of epoxy grout within a masonry section
A_{rs}	Cross-sectional area of steel reinforcing bars within a masonry section
A_{rg}	Cross-sectional area of GFRP reinforcing bars within a masonry section
b	Length of a single masonry unit
d	Distance from the extreme compression fibre to the centroid of reinforcing bars in tension
d'	Distance from the extreme compression fibre to the centroid of reinforcing bars in compression
d_e	Distance from the extreme compression fibre to the centroid of dowelling epoxy in tension
d_e'	Distance from the extreme compression fibre to the centroid of dowelling epoxy in compression
I_{cr1}	Moment of inertia of cracked masonry where epoxy in tension contributes to stiffness
I_{cr2}	Moment of inertia of cracked masonry where epoxy in tension does not contribute to stiffness
I_h	Moment of inertia of the hollow cores of a CMU
I_{mcr}	Moment of inertia of the uncracked portion of masonry within a cracked masonry section
I_o	Uncracked moment of inertia
I_p	Moment of inertia of a fully solid CMU (no hollow)
I_r	Moment of inertia of a reinforcing bar relative to the neutral axis of the CMU in which it is placed
kd	Depth from the extreme compression fibre of a cracked masonry section to the neutral axis
n_e	Modular ratio of epoxy grout relative to masonry
n_{rg}	Modular ratio of GFRP reinforcing bars relative to masonry
n_{rs}	Modular ratio of steel reinforcing bars relative to masonry
S_{ec}	Moment of area of epoxy grout in compression within a cracked section
S_{et}	Moment of area of epoxy grout in tension within a cracked section
S_m	Moment of area of masonry within a cracked section
S_{rc}	Moment of area of reinforcing bars in compression within a cracked section
S_{rt}	Moment of area of reinforcing bars in tension within a cracked section
t	Total CMU thickness
t_f	CMU faceshell thickness
t_w	Total web thickness

Material properties:

The material properties for the masonry assembly, steel reinforcing bars, and GFRP reinforcing bars are taken from the material tests performed in Chapter 3. Material properties for the dowelling epoxy were obtained from the manufacturer's material data sheet (properties at 7 days age). Properties used in this section are listed in Table 24.

Table 24: Material properties for stiffness calculations

Material	Modulus of elasticity (E)	Modular ratio (n)
Masonry assembly	18.5GPa	1
Steel rebar	173.7GPa	$n_{fs}=9.4$
GFRP bar	44.1GPa	$n_{fg}=2.4$
Dowelling epoxy	5.5GPa	$n_e=0.3$

Uncracked section:

The uncracked moment of inertia (I_o) of a reinforced hollow SRCMU section may be calculated following equation (32). The moment of inertia of the outer perimeter (I_p) of the specimen is calculated, from that bulk moment of inertia is subtracted the moment of inertia of the hollow portions of the section (I_h), then the additional stiffness attributed to the epoxy and reinforcing bars (I_r) is added.

$$I_o = I_p - I_h + I_r \quad (32)$$

Where, for the flexural specimens from Chapter 4:

$$I_p = \frac{bt^3}{12} \quad (33)$$

$$I_h = \frac{(b - t_w)(t - 2t_f)^3}{12} \quad (34)$$

$$I_r = n_{rs/rg} A_{rs/rg} \left(d - \frac{t}{2} \right)^2 + n_s A_{sp} \left(d_s - \frac{t}{2} \right)^2 \quad (35)$$

4.2.4.2 Cracked sections

The cracked moment of inertia (I_{cr}) of a reinforced hollow SRCMU may be calculated by first determining the depth to neutral axis of the cracked section. The moment of inertia is then calculated based on the stiffness contribution of the elements in compression and those in tension. For completeness, two scenarios must be considered; first the case where the only the masonry is cracked, then the case where both the masonry and doweling epoxy are cracked.

Considering firstly the case where only masonry is cracked, the depth to neutral axis (kd) is calculated using the equilibrium of Moment of area (S) equation (36). The sum of moments of area about the neutral axis must be equal to zero.

$$0 = S_m + S_{ec} + S_{rc} + S_{st} + S_{rt} \quad (36)$$

Where:

Moment of area of masonry:

$$S_m = \begin{cases} bkd \left(\frac{kd}{2} \right) & 0 < kd < t_f \\ t_f b \left(kd - \frac{t_f}{2} \right) + t_w \frac{(kd - t_f)^2}{2} & t_f < kd < t - t_f \end{cases} \quad (37)$$

Moment of area of epoxy in compression:

$$S_{ec} = n_s A_{sp} (kd - d'_s) \quad (38)$$

Moment of area of reinforcement in compression:

$$S_{rc} = n_{rs/rg} A_{rs/rg} (kd - d') \quad (39)$$

Moment of area of epoxy in tension:

$$S_{et} = n_e A_{ep} (d_e - kd) \quad (40)$$

Moment of area of reinforcement in compression:

$$S_{rt} = n_{rs/rg} A_{rs/rg} (d - kd) \quad (41)$$

For cases where the epoxy is cracked, the contribution from the epoxy in tension is omitted as shown in equation (42). A different value of kd is thereby yielded from the equilibrium equation.

$$0 = S_m + S_{ec} + S_{rc} + S_{rt} \quad (42)$$

Using kd from the previous step, the two cracked moments of inertia may be calculated. For cases where only the masonry is cracked, the moments of area of the various components of the section are summed as shown in equation (43):

$$I_{cr1} = I_{mcr} + I_{ec} + I_{rc} + I_{et} + I_{rt} \quad (43)$$

Where:

Moment of inertia of cracked masonry:

$$I_{mcr} = \frac{b(kd)^3}{3} - (b - t_w) \frac{(kd - t_f)^3}{3} \quad (44)$$

Moment of inertia of epoxy in compression may be approximated as:

$$I_{ec} = n_e A_{ep} (kd - d'_e)^2 \quad (45)$$

Moment of inertia of reinforcement in compression may be approximated as:

$$I_{rc} = n_{rs/rg} A_{rs/rg} (kd - d')^2 \quad (46)$$

Moment of inertia of epoxy in tension may be approximated as:

$$I_{et} = n_e A_{ep} (kd - d_e)^2 \quad (47)$$

Moment of inertia of reinforcement in tension may be approximated as:

$$I_{rt} = n_{rs/rg} A_{rs/rg} (kd - d)^2 \quad (48)$$

For cases where both the epoxy and masonry are cracked, the contribution from the epoxy in tension is omitted as shown in equation (49).

$$I_{cr2} = I_{mcr} + I_{ec} + I_{rc} + I_{rt} \quad (49)$$

The uncracked and cracked moments of inertia for the GFRP-reinforced and steel-reinforced sections are listed in Table 25.

Table 25: Reinforced masonry moment of inertia

Moment of inertia condition	Steel-reinforced specimen ($\times 10^6 \text{mm}^4$)	GFRP-reinforced specimen ($\times 10^6 \text{mm}^4$)
Uncracked section (I_o)	183.0	174.3
Partially cracked section (I_{cr1})	25.1	8.8
Fully cracked section (I_{cr2})	21.9	5.3

4.2.4.3 Comparison with experimental data

Using the values from Table 25 as well as the deflection equation for 4-point loading and the equation for effective moment of inertia from S304.1, the code-predicted behaviour of the SRCMU masonry system may be compared to the experimental results. Figure 70 and Figure 71 show the experimental data from the steel-reinforced and GFRP-reinforced specimens, overlaid with the code-predicted load-deflection curves assuming elastic reinforcement. Note that the two code-predicted curves represent the two stages of cracking; the partially cracked curve shows the expected behaviour of the section passing from uncracked to the state where only the masonry is cracked, the fully cracked curve shows the expected behaviour of the section passing from uncracked to the state where both the masonry and epoxy materials are cracked in tension. In

Figure 70, the code-predicted curves show a maximum load of 39.0kN which corresponds to the state at which the reinforcing steel yields.

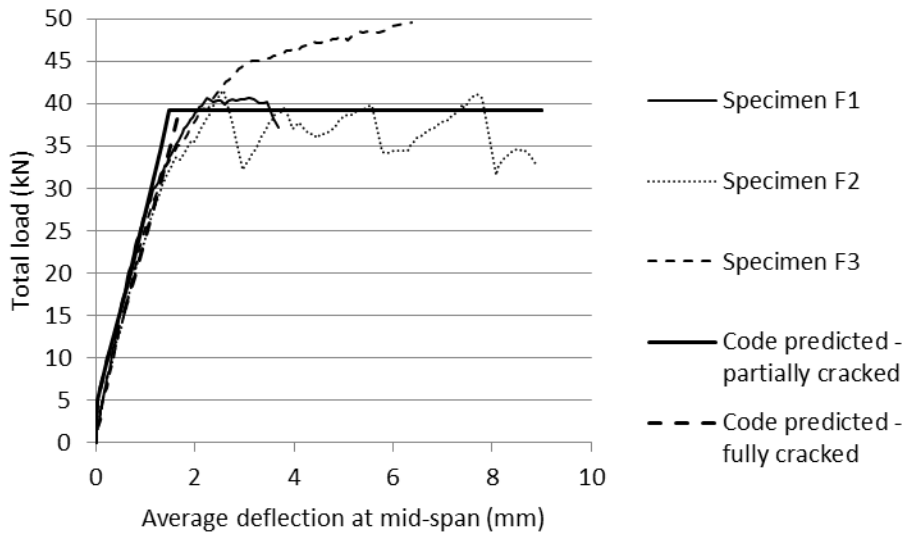


Figure 70: Steel-reinforced flexural displacement with code-predicted behaviour

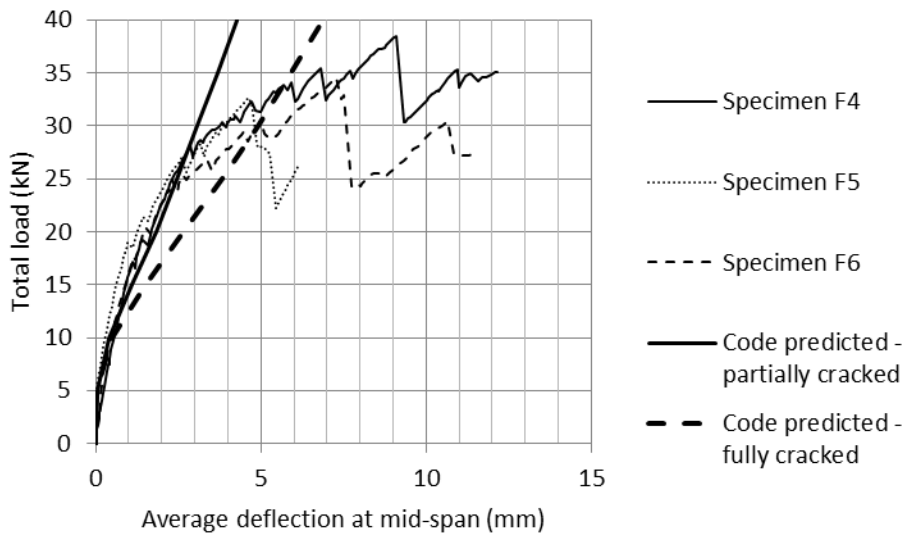


Figure 71: GFRP-reinforced flexural displacement with code predicted behaviour

The code-predicted curves match well with the experimental data up to around 80% of the maximum strength of the specimens; however note that since these code equations are meant

for the serviceability limit state, they do not predict the behaviour at load levels approaching failure. Other important differences may also be observed; the CSA S304.1 SLS deflection equation assumes an increased stiffness at low applied load levels until cracking occurs at the mortar joints, this pre-cracking behaviour was not observed in the experimental data. Furthermore, large deflections begin to occur near 80% of the failure load due to shear displacement of the specimens; this behaviour is also not captured by the S304.1 deflection equations.

A manifestation of the SRCMU systems greater flexural stiffness is displayed in Figure 72 and Figure 73. By overlaying the code-predicted stress-strain curve for a conventionally-reinforced masonry specimen under the same loading conditions with two reinforcing bars grouted into the hollow cores of the specimen, it becomes clear that the SRCMU system deflects on the order of half as much as a conventional masonry system (post cracking) prior to failure.

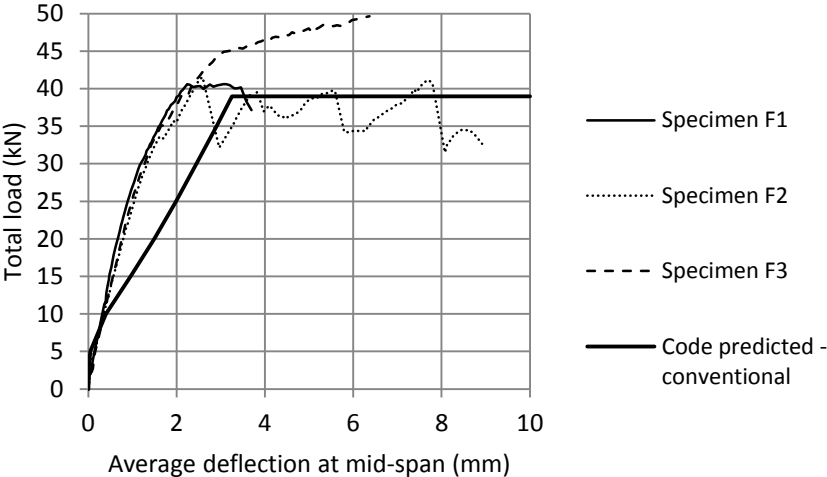


Figure 72: Conventional vs. SRCMU flexural stiffness - steel-reinforced

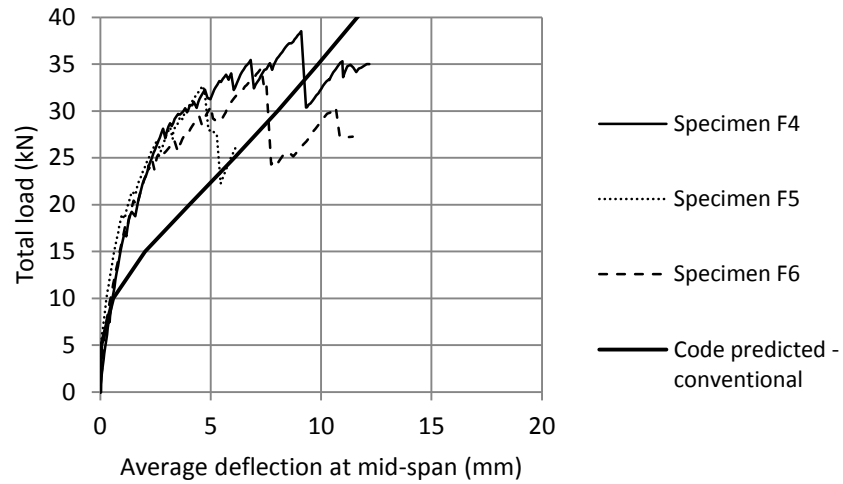


Figure 73: Conventional vs. SRCMU flexural stiffness - GFRP-reinforced

4.2.5 Shear behaviour

All six flexural specimens failed in diagonal tension shear. Furthermore, some sliding shear could be seen through visual inspection, although no instrumentation was in place to quantitatively capture the behaviour.

5 ATENA FEA Analysis

The purpose of this study was two-fold; to show the potential advantages of the SRCMU system over conventional concrete masonry systems, and to perform preliminary testing and generate data to calibrate FEA models thereby facilitating further structural studies. In this chapter, first will be discussed the use of the data collected in Chapter 4 to calibrate FEA models using the ATENA FEA software.

In order to gain a better understanding of the behaviour observed during the testing of pull-out and flexural SRCMU specimens, FEA models were constructed and analyzed using the ATENA FEA software package. This particular FEA package was utilized because of the ease with which it models the cracking behaviour of reinforced concrete elements. The ATENA software package is used by many research groups including one at the University of Manitoba; ATENA revision 5.1.1t, available from Cervenka Consulting (2015), was used for this project.

5.1 Model geometry

To limit the number of elements necessary to model the shape of the SRCMU, the cross-section was constructed using the Cartesian points shown in Figure 74 in the global x-y plane. This cross-section was extruded to a thickness of 190mm for the blocks, and 10mm for the mortar joints in the positive z-direction. The epoxy grout was shaped by extruding the area enclosed within the simplified channel of the SRCMU shape to the full height of the masonry prism being modeled. The reinforcing bar was modeled as a line element.

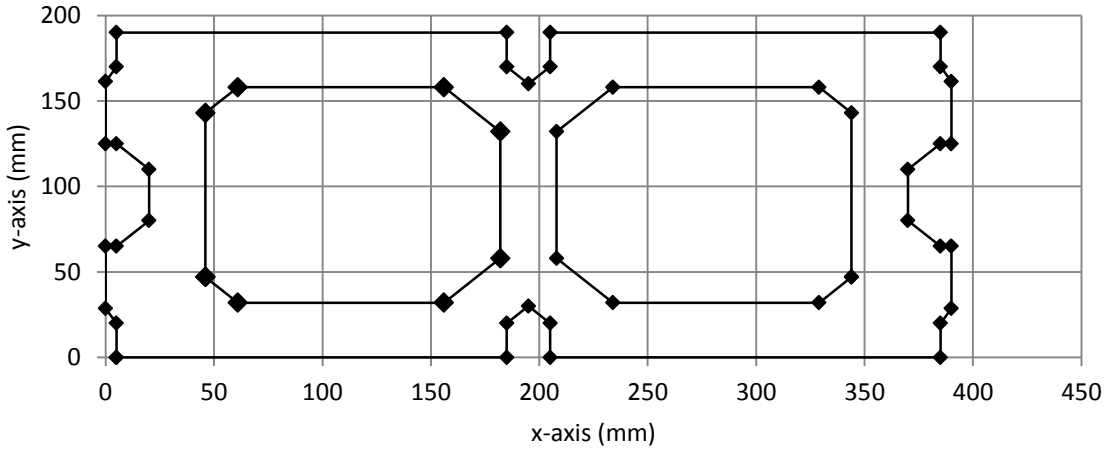


Figure 74: x-y coordinates for SRCMU cross-section numerical model

The full three-high specimen was constructed to simulate the pull-out specimens. The full model including the three SRCMUs, two mortar joints and top steel plate is shown in Figure 75. Note that the reinforcing bar was terminated at the surface of the epoxy grout.

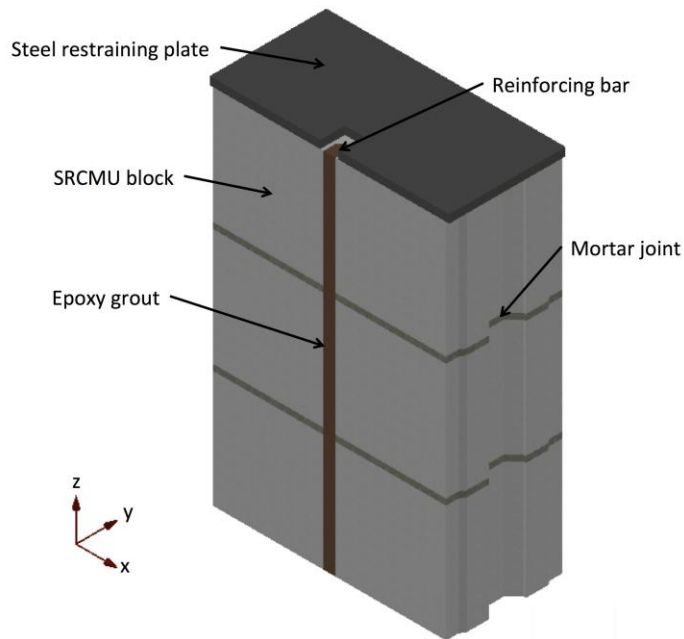


Figure 75: Pull-out FEA model

To accelerate the numerical analysis, only half of the flexural SRCMU specimen was modeled. The models were terminated at mid-span and the boundary conditions were adjusted to reflect the behaviour of the full-sized specimen. The model specimen therefore consisted of three SRCMUs, two mortar joints, one half-thickness mortar joint, one supporting steel bar and one loading steel bar as shown in Figure 76.

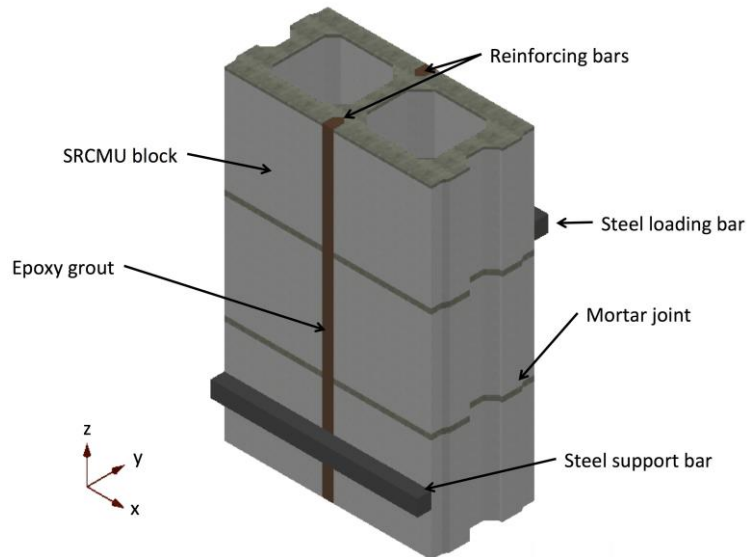


Figure 76: Flexural FEA model

The SRMUs and supporting/loading steel bars were meshed with tetrahedral elements with a nominal size of 20mm. The mortar joints were meshed with tetrahedral elements with a nominal size of 10mm. Reinforcing bars consisted of continuous line segments with nodes at the locations of strain gauges. For simplicity, all material contacts were first assumed to be fully bonded. Two reinforcement bond models, expressed through a shear-slip model between the reinforcing bars and the epoxy substrate, were also explored in the pull out analyses.

5.2 Material properties

The properties of the materials used in the ATENA FEA model were based on built-in material models and adjusted based on experimental evidence gathered through the preceding experimental procedures as well as relevant literature and codes. A complete breakdown of the material properties accounted for by the modeling software for this section is provided in Table 26; this table also provides the reasoning for each property assigned.

Table 26: ATENA FEA material properties

Base Material	Material model type	Property	Value	Justification/evidence		
SRCMU (concrete)	Cementitious Material II	Compressive strength f'_c	32.7 MPa	Concrete cylinder testing (Chapter 3)		
		Young's modulus, E	18.5 GPa	Masonry prism testing (Chapter 3)		
		Poisson ratio, μ	0.2	Material model default		
		Tensile strength f_t	2.42 MPa	Material model default based on $f_{cu}=38.5$ MPa		
		Fracture energy G_F	6.048×10^{-5} MN/m	Material model default based on $f_{cu}=38.5$ MPa		
		Critical compressive displacement, W_d	5×10^{-4} m	Material model default based on $f_{cu}=38.5$ MPa		
		Critical plastic strain, ϵ_{cp}	8.736×10^{-4}	Material model default based on $f_{cu}=38.5$ MPa		
		Relative compressive strength due to cracking, $r_{c,lim}$	0.2	Material model default based on $f_{cu}=38.5$ MPa		
		Aggregate interlock	-	No large aggregate in concrete mix		
		Failure surface eccentricity	0.52	Material model default based on $f_{cu}=38.5$ MPa		
		Crack model coefficient	1	Material model default based on $f_{cu}=38.5$ MPa		
		Mortar joints (concrete)	Cementitious Material II	Compressive strength (cube), f_{cu}	12 MPa	Typical value
				Compressive strength (cylinder), f'_c	10.2 MPa	Material model default based on $f_{cu} = 12$ MPa
Young's modulus, E	12.1 GPa			CSA A23.3 based on $f'_c=10.2$, $\gamma_c=1800$		

		Poisson ratio, μ	0.2	Material model default
		Tensile strength f_t	0.8 MPa	Recommended value, CSA S304.1 Table 5
		Fracture energy G_F	3.15×10^{-5} MN/m	Material model default based on $f_{cu}=12$ MPa
		Critical compressive displacement, W_d	5×10^{-4} m	Material model default based on $f_{cu}=12$ MPa
		Critical plastic strain, ϵ_{cp}	5.060×10^{-4}	Material model default based on $f_{cu}=12$ MPa
		Relative compressive strength due to cracking $r_{c,lim}$	0.2	Material model default based on \
		Aggregate interlock	-	No large aggregate in concrete mix
		Failure surface eccentricity	0.52	Material model default based on $f_{cu}=12$ MPa
		Crack model coefficient	1	Material model default based on $f_{cu}=12$ MPa
Epoxy grout	Cementitious Material II	Compressive strength (cube), f_{cu}	85 MPa	Manufacturer's Material Data Sheet
		Compressive strength (cylinder), f'_c	72.2 MPa	Material model default based on $f_{cu}=85$ MPa,
		Young's modulus, E	5 GPa	Manufacturer's material data sheet
		Poisson ratio, μ	0.2	Material model default
		Tensile strength f_t	23.5 MPa	Recommended value, CSA S304.1 Table 5
		Fracture energy G_F	1.0×10^{-7} MN/m	Typical value
		Critical compressive displacement, W_d	5×10^{-4} m	Material model default based on $f_{cu}=85$ MPa
		Critical plastic strain, ϵ_{cp}	1.674×10^{-3}	Material model default based on $f_{cu}=85$ MPa
		Relative compressive strength due to cracking $r_{c,lim}$	0.2	Material model default based on $f_{cu}=85$ MPa
		Aggregate interlock	-	No large aggregate
		Failure surface eccentricity	0.52	Material model default based on $f_{cu}=85$ MPa
		Crack model coefficient	1	Material model default based on $f_{cu}=85$ MPa
GFRP reinforcing bar	Reinforcing bar (linear-elastic)	Young's modulus, E	44.1 GPa	Bar tension test (Chapter 3)

		Cross-sectional Area	71.3mm ²	Material Data Sheet
		Perimeter	31.5mm	Direct measurement
Steel reinforcing bar	Reinforcing bar (bi-linear)	Young's modulus, E	173.7 GPa	Bar tension test (Chapter 3)
		Yield stress, f _y	436.0 MPa	Bar tension test (Chapter 3)
		Maximum stress	612.2MPa	Bar tension test (Chapter 3)
		Strain at end of yield plateau	19035 microstrain	Bar tension test (Chapter 3)
		Strain at maximum stress	148000 microstrain	Bar tension test (Chapter 3)
		Cross-sectional area	100mm ²	Nominal value
		Perimeter	35.5mm	Direct measurement
Steel plate	Linear-elastic	Young's modulus	200GPa	Typical value for steel

The models used to dictate the shear-slip relationship between the reinforcing bars and the epoxy substrate are shown in Table 27.

Table 27: Reinforcement bond models

Bond for reinforcement name	Coordinated of multilinear model [mm,MPa]	Graphical model
Perfect bond	-	-
Bond model 1	[0,0];[0.1,11];[0.6,0.01];[1000,0.01]	
Bond model 2	[0,0];[0.1,11];[1000,11]	

5.3 Support and loading conditions

The pull-out specimen model was supported only at the top surface of the restraining plate. This surface was restrained in movement in the x, y, and z directions. Loading was simulated by controlling the displacement of the epoxy material at the point where the reinforcing bar reaches the top surface of the specimen, at coordinates (195;20;590). Displacements were completed in increments of 0.005mm. Body loads were neglected. The location of the supports and loads for the pull-out specimens are indicated in Figure 77.

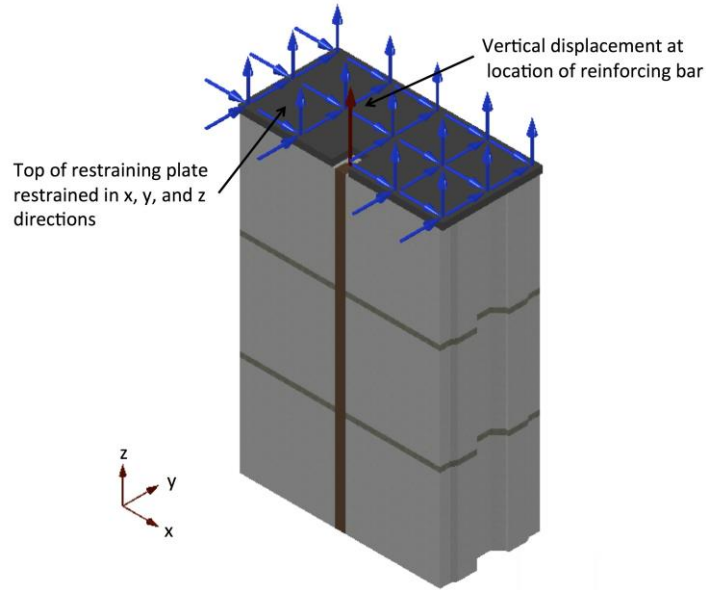


Figure 77: Pull-out FEA model, support/loading conditions

The flexural model was restrained at two locations. A 25mm thick steel bar with a width and length of 30mm and 190mm, respectively was located at the mid-height of the bottom block; the centerline of the free surface of that support was restrained against movements in the x and y directions. The top of the central mortar half-joint as well as the tops of the beads of epoxy were restrained against movement in the z direction only, to simulate vertical continuity and symmetry of the flexural specimen. The specimen was loaded by controlling the displacement of the central point of the loading steel plate; a 25mm thick steel bar with a width and length of 30mm and 190mm, respectively and located on the opposite side of the model from the support bar and 333mm higher in the z-direction. Displacements were completed in increments of 0.02mm. Body loads (i.e. self-weight) were neglected. The location of the supports and loads for the flexural specimens are indicated in Figure 78, Figure 79.

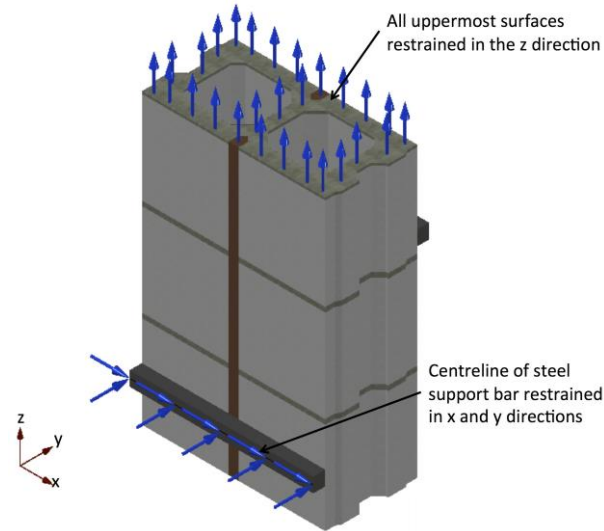


Figure 78: Flexural FEA model, support conditions

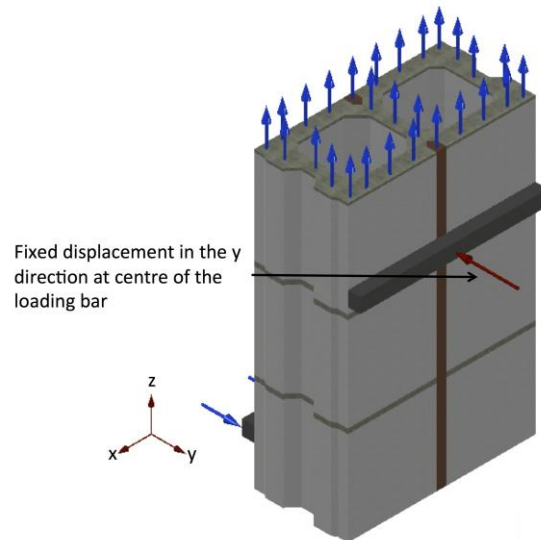


Figure 79: Flexural FEA model, loading conditions

5.4 Pull-out analysis

The analysis of finite element models was performed with two different reinforcement types; similarly to the experimental work, a test was performed with the reinforcing bar having the properties and cross-sectional area of the 10M rebar from Chapter 3, and another one with the

reinforcing bar having the properties of the #3 GFRP bar, also from Chapter 3. Both models were analysed with each of the three different reinforcement bond-slip models from Table 27. The load-slip and reinforcing bar strain behaviour of the FEA models were compared to the behaviour of the experimental specimens. Note that total slip data for the experimental specimens were generated using the same method as in 4.1.3 (i.e. by integrating strains in the reinforcing bars using the trapezoid rule).

5.4.1 Steel reinforcement

The load-slip data from the FEA analyses for all three bond models are overlaid onto the load-slip data from pull-out specimens P1, P2, and P3 in Figure 80. All three FEA models show the reinforcing bar reaching achieving its yield strength, however the behaviour in the strain-hardening region of the reinforcing bar does not seem to be accurately simulated. All three bond models also appear to accurately represent the slope of the experimental load-slip curves.

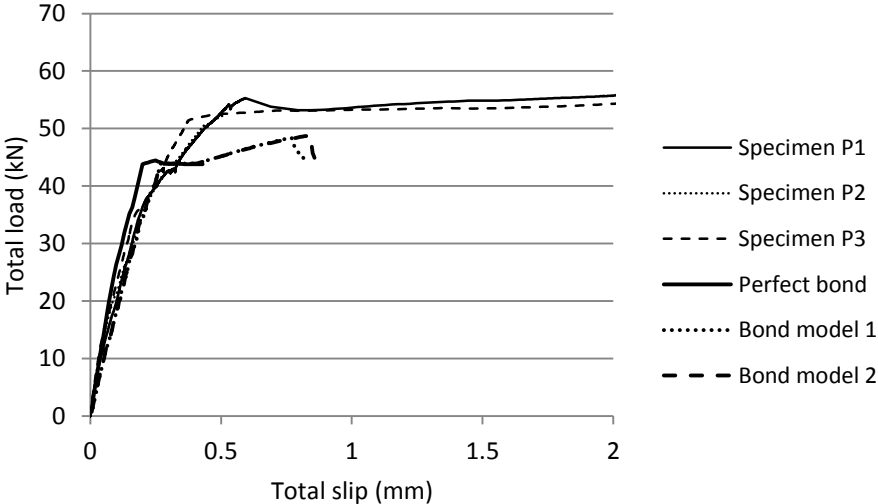


Figure 80: Steel-reinforced pull-out load vs. total slip (at surface), experimental and FEA data

Stress transfer through the reinforcing bar is shown in Figure 81, Figure 82, Figure 83, and Figure 84. From these figures, it may be concluded that strain behaviour up to the yield point of reinforcing steel is accurately estimated in by all three bond models to a depth of at least 145mm from the loaded end of the pull-out models. At 245mm from the loaded end, only “Bond model 2” accurately estimates bar stresses, and at 345mm, none of the bond models tested appear to function properly.

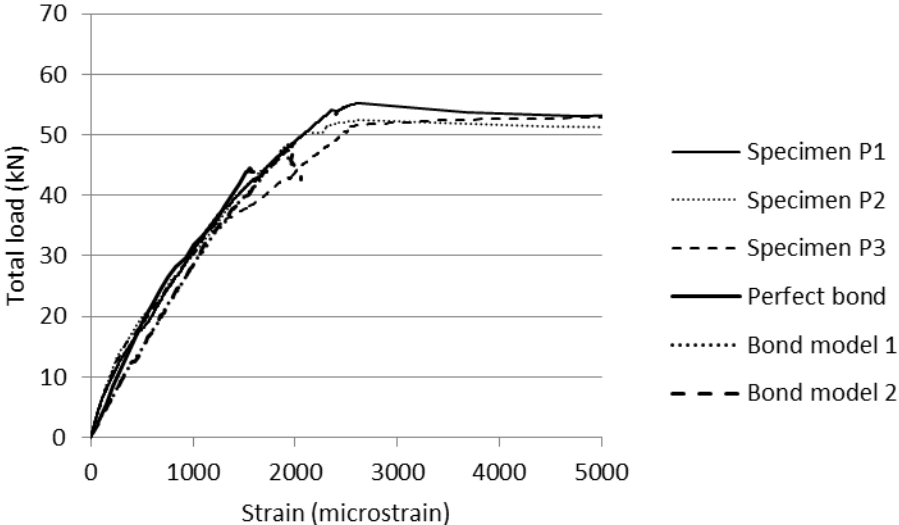


Figure 81: Pull-out load vs strain at 45mm from the loaded end, steel-reinforced specimens

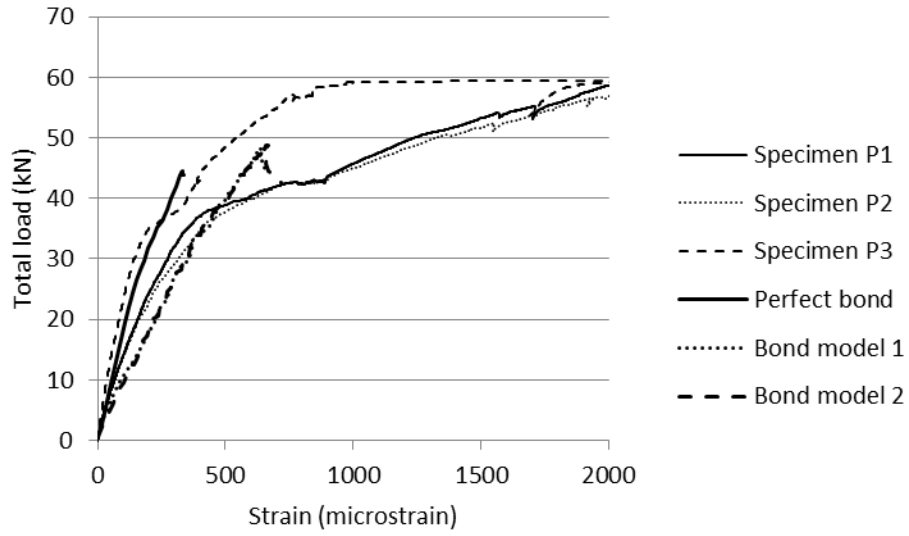


Figure 82: Pull-out load vs strain at 145mm from the loaded end, steel-reinforced specimens

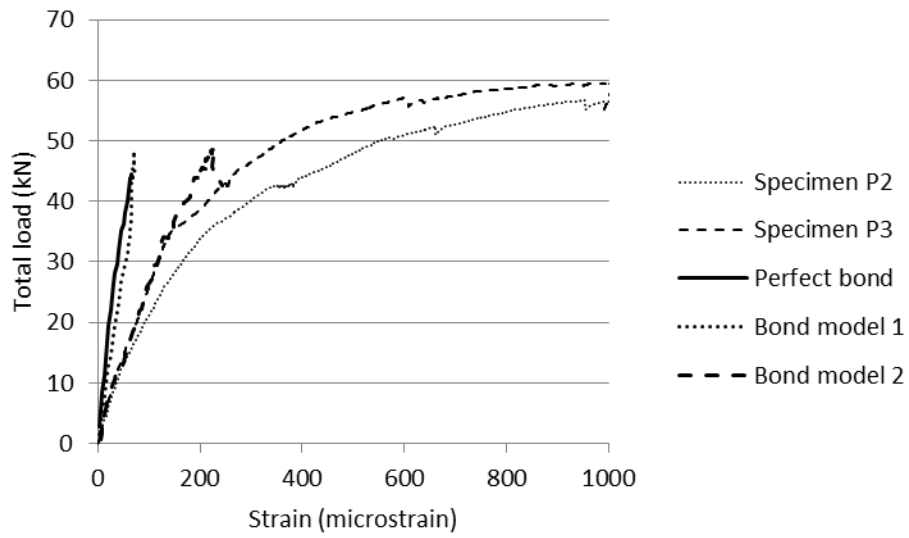


Figure 83: Pull-out load vs strain at 245mm from the loaded end, steel-reinforced specimens

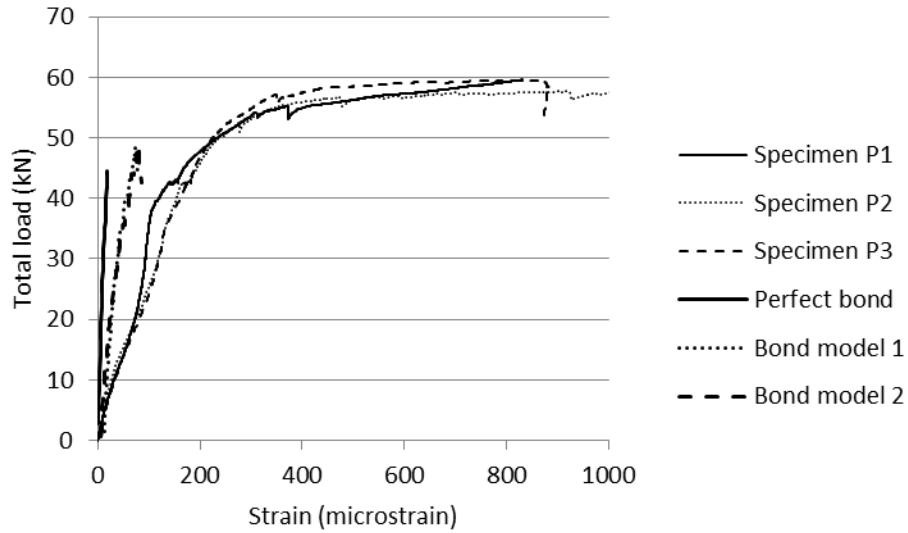


Figure 84: Pull-out load vs strain at 345mm from the loaded end, steel-reinforced specimens

5.4.2 GFRP reinforcement

Figure 85 shows the load vs. slip behaviour of the three GFRP-reinforced experimental pull-out specimens as well as the data generated by the ATENA FEA models for each of the three bond model. None of the models captured the load capacity observed in the experimental specimens because of non-convergence; however all three models accurately estimated the initial slope of the experimental load-slip curves.

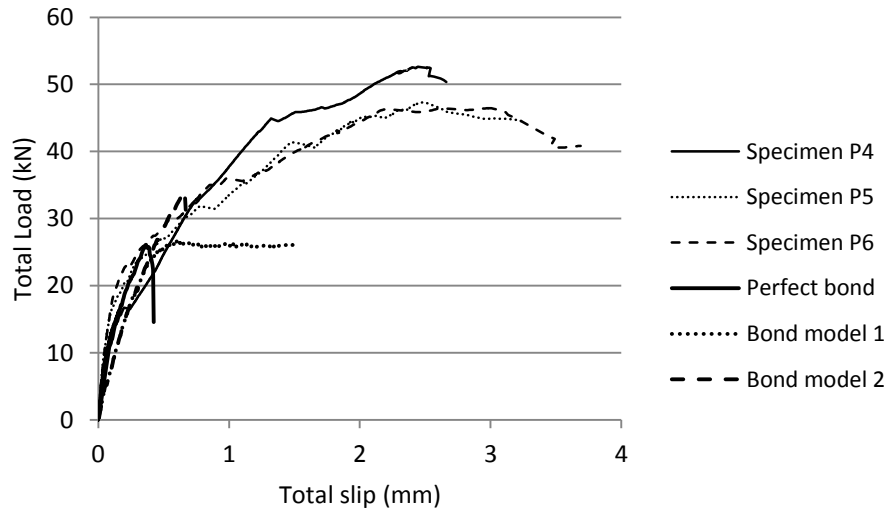


Figure 85: GFRP-reinforced Pull-out load vs. total slip (at surface), experimental and FEA data

Figure 86 shows bar stresses in all three FEA models closely match those recorded in the upper most strain gauge of the experimental specimens (45mm from the loaded end). In particular, the Perfect Bond model appears true to the experimental data at loads up to roughly 25kN and “Bond model 2” closely matches the experimental data between roughly 20kN and 35kN.

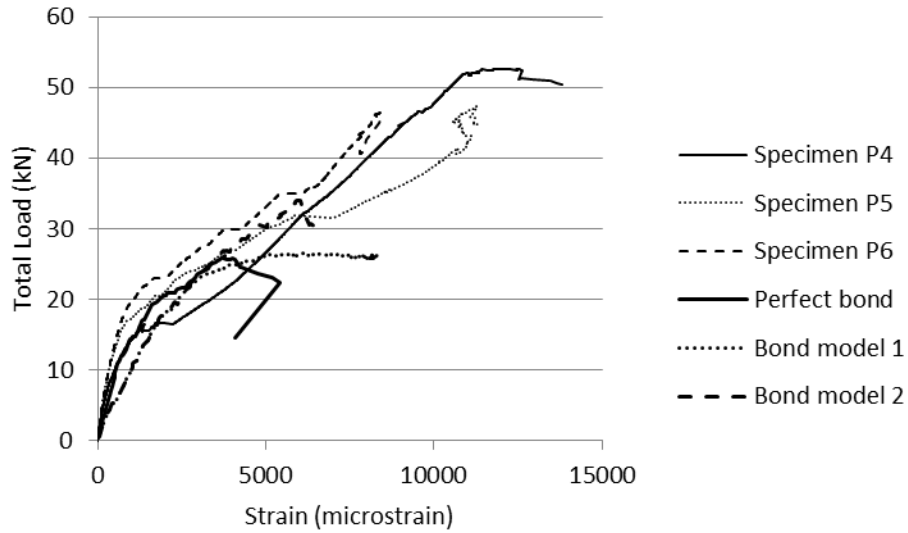


Figure 86: Pull-out load vs strain at 45mm from the loaded end, GFRP-reinforced specimens

However, Figure 87 reveals that bar stresses in the FEA model are not appropriately transferred further down the reinforcing bar. Further refinement in the bond model for the reinforcing bars is manifestly necessary for a more accurate prediction of GFRP reinforcing bar anchorage strength into SRCMU masonry systems. A more detailed study of this behaviour may follow in future research.

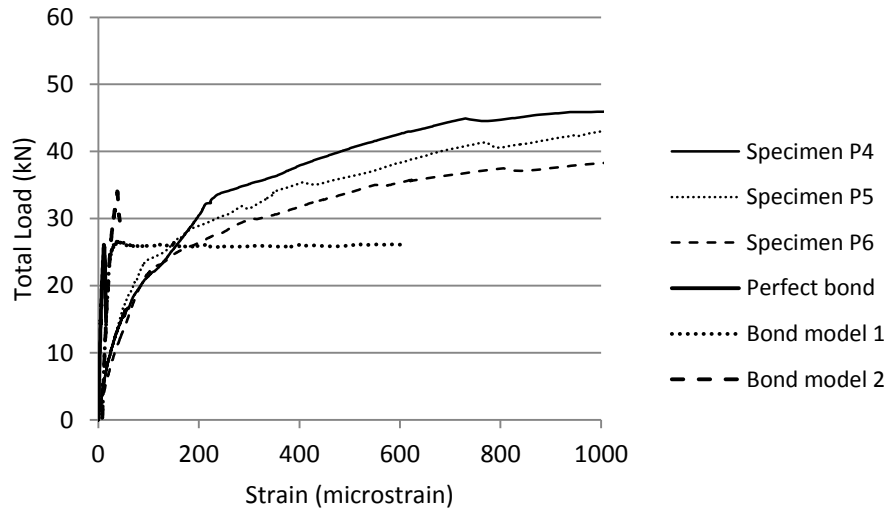


Figure 87: Pull-out load vs strain at 245mm from the loaded end, GFRP-reinforced specimens

5.5 Flexural analysis

Finite element analysis of the flexural models was performed twice; once with the reinforcing bar having the properties and cross-sectional area of the 10M rebar from Chapter 3, and once with the reinforcing bar having the properties of the #3 GFRP bar, also from Chapter 3. A perfect bond between all materials in contact with each other was assumed. For comparison with the behaviour of the experimental specimens, strain, deflection and crack width were recorded during each analysis at the same location as for the experimental specimens. Crack width for the model is determined by doubling the vertical displacement of two nodes located centrally within the upper block of the specimen, at the location of one of the lower pi-gauge mount in the experimental specimens.

5.5.1 Perfect bond – Steel reinforcement

The load-deflection curve of the FEA model is displayed next to the experimental data in Figure 88. Important differences to note are the significantly higher peak load and higher stiffness at loads up to roughly 10kN; both these differences may be largely attributed to the perfect bond assumed between the reinforcing bar and the epoxy grout, and between the mortar joints and the concrete blocks.

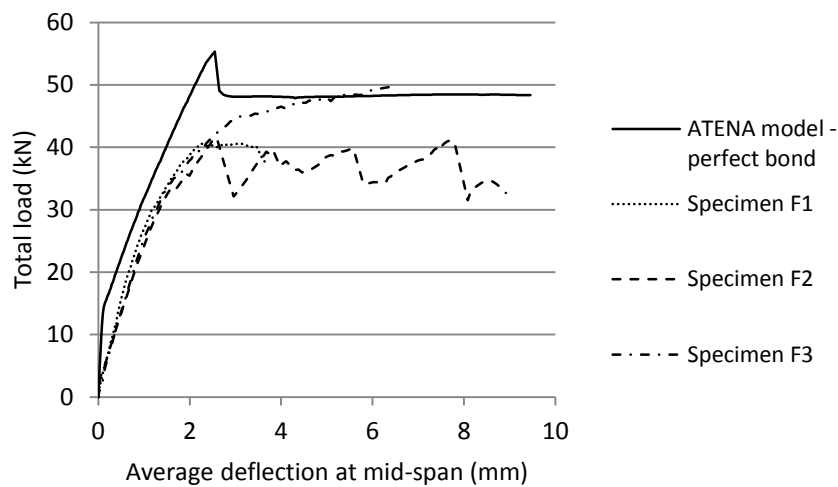


Figure 88: Load-deflection curve, comparison with ATENA FEA - steel-reinforced

Better agreement may be observed for the other sensors; for example crack width of the FEA model closely matches that of the experimental specimens until shear failure occurred in the block. This may be seen in Figure 89. Note that Specimen F3 exhibited a significant yield plateau in the reinforcing bar before failure occurred in shear. The FEA model, possibly overestimating the shear strength of the masonry blocks, displayed this ductile mode of failure following the peak load. Specimens F1 and F2 show decreasing crack width following the peak

load since shear displacements allowed the central crack to close. Specimen F3 as well as the FEA model show increasing crack width during the yielding of the steel reinforcing bar.

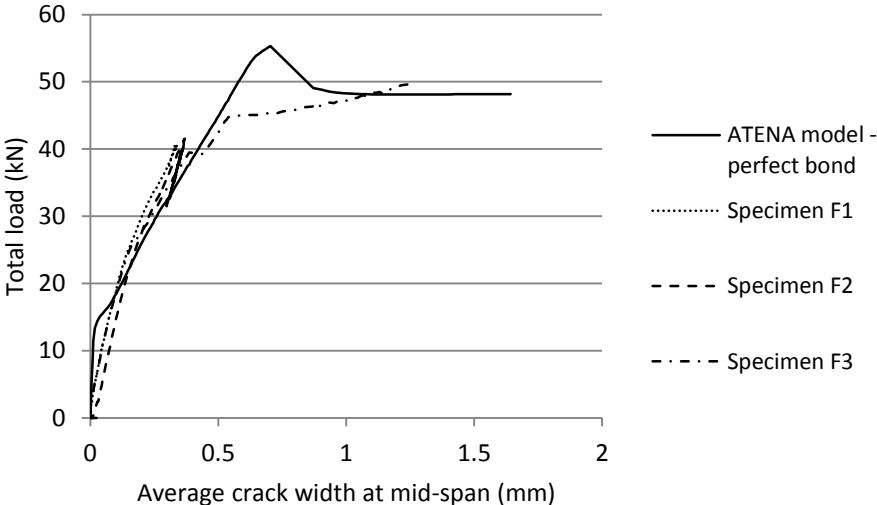


Figure 89: Crack-width expansion, comparison with ATENA FEA - steel-reinforced

Strain at mid-span of the tension reinforcing bar also closely follows the experimental data until either the yielding of the reinforcing steel, or shear failure of the blocks occurred, as shown in Figure 90.

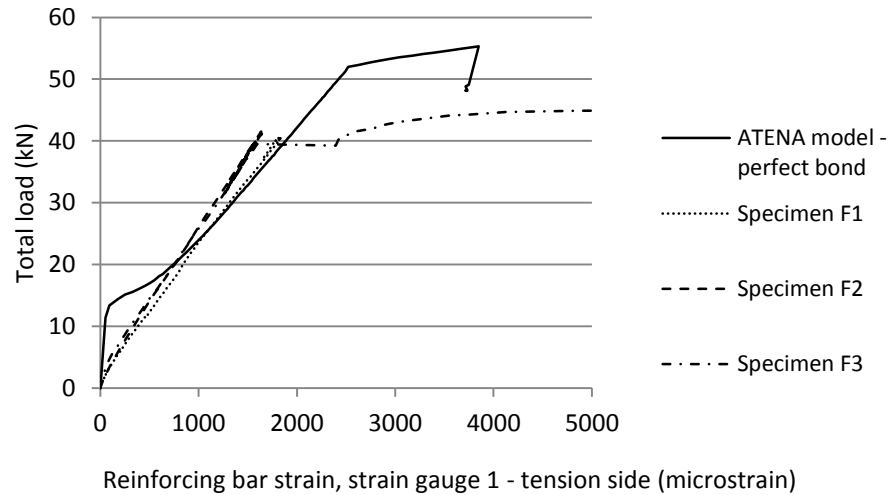


Figure 90: Reinforcing bar strain, comparison with ATENA FEA - steel-reinforced

Overestimation of the flexural strength of the flexural specimens by the FEA model is most likely due to the fact that the FEA model assumed greater synergy between the reinforcing steel and the epoxy grout. In the experimental specimens, small cracks and slipping between the steel and epoxy seem to have contributed to the reduced impact of the epoxy on the over-all strength of the steel-reinforced flexural specimens. Although some cracking in the epoxy was captured by the FEA model, the lack of allowed slip between steel and epoxy, and between epoxy and masonry appear to have contributed to over-all increase in apparent strength.

5.5.2 Perfect bond – GFRP reinforcement

The load-deflection curve of the GFRP-reinforced FEA flexural model is displayed next to the experimental data in Figure 91. Very strong agreement is observed between the FEA model and the experimental data over the majority of the displacement range. Major differences between the FEA model and the experimental data include the higher stiffness of the model at loads up to 15kN and the lack of a decrease in load due to shear failure of the masonry blocks. The higher

stiffness at low loads is a result of the perfect bond assumed between the masonry blocks and mortar joints, resulting in a higher stiffness prior to cracking. As mentioned earlier in Chapter 4, the experimental flexural specimens did not display pre-cracking behaviour.

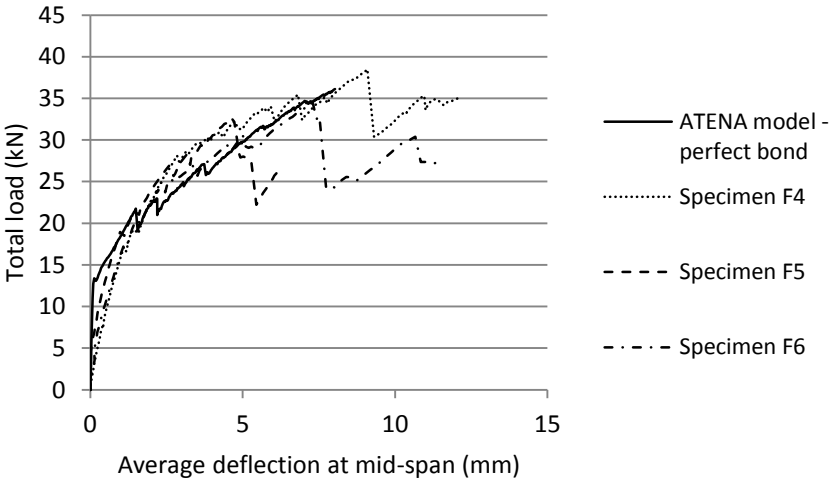


Figure 91: Load-deflection curve, comparison with ATENA FEA - GFRP-reinforced

The growth of crack width at mid-span, as seen in Figure 92, and the strain in the tension reinforcement at mid-span, as seen in Figure 93, show similarly good agreement between the FEA model and the experimental data following the initiation of the central crack in the FEA model at approximately 13kN of load.

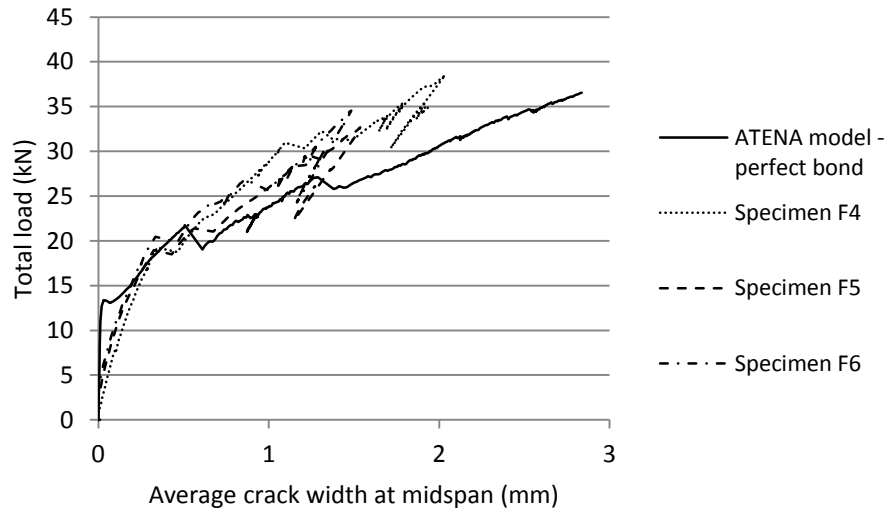


Figure 92: Crack-width expansion, comparison with ATENA FEA - GFRP-reinforced

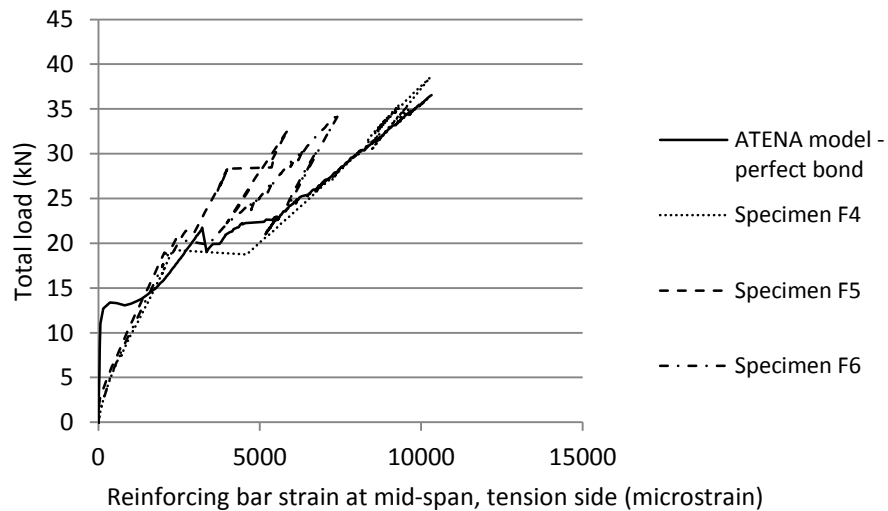


Figure 93: Reinforcing bar strain, comparison with ATENA FEA - GFRP-reinforced

The GFRP-reinforced FEA model appears to have better agreement with the experimental data than the Steel-reinforced FEA model. This is most likely due to the increased cracking of the epoxy effected in the GFRP-reinforced model by the higher strains in the GFRP at low load levels due to its lower stiffness. This resulted in the behaviour being more-so

dependent on the cracking behaviour of the epoxy (which appears to have been effectively modeled) than the load-slip behaviour (which was not modeled in this case).

6 Conclusion and Future Work

The SRCMU system is a promising technology for the masonry construction sector. This work demonstrates many of the benefits of the proposed system over existing conventional reinforced masonry technology. By including vertical channels into the face shells of CMUs, reinforcing bars can be placed near the extreme tension fibre of walls in out-of-plane flexure using the NSM reinforcing technique.

6.1 Benefits of the SRMCU system

The new proposed SRCMU reinforced concrete masonry system is shown to have many benefits over conventional masonry construction. Out-of-plane flexural analysis of various wall configurations possible to achieve using the SRCMU system were analysed using the CSA S304.1 Masonry Design Code. By optimizing the location of reinforcing steel bars, an increase in capacity of up to 30%, when compared to conventionally reinforced concrete masonry systems with the same cross-sectional area of steel reinforcement, was observed. The flexural stiffness of the SRCMU systems are nearly twice that of equivalent conventional masonry systems. This design performance is contingent mainly on the capacity to bond reinforcing bars into the reinforcement channels of SRCMU assemblies.

The NSM reinforcement technique, by which reinforcing bars are adhered into surface channels cut into structural members to be reinforced, has been extensively studied, and is now used in the structural retrofitting of existing structures. The technology has been proven to impart levels of shear and flexural capacity equivalent to that of conventionally embedded reinforcement for reinforced concrete structures. Application of this technique to new masonry construction is expected to perform similarly well.

In addition to structural benefits of additional strength and stiffness, the SRCMU system is in many ways more environmentally friendly than conventional masonry systems. The decrease in the volume of concrete necessary for the construction of SRCMU assemblies results in a large reduction in the over-all weight of a finished structure. The replacement of grout-filled cores with small epoxy-filled channels results in a net reduction in embodied greenhouse gas emissions, and hollow walls allow for a greater insulating capacity. Faster construction made possible with the NSM reinforcement technique results in a decrease in heating-related construction costs for winter construction.

Over-all, preliminary analysis of the SRCMU masonry system showed it is stronger and more environmentally friendly than the existing conventional reinforced concrete masonry system. The additional strength of this masonry system may result in an over-all reduction in cost of a finished structure, and the decreased environmental impact will only improve the desirability of this innovative masonry system.

6.2 Axial behaviour

Experimental laboratory work studied the effect of the SRCMU shape on its axial compressive properties when compared to the conventional CMU shape. Four-high masonry prisms were constructed then loaded axially until failure. The ultimate failure load as well as axial strain data was recorded.

The axial compressive properties of prisms produced from commercially-produced conventional CMUs and those of conventionally shaped and SRCMU-shaped CMUs produced in the laboratory were compared. No significant variation in compressive properties was observed between the three populations of prisms. This result showed that the laboratory casting procedure

used to produce the SRCMUs adequately simulates that of commercial production and that there is no disadvantage to the SRCMU inherent in the shape of the block.

6.3 Flexural behaviour

The out-of-plane flexural behaviour of the reinforced SRCMU system was tested with the aid of small pull-out and flexural test specimens, and numerical models. Pull-out specimens were constructed by reinforcing three-high masonry prisms on one side with a protruding reinforcing bar, and loaded by restraining the masonry prism and applying tension on the protruding reinforcing bar. The flexural test specimens consisted of six-high SRCMU masonry prisms reinforced on both sides with reinforcing bars using a dowelling epoxy, and were then loaded using a 4-point bending configuration. Both types of test were performed in triplicate with 10M steel rebar and #3 sand-coated GFRP bars.

The pull-out tests showed that it is possible to develop the full design strength of both types of reinforcement (steel and GFRP). Steel-reinforced specimens performed better than the GFRP-reinforced specimens due to steel's greater tensile stiffness resulting in better stress transfer to the masonry prism. Numerical FEA of the pull-out tests revealed that proper modeling of the bond-slip behaviour of the reinforcing bar in tension is critical to the model's accuracy. The behaviour of the flexural specimens under 4-point bending conformed very well to that predicted by the S304.1 design code. Good agreement was observed between the load-deflection experimental data, and the code-predicted load deflection behaviour up to the failure load of the specimens. The ultimate flexural strength was not observed in this study, as the flexural specimens all failed in shear; however ultimate loads approaching the maximum loads predicted by design codes were achieved. FEA modeling of the flexural specimens tested revealed that the shear characteristics of the concrete masonry units, as well as the bond-slip relationship between

the reinforcing bars and the epoxy grout have a large effect on the over-all behaviour of the reinforced SRCMU systems in out-of-plane bending.

Physical and numerical testing of SRCMU assemblies confirmed that their behaviour closely match that predicted by existing masonry design codes; good bonding between the reinforcing bars and the masonry assembly, greater flexural stiffness, and high flexural strength were all observed. Care must be taken when constructing FEA models to accurately represent the shear and load-slip behaviours of the configuration being studied.

6.4 Proposed future work

The work discussed in this document demonstrates the potential of the SRCMU system for structural applications. More tests are nonetheless necessary to fully characterize its behaviour and generate sufficient evidence to develop design procedures. The following research activities are proposed to further develop this technology.

6.4.1 Test confirmation

The experimental procedures discussed in this document should be repeated using commercially produced SRCMUs to both study the behaviour of SRCMU blocks that have been cast using commercial production techniques, and increase the experimental data on SRCMU blocks and assemblies. Extensive documentation of the performance of SRCMU assemblies will be necessary prior to its implementation in the construction industry.

6.4.2 Tall flexural walls

An area of construction in which the SRCMU system would be particularly useful is the construction of tall and slender walls of industrial warehouse structures. Conventional masonry is not suited for this application because of its susceptibility to moment magnification. The

enhanced stiffness of the SRCMU system promises to mitigate the effects of moment magnification on masonry walls. Axial and flexural loading of 12m slender test walls will be necessary to confirm these benefits.

6.4.3 SRCMU walls in Shear

Masonry walls are currently widely used in the shear strengthening of steel and reinforced concrete frame structures. The behaviour of reinforced SRCMU walls in in-plane shear should be explored to determine if any benefits exist over conventional CMU construction.

6.4.4 Fire resistance

Conventional masonry assemblies are commonly used as fire separations. The placement of reinforcing bars near the surface of SRCMU assemblies may make them more susceptible to fire damage. Study of the fire resistance of SRCMU assemblies is necessary to determine the extent of its fire resistance, and develop appropriate protective systems.

6.4.5 Earthquake resistance

The high flexural strength of SRCMU systems make them attractive for the construction of earthquake-resistant structures. The behaviour of these systems under simulated earthquake conditions, such as reversed cyclic loading, will need to be studied.

6.4.6 Monitoring of a complete structure

Finally, a complete building using the SRCMU as its main structural system will need to be constructed. The performance of this structure over time may be monitored using strain gauges and load cells, as well as temperature and humidity sensors. As the SRCMU system promises benefits to both the strength and sustainability of a finished structure, energy inputs to the building over its lifetime should also be tracked to help quantify its environmental benefits.

References

Asplund, S. O. 1949. "Strengthening bridge slabs with grouted reinforcement." *Journal of the American Concrete Institute* 20(6):397–406.

ASTM International. 2013. "Standard Test Method for Total Evaporable Moisture Content of Aggregate by Drying." ASTM C566-13

ASTM International. 2006. "Standard Test Method for Tensile Properties of Fiber Reinforced Polymer Matrix Composite Bars." ASTM D7204-06

ASTM International. 2014. "Standard Test Methods and Definitions for Mechanical Testing of Steel Products1." ASTM A370-14

ASTM International. 2014. "Standard Test Method for Compressive Strength of Cylindrical Concrete Specimens." ASTM C39-14

Barros, J. A. O., D. R. S. M. Ferreira, A. S. Fortes, and S. J. E. Dias. 2006. "Assessing the Effectiveness of Embedding CFRP Laminates in the Near Surface for Structural Strengthening." *Construction and Building Materials* 20 (7): 478-491. doi:10.1016/j.conbuildmat.2005.01.030

Bernstein, L., J. Roy, K. C. Delhotal, J. Harnisch, R. Matsushashi, L. Price, K. Tanaka, E. Worrell, F. Yamba, Z. Fengqi. 2007. "Industry." In *Climate Change 2007: Mitigation. Contribution of Working Group III to the Fourth Assessment Report of the Intergovernmental*

Panel on Climate Change, edited by B. Metz, O.R. Davidson, P.R. Bosch, R. Dave, L.A. Meyer, Cambridge University Press, Cambridge, United Kingdom and New York, NY, USA.

Cabeza, L. F., C. Barreneche, L. Miró, J. M. Morera, E. Bartolí, and A. Inés Fernández. 2013. "Low Carbon and Low Embodied Energy Materials in Buildings: A Review." *Renewable and Sustainable Energy Reviews* 23: 536-542. doi:10.1016/j.rser.2013.03.017

Carney, P. and J. J. Myers. 2003. "Shear and Flexural Strengthening of Masonry Infill Walls with FRP for Extreme Out-of-Plane Loading." Paper presented at Architectural Engineering 2003: Building Integration Solutions, Austin, Texas, USA, September 17-20.
doi:10.1061/40699(2003)45

Cervenka Consulting. 2015. "ATENA" (release version 5.1.1t) [computer software], Prague, Czech Republic. Available from <http://www.cervenka.cz/download/>

ColoradoENERGY.org. 2014. "R-Value Table." Last modified August 18.
<http://www.coloradoenergy.org/procorner/stuff/r-values.htm>

Concrete Masonry Association of Australia. 2000. "MA46 Manufacture of Concrete Masonry," Concrete Masonry Association of Australia, Artarmon, Australia.
http://brikmakers.com/docs/cmaaguide/cmaa_ma46.pdf

Cook, D. J., R. P. Pama, and B. K. Paul. 1977. "Rice Husk Ash-Lime-Cement Mixes for use in Masonry Units." *Building and Environment* 12 (4): 281-288. doi:10.1016/0360-1323(77)90031-2

Crawford, R. H. 2003. "Validation of the use of Input-Output Data for Embodied Energy Analysis of the Australian Construction Industry." *Journal of Construction Research* 6 (1): 71-90. doi:10.1142/S1609945105000250

CSA Group. 2014. "Concrete materials and methods of concrete construction/Test methods and standard practices for concrete." CSA A23.2-14.

CSA Group. 2004. "CSA Standards on Concrete Masonry Units." CSA A165-04.

CSA Group. 2004. "Design of Masonry Structures." CSA S304.1-04.

CSA Group. 2014. "Mortar and grout for unit masonry." CSA A179-14.

Damineli, B. L., F. M. Kemeid, P. S. Aguiar, and V. M. John. 2010. "Measuring the Eco-Efficiency of Cement use." *Cement and Concrete Composites* 32 (8): 555-562.
doi:10.1016/j.cemconcomp.2010.07.009

De Lorenzis, L., A. Rizzo, and A. La Tegola. 2002. "A Modified Pull-Out Test for Bond of Near-Surface Mounted FRP Rods in Concrete." *Composites Part B: Engineering* 33 (8): 589-603. doi:10.1016/S1359-8368(02)00052-5

De Lorenzis, L. and J. G. Teng. 2007. "Near-Surface Mounted FRP Reinforcement: An Emerging Technique for Strengthening Structures." *Composites Part B: Engineering* 38 (2): 119-143. doi:10.1016/j.compositesb.2006.08.003

De Sena Cruz, J. M. and J. A. O. De Barros. 2004. "Bond between Near-Surface Mounted Carbon-Fiber-Reinforced Polymer Laminate Strips and Concrete." *Journal of Composites for Construction* 8 (6): 519-527. doi:10.1061/(ASCE)1090-0268(2004)8:6(519)

Derakhshan, H., D. Dizhur, M. C. Griffith, and J. M. Ingham. 2014. "In Situ Out-of-Plane Testing of as-Built and Retrofitted Unreinforced Masonry Walls." *Journal of Structural Engineering (United States)* 140 (6). doi:10.1061/(ASCE)ST.1943-541X.0000960

Dizhur, D., M. Griffith, and J. Ingham. 2013. "In-Plane Shear Improvement of Unreinforced Masonry Wall Panels using NSM CFRP Strips." *Journal of Composites for Construction* 17 (6). doi:10.1061/(ASCE)CC.1943-5614.0000400

Dizhur, D., M. Griffith, and J. Ingham. 2014. "Out-of-Plane Strengthening of Unreinforced Masonry Walls using Near Surface Mounted Fibre Reinforced Polymer Strips." *Engineering Structures* 59: 330-343. doi:10.1016/j.engstruct.2013.10.026

Dizhur, D., M. C. Griffith, and J. M. Ingham. 2014. "Pullout Strength of NSM CFRP Strips Bonded to Vintage Clay Brick Masonry." *Engineering Structures* 69: 25-36.

doi:10.1016/j.engstruct.2014.02.006

Drysdale, R. G. and A. A. Hamid. 2005. *Masonry Structures Behaviour and Design: Canadian Edition*. Mississauga: Canada Masonry Design Centre.

Expocrete an Oldcastle Company. 2012. "Standard Shapes MB," Last modified Feb 2nd, 2012.

<http://www.expocrete.com/pdf/masonry/standard/masonry-standard-mb.pdf>

Fay, R., G. Treloar, and U. Iyer-Raniga. 2000. "Life-Cycle Energy Analysis of Buildings: A Case Study." *Building Research and Information* 28 (1): 31-41. doi:10.1080/096132100369073

Goggins, J., T. Keane, and A. Kelly. 2010. "The Assessment of Embodied Energy in Typical Reinforced Concrete Building Structures in Ireland." *Energy and Buildings* 42 (5): 735-744.

doi:10.1016/j.enbuild.2009.11.013

Habert, G. and N. Roussel. 2009. "Study of Two Concrete Mix-Design Strategies to Reach Carbon Mitigation Objectives." *Cement and Concrete Composites* 31 (6): 397-402.

doi:10.1016/j.cemconcomp.2009.04.001

Hammond, G. P. and Jones, C. I. 2008 "Embodied energy and carbon in construction materials." *Proceedings of the Institution of Civil Engineers - Energy*, 161 (2). pp. 87-98.

doi:10.1680/ener.2008.161.2.87

Hammond, G. and C. Jones. 2008. *Inventory of Carbon and Energy (ICE): Version 1.6a*. Bath, UK: University of Bath.

http://www.ecocem.ie/downloads/Inventory_of_Carbon_and_Energy.pdf

Hazaree, C., H. Ceylan, and K. Wang. 2011. "Influences of Mixture Composition on Properties and Freeze-Thaw Resistance of RCC." *Construction and Building Materials* 25 (1): 313-319.

doi:10.1016/j.conbuildmat.2010.06.023

Hüsken, G. and H. J. H. Brouwers. 2012. "On the Early-Age Behavior of Zero-Slump Concrete." *Cement and Concrete Research* 42 (3): 501-510. doi:10.1016/j.cemconres.2011.11.007

Jiao, Y., C. R. Lloyd, and S. J. Wakes. 2012. "The Relationship between Total Embodied Energy and Cost of Commercial Buildings." *Energy and Buildings* 52: 20-27.

doi:10.1016/j.enbuild.2012.05.028

Kashyap, J., M. C. Griffith, M. S. Mohamed Ali, and D. J. Oehlers. 2011. "Prediction of Load-Slip Behavior of FRP Retrofitted Masonry." *Journal of Composites for Construction* 15 (6): 943-951. doi:10.1061/(ASCE)CC.1943-5614.0000224

Lunn, D. S. and S. H. Rizkalla. 2014. "Design of FRP-Strengthened Infill-Masonry Walls Subjected to Out-of-Plane Loading." *Journal of Composites for Construction* 18 (3). doi:10.1061/(ASCE)CC.1943-5614.0000412

Patel, H. H., C. H. Bland, and A. B. Poole. 1995. "The Microstructure of Concrete Cured at Elevated Temperatures." *Cement and Concrete Research* 25 (3): 485-490. doi:10.1016/0008-8846(95)00036-C

Petersen, R. B., M. J. Masia, and R. Seracino. 2010. "In-Plane Shear Behavior of Masonry Panels Strengthened with NSM CFRP Strips. I: Experimental Investigation." *Journal of Composites for Construction* 14 (6): 754-763. doi:10.1061/(ASCE)CC.1943-5614.0000134

Petersen, R. B., M. J. Masia, and R. Seracino. 2010. "In-Plane Shear Behavior of Masonry Panels Strengthened with NSM CFRP Strips. II: Finite-Element Model." *Journal of Composites for Construction* 14 (6): 764-774. doi:10.1061/(ASCE)CC.1943-5614.0000137

Rahal, K. N. and H. A. Rumaih. 2011. "Tests on Reinforced Concrete Beams Strengthened in Shear using Near Surface Mounted CFRP and Steel Bars." *Engineering Structures* 33 (1): 53-62. doi:10.1016/j.engstruct.2010.09.017

Rashid, R. A. and G. C. Frantz. 1992. "MSW Incinerator Ash as Aggregate in Concrete and Masonry." *Journal of Materials in Civil Engineering* 4 (4): 353-368. doi:10.1061/(ASCE)0899-1561(1992)4:4(353)

SIKA Canada Inc. 2014. "Sika AnchorFix®-3001." In Commercial Construction 2014 Product Catalogue, 3-502. Pointe-Claire: Sika Canada Inc.

Täljsten, B., A. Carolin, and H. Nordin. 2003. "Concrete Structures Strengthened with Near Surface Mounted Reinforcement of CFRP." *Advances in Structural Engineering* 6 (3): 201-213. doi:10.1260/136943303322419223

Tan, K. and O. E. Gjørsv. 1996. "Performance of Concrete Under Different Curing Conditions." *Cement and Concrete Research* 26 (3): 355-361. doi:10.1016/S0008-8846(96)85023-X

Tumialan, J. G., F. Micelli, and A. Nanni. 2001. "Strengthening of Masonry Structures with FRP Composites." Paper presented at Structures 2001: A Structural Engineering Odyssey, Washington, D.C., USA, May 21-23. doi:10.1061/40558(2001)130

Tumialan, J. G., M. Vatovec, and P. L. Kelley. 2007. "Case Study: Strengthening of Parking Garage Decks with Near-Surface-Mounted CFRP Bars." *Journal of Composites for Construction* 11 (5): 523-530. doi:10.1061/(ASCE)1090-0268(2007)11:5(523)

Turco, V., S. Secondin, A. Morbin, M. R. Valluzzi, and C. Modena. 2006. "Flexural and Shear Strengthening of Un-Reinforced Masonry with FRP Bars." *Composites Science and Technology* 66 (2): 289-296. doi:10.1016/j.compscitech.2005.04.042

Türkel, S. and V. Alabas. 2005. "The Effect of Excessive Steam Curing on Portland Composite Cement Concrete." *Cement and Concrete Research* 35 (2): 405-411.

doi:10.1016/j.cemconres.2004.07.038